Mixing and the Geometry of Isosurfaces in Turbulent Jets

HARIS J. CATRAKIS

Graduate Aeronautical Laboratories
California Institute of Technology
Pasadena, CA 91125

23 May 1996

Thesis submitted in partial fulfillment of the degree requirements of
Doctor of Philosophy in Aeronautics

Abstract

Experiments have been conducted to investigate mixing and the geometry of scalar isosurfaces in turbulent jets. Specifically, images of the jet-fluid concentration in the far-field of round, liquid-phase, turbulent jets have been recorded at high resolution and signal-to-noise ratio using laser-induced-fluorescence digital-imaging techniques, in the Reynolds number range $4.5 \times 10^3 \leq Re \leq 18 \times 10^3$. Analysis of these data indicates that this Reynolds-number range spans a mixing transition in the far field of turbulent jets. This is manifested in the probability-density function of the scalar field, as well as in other scalar-field and scalar-isosurface measures. Classical as well as fractal measures of the isosurfaces have been computed, from small to large spatial scales, and are found to be functions of both scalar threshold and Reynolds number. The coverage of level sets of jet-fluid concentration in the two-dimensional images is found to possess a scale-dependent-fractal dimension that increases continuously with increasing scale, from near unity, at the smallest scales, to 2, at the largest scales. The geometry of the scalar isosurfaces is, therefore, more complex than power-law fractal, exhibiting an increasing complexity with increasing scale. This behavior necessitates a scale-dependent generalization of power-law-fractal geometry. A connection between scale-dependent-fractal geometry and the distribution of scales is established and used to compute the distribution of spatial scales in the flow. A lognormal model of scales is proposed. The data also indicate a lognormal distribution of size of the isoscalar islands and lakes, and a power-law distribution of shape complexity, with values of the latter that increase with increasing size.

her wizened hand
reaches out
time collides
at her touch
in the clutch
of her fingers
lies the quick
of my beginnings
in the grasp
of her palm
a rhetoric of joy
and suffering
meets mine
as tomb on
tomb disinters

MARIA CATRAKIS, *Crete*

Μηδεὶς αγεωμέτρητος εισήτω.

PLATO, *ca.* 400 BC

A man needs a little insanity.

NIKOS KAZANTZAKIS, *Zorba the Greek*

I wish to express my gratitude to my mentor and collaborator, Paul Dimotakis, whose scientific spirit as well as zest for life have been a wonderful guide throughout this journey. To my parents, who have given me a life full of vitality and merriment, I dedicate this thesis.

Contents

Preface

Turbulent mixing refers to the advection and diffusion of any scalar quantity at high Reynolds number. Turbulent flow enhances (molecular diffusion) mixing and results, in turn, in more effective (local) scalar-field homegenization, relative to laminar-flow mixing. The structure and dynamics of turbulent mixing reflect the complexity of turbulent flow. Apart from its scientific significance, turbulent mixing is biologically, environmentally, and technologically important in various contexts. For example, several aspects of marine biology depend on fluid transport at high Reynolds number as many aquatic organisms rely on turbulent mixing for their survival (consumption, waste, dispersion, and evolution) in the oceans (*e.g.*, Denny 1988). Other examples include dispersion of pollutants in the atmosphere and turbulent combustion.

Isosurfaces of the scalar field, *e.g.*, surfaces of constant species composition or temperature, are known to be highly convoluted in turbulent-mixing flows. For example, isosurfaces of passive scalars (*i.e.*, scalars that do not affect the advecting velocity field, such as dye markers), are known to exhibit a complex geometry in turbulent-jet flows (*e.g.*, Dimotakis, Miake-Lye, & Papantoniou 1983), as well as in other high-Reynolds number turbulent flows (*e.g.*, Sreenivasan & Meneveau 1986). The complex geometry of the isosurfaces arises, in part, because of the multiscale (and unsteady) nature of the structure and dynamics of turbulence.

Knowledge of the geometry of the scalar isosurfaces is necessary for an understanding of the turbulent mixing process. The isosurface geometry significantly affects (molecular diffusion) mixing, wave propagation, scattering, chemical reactions, and any physical process that depends on the area of the isosurfaces. In the case of nonpremixed hydrocarbon combustion, for example, chemical reactions are largely confined to the instantaneous (isoscalar) stoichiometric surface (*e.g.*, Bilger 1980), while in the case of premixed combustion, burning takes place on the (isotemperature) interface between burnt and unburnt fuel (*e.g.*, Mantzaras 1992), with

flame-front propagation characteristics that are intimately intertwined with the geometric complexity of the burning surface (*e.g.*, Ashurst 1995). Various measures of the isosurface geometry, such as surface-to-volume ratio or volume-fill fraction, and their relation to the distribution of spatial scales, are, as a consequence, important to our understanding and modeling of mixing, chemical reactions, and combustion in turbulent flows.

The need for a quantitative description of complex geometries also arises in other natural phenomena that involve fluid transport, *e.g.*, nephron cells possess a complex boundary that provides the high surface-to-volume ratio necessary for the high transport (mass flux) of water in response to a small osmotic gradient (*e.g.*, Welling *et al.* 1996). Other examples of natural complexity include the alveolar structure of lungs, the branching structure of blood vessels in the heart, complex organisms (*e.g.*, a virus), the trajectory of particles exhibiting Brownian motion, earthquake fault systems, *etc.*

In this thesis, mixing and the geometry of scalar isosurfaces in (liquid-phase) turbulent jets are investigated. In particular, the behavior and properties of scalar level sets in turbulent jets, identified from two-dimensional image slices of the scalar field, are analyzed using both classical and fractal measures. Chapter 1 describes the experiments and imaging techniques, and presents scalar-field image data. Chapter 2 analyzes classical scalar and isoscalar measures, computed from the scalar-field images. Reynolds-number as well as scalar-threshold dependence is found for both classical and fractal measures. The present findings necessitate an extension of the (power-law) fractal (denoted 'PLF', below) framework to characterize the more complex geometries observed in these experiments, as well as in other natural phenomena, for which PLF descriptions cannot capture the observed complexity.

The framework of scale-dependent-fractal (denoted as 'SDF', below) geometry is described in chapter 3. In this framework, geometric behavior is characterized by fractal dimensions that vary with scale, as opposed to scale-independent, PLF behavior. Chapter 4 establishes a connection between SDF dimensions and distributions of a measure of (multidimensional) scale. Chapter 5 presents experimental evidence of SDF behavior in turbulent-jet mixing, as well as its relation to the distribution of spatial scales in the flow. Chapter 6 reports a further analysis of the

isosurfaces that employs additional measures of geometric structure and complexity, based on the area-perimeter properties of the individual isoscalar islands and lakes, identified from the scalar level sets.

The experiments, as well as investigations of various measures of the scalar field and of the isosurface geometry (in particular, chapters 1–3, and 5), are also reported in Catrakis & Dimotakis (1996a). The framework connecting SDF dimensions to distributions of scales for complex geometries (chapter 4) can also be found in Catrakis & Dimotakis (1996b). Finally, area-perimeter measures of geometric complexity, with application to isoscalar islands and lakes in turbulent-jet mixing (*cf.*, chapter 6), are also reported in Catrakis & Dimotakis (1996c).

The findings of this thesis have general implications for other turbulent flows as well as for other phenomena that exhibit natural complexity. Analysis of the present measurements on isosurfaces in turbulent jets has led to the development of SDF geometry — a framework which can be used to quantify the geometric complexity, analyze the distribution of scales, and model the geometric behavior, in a variety of complex phenomena. For example, this framework can be applied to any phenomena for which SDF dimensions have been reported such as, the trajectory of particles in Brownian motion (Takayasu 1982), Japanese coastlines (Suzuki 1984), topographic surfaces (Mark & Aronson 1984), fractured rocks (Chilés 1988), the galaxy distribution in the universe (*e.g.*, Castagnoli & Provenzale 1991), solar granulation (Brandt *et al.* 1991), or the alveolar structure of lung tissues of prematurely-born rabbits (Rigaut 1991). Turbulent flows, in particular, exhibit structure over a wide range of scales and provide, therefore, a testbed for proposed frameworks that quantify the resulting geometric complexity. On the basis of the present findings of SDF behavior in turbulent mixing, as well as the implications and applications of the framework of SDF geometry in other phenomena, it is proposed that SDF geometry may be expected to be prevalent, and can be used to compute the scale distribution, in complex natural phenomena, in general, and in turbulence, in particular.

The guidance, advice, and constant inspiration of my mentor and collaborator, P. E. Dimotakis, throughout this effort, provided an invaluable educational experience as well as a unique research environment. The assistance and informal

collaboration with P. L. Miller, at the early stages of these investigations, the discussions with C. L. Bond, M. C. Cross, M. Gharib, A. Leonard, D. I. Pullin, and P. G. Saffman, as well as the electronics expertise of D. B. Lang and his assistance to the digital imaging technology employed in these experiments, are also gratefully acknowledged.

This research was financially supported by AFOSR Grant 90–0304 and GRI Contract 5087–260–1467, initially, and subsequently by AFOSR Grants F49620–92–J–0290 and F49620–94–1–0353.

CHAPTER 1

Experiments and scalar-field imaging techniques

In this chapter, experiments in turbulent jets are described. These experiments have been conducted in order to study the structure of turbulent mixing in the far-field of turbulent jets. Digital, solid-state (charge-coupled device, or CCD) cameras, coupled with laser-induced-fluorescence techniques, permit quantitative, multidimensional (field) measurements of the jet-fluid-concentration (scalar) field. In these experiments, two-dimensional, spatial measurements of the scalar field, or 2-D "slices", have been recorded in the form of digital images, at high resolution and high signal-to-noise ratio. The imaging was conducted in the far field, in a plane normal to the jet axis, and at the highest Reynolds numbers possible, as dictated by the size of the facility, the resolution of the camera, and the laser-sheet thickness. An assessment of the space-time resolution of these measurements is provided. The normalization and calibration procedure in the image processing is described. Examples of scalar-field images are presented and scalar power spectra are analyzed. Reynolds-number effects on the (radial) scalar power spectra are found.

1.1 Turbulent-jet facility

Experiments in liquid-phase, turbulent-jet flows were conducted in which images of slices through the three-dimensional scalar field of round, momentum-driven, turbulent jets were obtained. A schematic of the flow facility is shown in figure 1. It consists of the jet plenum, nozzle, and delivery system (not shown), and a large ($\simeq 1.1\,\mathrm{m}^3$), square-cross-section discharge tank with glass windows on four sides. For the present experiments, a 10-inch diameter glass window centered on the bottom face provided additional optical access, with a 45° mirror facilitating imaging from underneath the tank. Transverse sections of the scalar far-field of the jet, at a downstream station $z/d_0 = 275$, where $d_0 = 2.54\,\mathrm{mm}$ is the (internal) jet-nozzle diameter, were measured using planar, laser-induced-fluorescence, digital-imaging techniques (described in next section). More information on the facility can be found in Dahm (1985), Miller (1991), and references therein.

1.2 Laser-induced fluorescence imaging

Laser-induced fluorescence techniques, coupled with digital imaging, can be employed to provide quantitative, field information of the scalar-species concentration in turbulent-mixing flows (*e.g.*, Dimotakis *et al.* 1983, Koochesfahani & Dimotakis 1986). In the present experiments, two-dimensional, spatial measurements of the jet scalar far field were obtained by imaging the fluorescence field emitted by a laser dye (disodium fluorescein), premixed with the jet plenum fluid, upon excitation by an Argon-ion laser beam swept in the imaging plane.

The laser-induced fluorescence field was recorded on a cryogenically-cooled, (1024 × 1024)-pixel, CCD camera (Photometrics Series 200 system), with a Nikon 50 mm f/1.2 lens. Figure 2 shows a schematic of the geometry of the scalar far field of the jet and the imaging station. The laser-illumination sheet was at constant z/d_0, *i.e.*, in the similarity plane of the jet perpendicular to the jet axis, and spanned the entire extent of the jet-fluid concentration field at that downstream location.

The jet plenum was seeded with an aqueous solution of disodium fluorescein at a concentration of $c_0 \simeq 2.0 \times 10^{-6}\,\mathrm{M}$. The fluorescence response time of this laser dye is $\approx 4\,\mathrm{nsec}$ (see Dahm 1985), which is much shorter than the smallest

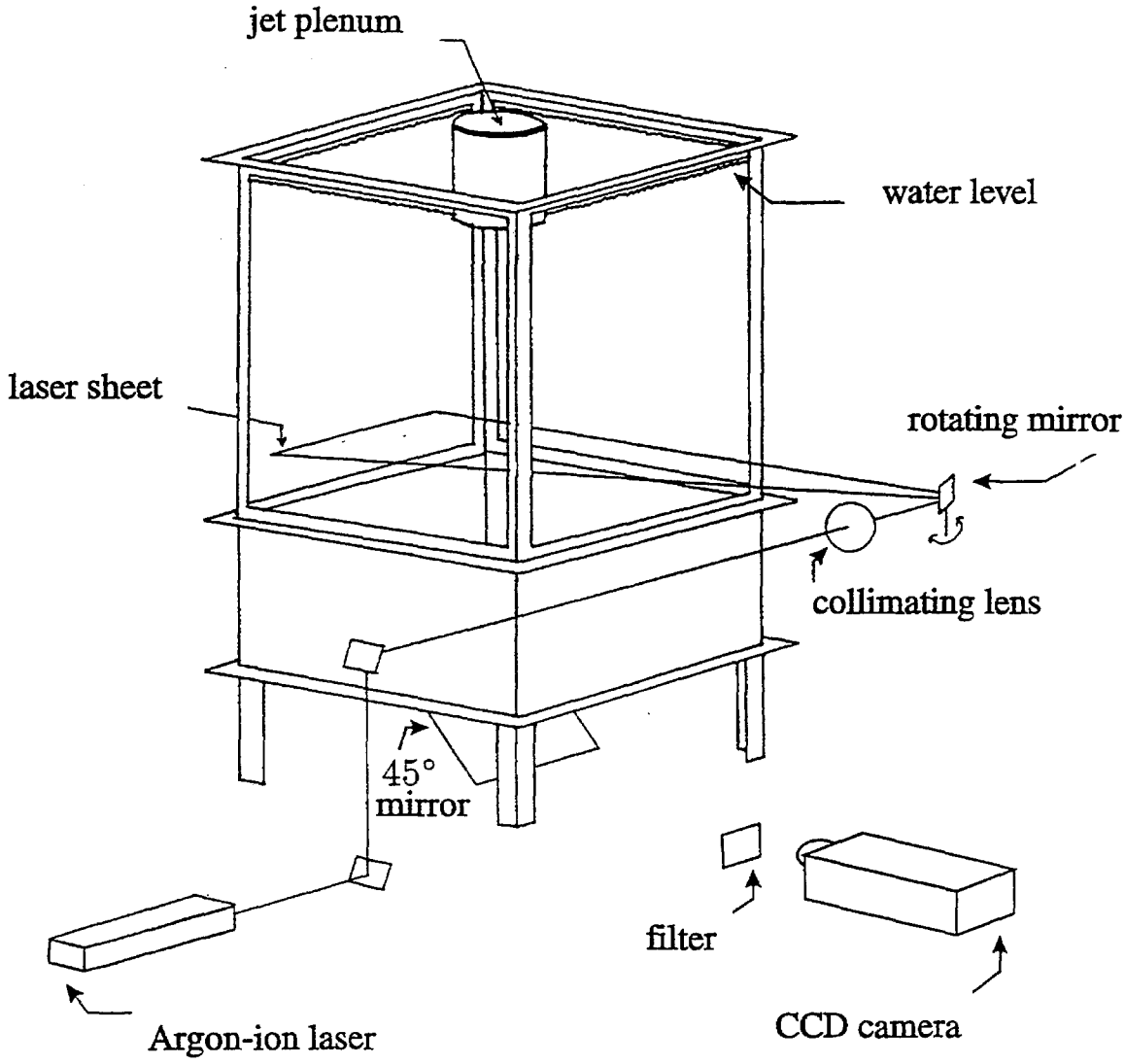

FIGURE 1 Jet facility and diagnostics schematic.

turbulent-mixing time scales in these experiments. The fluorescence is emitted at a longer wavelength than the excitation radiation, where the dye is characterized by a negligible absorption cross-section. Consequently, the mixed fluid is in the optically thin regime as far as fluorescence emission is concerned (Dimotakis *et al.* 1983). At the downstream station used for these experiments ($z/d_0 = 275$), it was verified that the low plenum dye concentration resulted in a scalar fluorescent dye field with negligible laser attenuation across the field of view.

A Gaussian (TEM_{00}) beam from a continuous-wave Argon-ion laser (Coherent Innova 90) was collimated by a long focal-length ($f = 1000\,\mathrm{mm}$), spherical lens to a beam waist (diameter) of $w_0 \lesssim 300\mu\mathrm{m}$ and approximately positioned in the center of the imaged field of view. The Rayleigh range for this beam was estimated to be $\pm 12.5\,\mathrm{cm}$ (on either side of the waist). The field of view spanned $\ell_0 \simeq 42\,\mathrm{cm}$, resulting in a pixel resolution of $\lambda_\mathrm{p} \simeq 420\,\mu\mathrm{m}$, and contained the full transverse spatial extent of the turbulent-jet fluid at the measuring station. This resulted in a transverse resolution that was smaller than the in-plane (pixel) resolution in the center and comparable to it near the edges of the field of view. The laser beam was swept across the jet and synchronized with the CCD camera shutter using a small-inertia, small-aperture (5 mm), galvanometrically-driven, linearly-scanned mirror (General Scanning: Mirror M0540V and scanner G120DT). Background laser light was filtered out using a low-pass optical filter (Kodak No. 22). The experiments were conducted in a dark environment to minimize noise due to ambient light.

1.3 Image calibration and normalization

The laser-induced-fluorescence image data were processed using a pixel-by-pixel calibration of the CCD array for noise, sensitivity, and laser illumination variations in the field of view. Each raw fluorescence-data image, $I_\mathrm{raw}(x,y)$, was calibrated and normalized with an ensemble-average of four background-noise images and four uniform-concentration images recorded for each run condition, *i.e.*,

$$\frac{c(x,y;z=\mathrm{const})}{c_\mathrm{ref}} = \frac{I_\mathrm{raw}(x,y) - \langle I_\mathrm{bck}(x,y)\rangle}{\langle I_\mathrm{ill}(x,y)\rangle - \langle I_\mathrm{bck}(x,y)\rangle}\,, \tag{1.1}$$

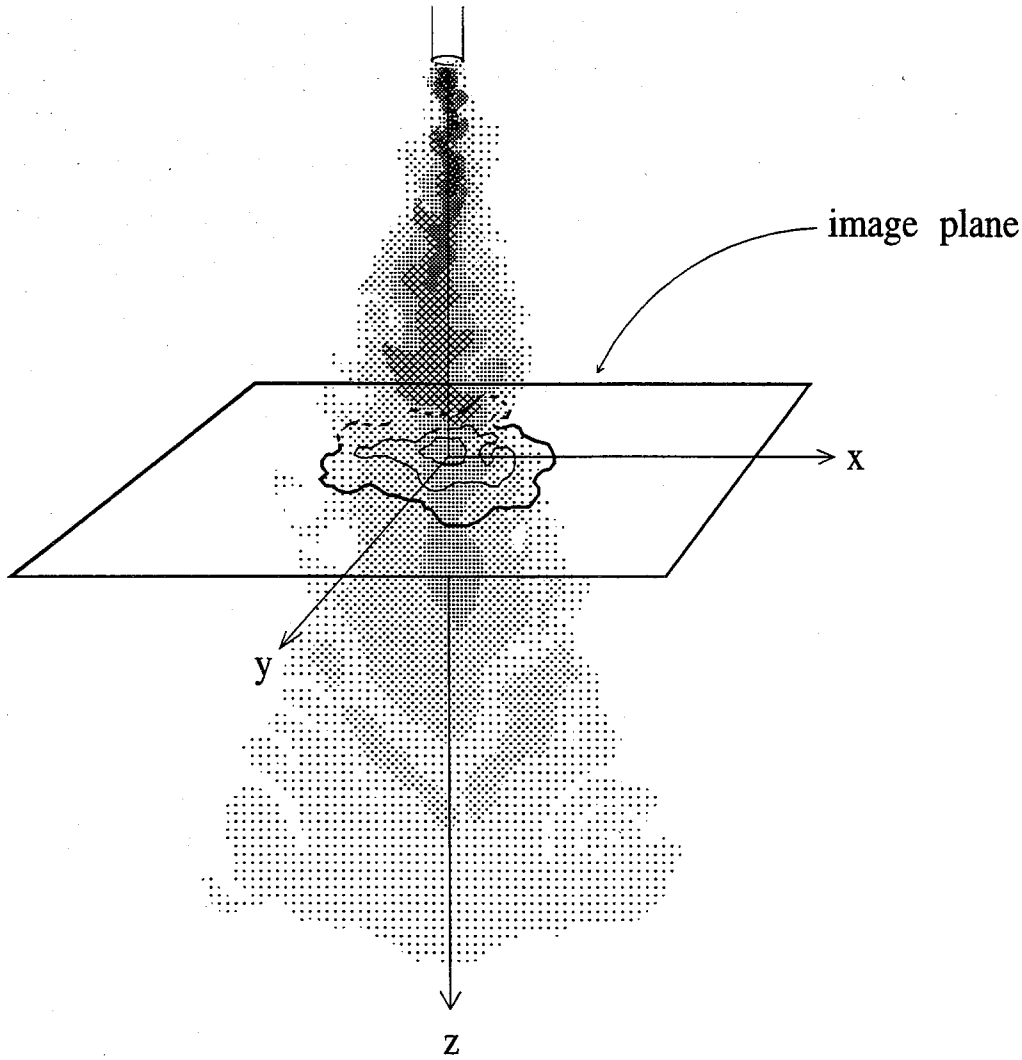

FIGURE 2 Jet scalar far-field geometry and image plane schematic.

where c_{ref} is a reference concentration that is constant for all runs, $I_{\mathrm{bck}}(x, y)$ are pre-run, "background" images, and $I_{\mathrm{ill}}(x, y)$ are post-run, "illumination" images, as described below. The background-noise images, $I_{\mathrm{bck}}(x, y)$, were recorded shortly before each run with no dye in the tank. Each such image was recorded at the same location as the (raw) jet images, along the same optical path, with the camera shutter open for the same exposure time as for the jet images. After the jet-plenum fluid had completely discharged into the tank, all of the water and dye were recirculated continuously in the tank. During the recirculation process, the laser-induced

fluorescence at the imaging station was monitored for non-uniformities of the dye concentration in the plane of illumination. After a sufficiently long time, non-uniformities were no longer measurable and images corresponding to the resulting, uniform-concentration dye field were recorded and used to measure the illumination and optical collection efficiency distribution in the field of view, $I_{\rm ill}(x,y)$, as well as provide an absolute, jet-fluid concentration reference. The procedure of emptying all the (fixed-volume) jet-plenum fluid into the tank ensured that $c_{\rm ref}$ was the same for all runs, and allowed the local scalar values, $c(x,y)$, to be referenced, in absolute value, to the (pure) jet-plenum concentration, c_0, *i.e.*,

$$\frac{c(x,y)}{c_0} = \frac{c(x,y)}{c_{\rm ref}}\,\frac{c_{\rm ref}}{c_0} = \frac{c(x,y)}{c_{\rm ref}}\,\frac{V_{\rm plenum}}{(V_{\rm tank}+V_{\rm plenum})} \simeq \frac{c(x,y)\,/\,c_{\rm ref}}{2.2\times 10^2}\ , \qquad (1.2)$$

where $V_{\rm plenum} \simeq 5.0\times 10^{-3}\,{\rm m}^3$ is the plenum volume and $V_{\rm tank} \simeq 1.1\,{\rm m}^3$ is the tank volume.

1.4 Reynolds numbers investigated

The Reynolds number, Re, is a flow (and fluid) parameter that is defined, for round, momentum-driven, turbulent jets, at a downstream distance z, as,

$$Re \equiv \frac{u(z)\,\delta(z)}{\nu}\ , \qquad (1.3)$$

in terms of the (local) jet centerline velocity, $u(z) \propto 1/z$, the (local) jet transverse extent (diameter), $\delta(z) \propto z$, and the kinematic viscosity of the fluid, ν. The Reynolds number in this case is, therefore, independent of the downstream coordinate, z, and, $Re \simeq Re_0$, where $Re_0 \equiv u_0\,d_0\,/\nu$ is the Reynolds number based on jet-nozzle values. The jet Reynolds number was varied in these investigations in the range,

$$4.5\times 10^3 \ \le\ Re\ \le\ 18\times 10^3\ , \qquad (1.4)$$

with measurements at three values: $Re \simeq 4.5\times 10^3$, 9.0×10^3, and 18×10^3.

1.5 Scalar-species Schmidt number

The Schmidt number, Sc, is a characteristic of the ambient fluid and of the scalar species (as opposed to the flow) and is defined as,

$$Sc \equiv \frac{\nu}{\mathcal{D}} , \tag{1.5}$$

where ν is the kinematic viscosity of the fluid ($\nu = \mu/\rho$, the ratio of dynamic viscosity, μ, to density, ρ) and $\mathcal{D}$ is the diffusivity of the scalar species into the ambient fluid. This dimensionless number is a relative measure, therefore, of momentum (vorticity) diffusion to scalar-species diffusion.

For the present experiments, the working fluid is a liquid (filtered, softened water) at a room temperature in the range $(20 \pm 2)\,^{\circ}\mathrm{C}$, with $\nu \simeq 9.9 \times 10^{-3}\ \mathrm{cm}^2/\mathrm{sec}$. The aqueous diffusion coefficient for the scalar species (disodium fluorescein) is, $\mathcal{D} \simeq 5.2 \times 10^{-6}\ \mathrm{cm}^2/\mathrm{sec}$ (*cf.* Ware *et al.* 1983, p. 280). The scalar-species Schmidt number is estimated to be, therefore,

$$Sc \simeq 1.9 \times 10^3 , \tag{1.6}$$

which reflects the fact that the diffusion of the scalar species occurs on a much longer time scale than the diffusion of momentum (or vorticity).

The high Schmidt number of these investigations, $Sc \sim O(10^3) \gg 1$, is characteristic of mixing in the liquid-phase (*i.e.*, of miscible liquids) as well as of mixing of solid particulates in the liquid or gas flows, *e.g.*, dispersion of aquatic organisms such as planktonic larvae in the ocean (*e.g.*, Denny 1988). Gas-phase mixing (*i.e.*, when both the ambient fluid and the scalar species are gases) is associated with a low Schmidt number, $Sc \simeq 1$ (*e.g.*, Tritton 1988). High Schmidt number turbulent mixing can be expected to result in a more complex isosurface geometry, as compared to low Schmidt number mixing (for a given flow, at a given Reynolds number), since scalar-field inhomogeneities will be smoothed out to a smaller extent (lower species diffusivity) in the former case.

1.6 Examples of scalar-field images

Examples of turbulent-jet scalar-image data at $Re \simeq 4.5 \times 10^3$, 9.0×10^3, and 18×10^3 are depicted in color in figures 3, 4ab, and 5, respectively. The image data have been normalized and calibrated; *cf.* equation (1.1). Black denotes the reservoir fluid into which the jet is discharging. Pale yellow, red, green and blue indicate successively lower levels of jet fluid concentration.

Throughout the Reynolds number range investigated, the image field of view was the same. At $Re \simeq 9.0 \times 10^3$ (*cf.* figure 4), scalar diffusion-layer thickness scales (half-wavelength) on the jet centerline are estimated to be approximately half the pixel resolution, and much larger than the pixel resolution near the outer region of the jet. Also, at this Reynolds number, the time for the passage of these scales is estimated to be a factor of 30 times longer than the exposure time of an individual pixel, on the jet axis, and even longer near the boundary of the jet. The images were acquired maintaining a constant product of the beam-scanning time, which scaled the time exposure per pixel, and the local flow velocity, over the Reynolds numbers investigated. These choices provided temporally- as well as spatially-resolved measurements of the scalar field, throughout the Reynolds number range, certainly in the outer region of the jet where these investigations were primarily focused, with minor compromises in spatial resolution in the vicinity of the highest-velocity/-concentration (interior) regions of the jet.

1.7 Scalar power spectra

The two-dimensional, scalar power spectrum, $S_c^{(2)}(\kappa_x \ell_0, \kappa_y \ell_0)$, for the image data of figure 4 is shown in figure 6. Contour values shown range from -8.5 to -6.0 (outer to inner) in increments of 0.5, in units of $\log_{10}\left(\ell_0^2\, c_{\rm ref}^2\right)$. The contours are approximately circular, consistent with a statistically-axisymmetric scalar field. These spectra have been normalized such that the zero-wavenumber value of the power spectrum recovers the mean-field value of the scalar image data, *i.e.*,

$$\left[S_c^{(2)}(0,0)\right]^{1/2} = \langle\, c \,\rangle \ , \tag{1.7}$$

where $\langle\, c \,\rangle$ denotes the spatial (field-of-view) average of the scalar-field values, estimated directly from the data.

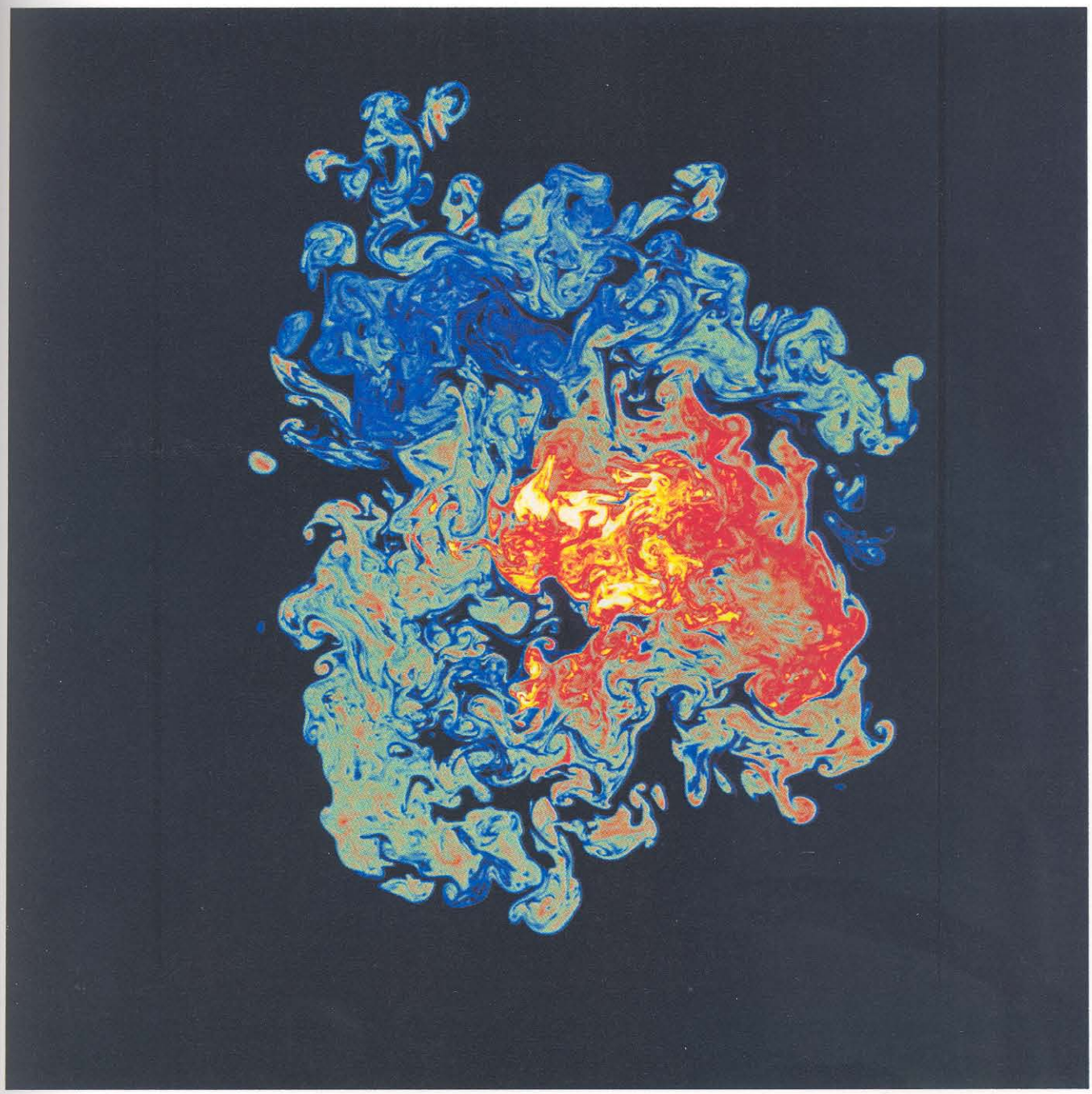

FIGURE 3 Jet-fluid concentration in the far-field ($z/d_0 = 275$) of a turbulent jet at $Re \simeq 4.5 \times 10^3$.

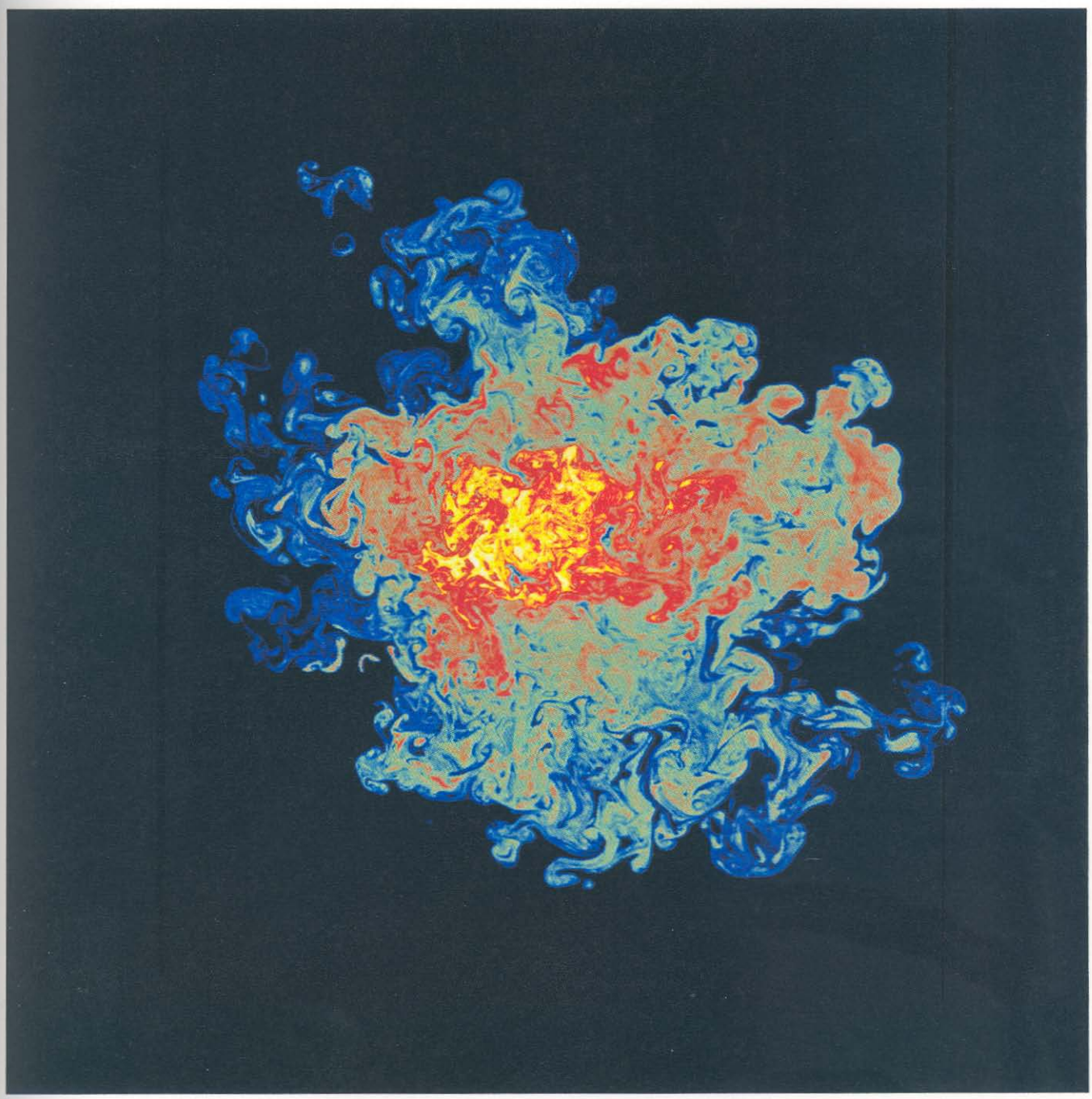

FIGURE 4 (a) Jet-fluid concentration in the far-field ($z/d_0 = 275$) of a turbulent jet at $Re \simeq 9.0 \times 10^3$.

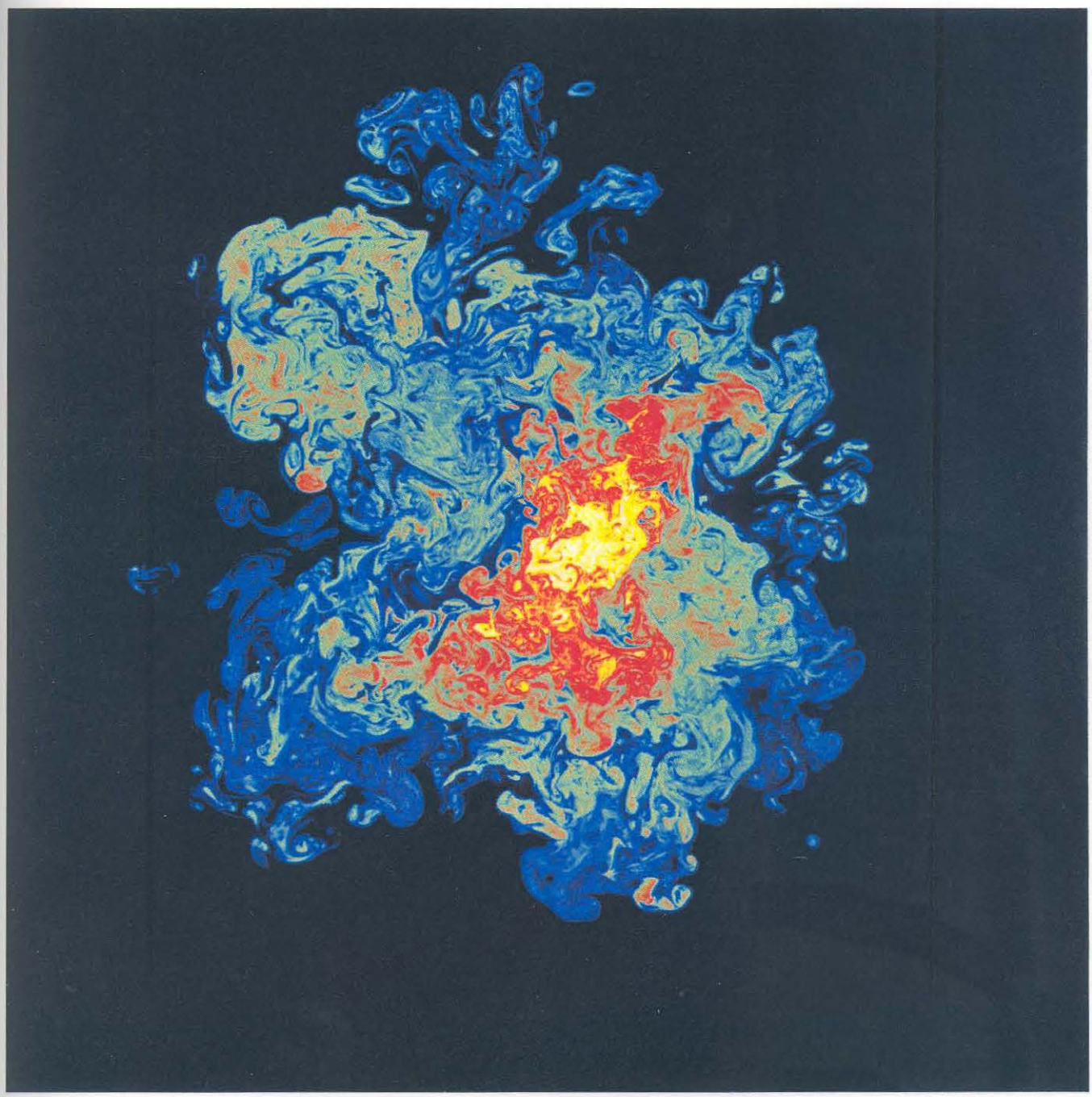

FIGURE 4 (b) A different image realization at the same Reynolds number and downstream location as for (a).

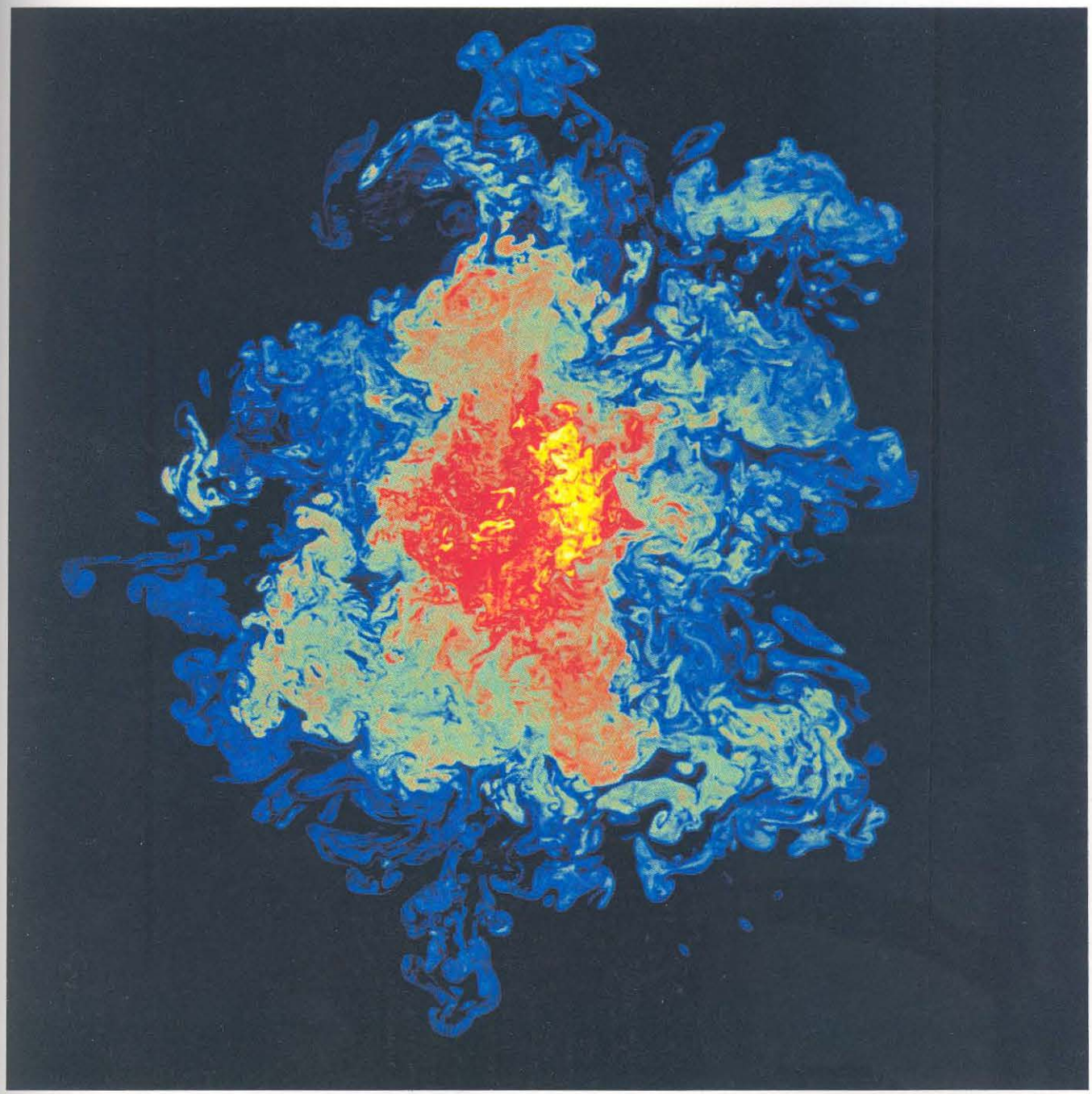

FIGURE 5 Jet-fluid concentration in the far-field ($z/d_0 = 275$) of a turbulent jet at $Re \simeq 18 \times 10^3$.

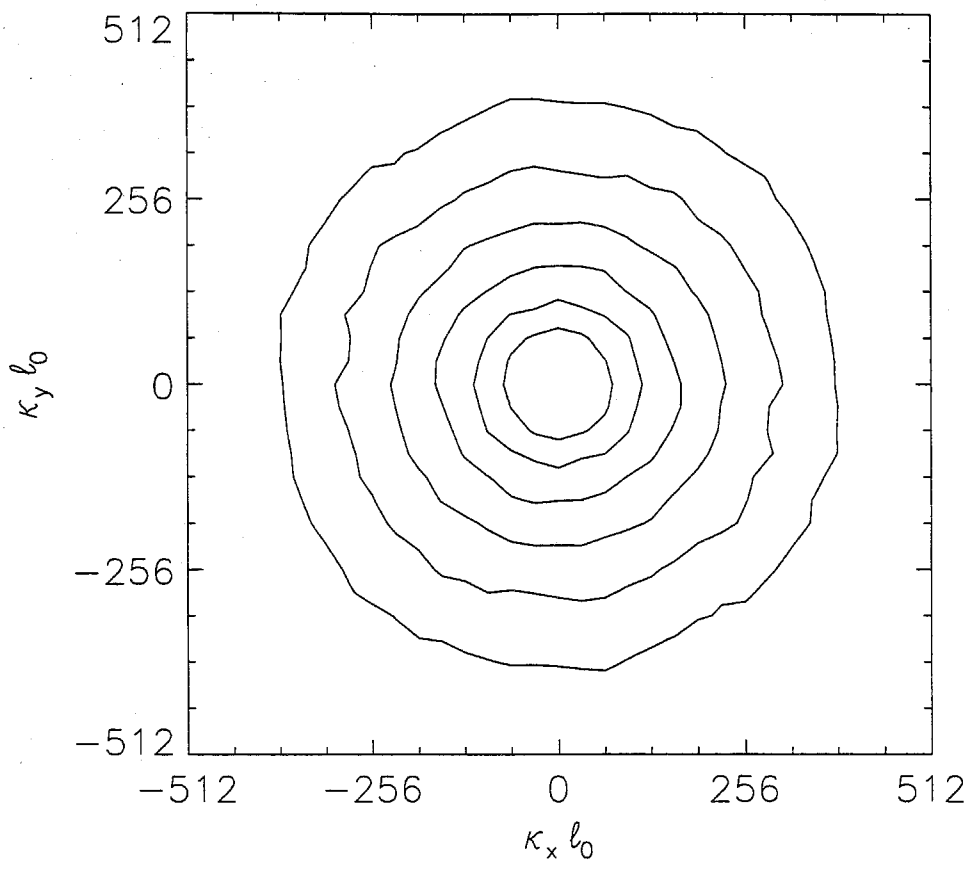

FIGURE 6 Contour plot of the (decimal) logarithm of the two-dimensional, spatial scalar power spectrum of the image data depicted in figure 4 ($\ell_0 = 42\,\mathrm{cm}$ denotes the spatial extent of the field-of-view).

It was also verified that the integral (sum) over the two-dimensional wavenumber space recovers the spatially-averaged scalar variance, $\langle\, c'^2 \,\rangle$, which was estimated directly from the image data, *i.e.*,

$$\sum_{\kappa_x \ell_0} \sum_{\kappa_y \ell_0} S_c^{(2)}(\kappa_x \ell_0, \kappa_y \ell_0) \;=\; \langle\, c'^2 \,\rangle \;, \tag{1.8}$$

where these summations extend over the normalized-wavenumber range, $\kappa_x \ell_0, \kappa_y \ell_0 = \pm 1, \ldots, \pm(1024/2 - 1)$, *i.e.*, exclude the zero-wavenumber spectrum value corresponding to the (mean-field) $(i, j) = (0, 0)$ scalar-field value.

Radial scalar power spectra, $S_c(\kappa \ell_0)$, where $\kappa = \sqrt{\kappa_x^2 + \kappa_y^2} = k/2\pi$ is the radial

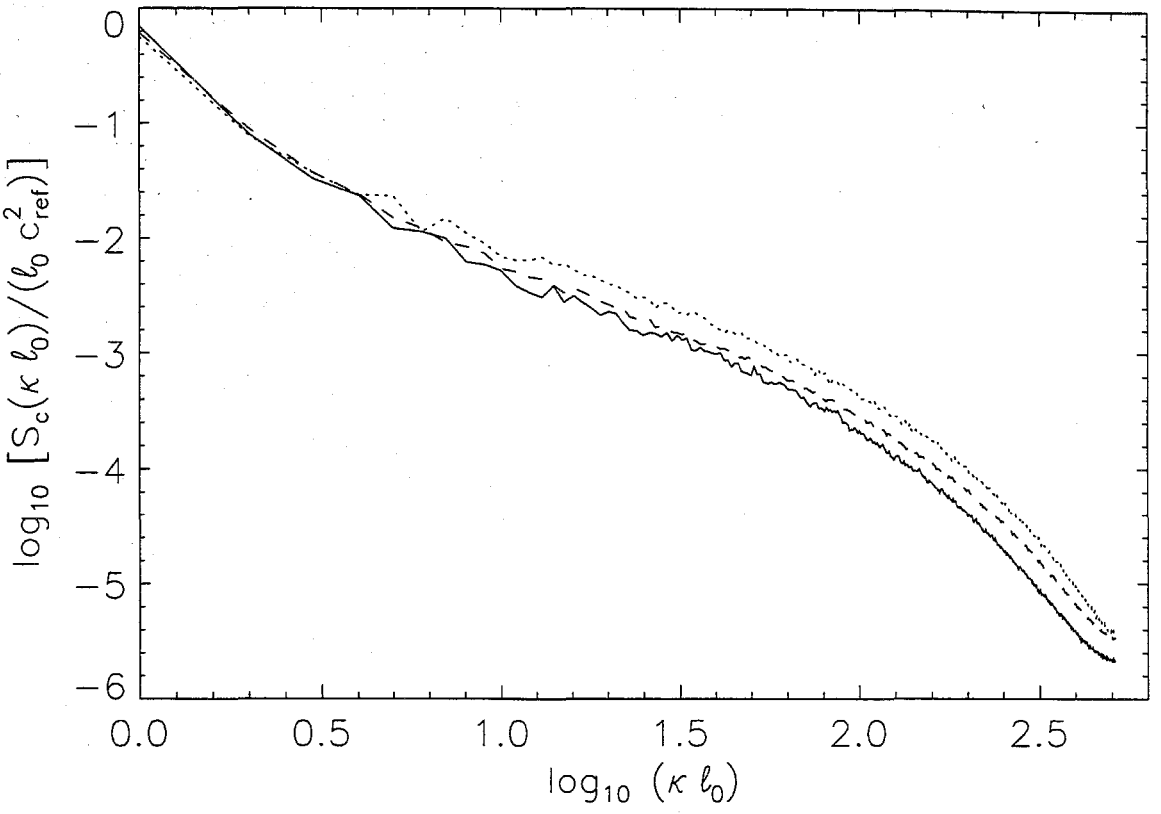

FIGURE 7 Ensemble-averaged radial scalar power-spectra. $Re \simeq 4.5 \times 10^3$: dotted line; $Re \simeq 9.0 \times 10^3$: dashed line; $Re \simeq 18 \times 10^3$: solid line.

wavenumber, for the three Reynolds numbers investigated (ensemble-averaged from six individual-image realizations at $Re \simeq 9.0 \times 10^3$, and three realizations at $Re \simeq 4.5 \times 10^3$ and $Re \simeq 18 \times 10^3$), are shown in figure 7. These were estimated by an azimuthal, constant-κ integration (shell-sum) of the corresponding, two-dimensional scalar power spectra (*cf.* figure 6), *i.e.*,

$$S_c(\kappa\ell_0) \equiv 2\pi \left\langle \tilde{S}_c^{(2)}(\kappa\ell_0, \theta) \right\rangle_\theta \kappa\ell_0 \ , \tag{1.9}$$

where $\langle\ \rangle_\theta$ denotes the azimuthal (shell) average, and,

$$\tilde{S}_c^{(2)}(\kappa\ell_0, \theta) \equiv S_c^{(2)}(\kappa\ell_0 \cos\theta, \kappa\ell_0 \sin\theta) \ , \tag{1.10}$$

cf. equation (1.8). These (one-dimensional) radial scalar power spectra are normalized so that the integral of $S_c(\kappa\ell_0)$ over a radial-wavenumber range recovers the integral of the two-dimensional scalar power spectra over the corresponding

wavevector $(\kappa_x \ell_0, \kappa_y \ell_0)$ range, *i.e.*,

$$\sum_{\kappa \ell_0} S_c(\kappa \ell_0) \;=\; \sum_{\kappa_x \ell_0} \sum_{\kappa_y \ell_0} S_c^{(2)}(\kappa_x \ell_0, \kappa_y \ell_0) \;=\; \langle\, c'^2 \,\rangle \;, \tag{1.11}$$

cf. equation (1.8), where the summations in equation (1.11) extend over a disk region centered at the (zero-wavenumber) origin in wavenumber space excluding the origin.

The shape of these (radial) spectra reflects, in part, the spatial extent of the imaged jet-fluid concentration field, which is not a spatially (statistically) homogeneous field. In particular, embedding the image data in a larger (*e.g.*, 2048^2-pixel) domain (with zero values in the extended region) would affect the behavior at small wavenumbers. Such an embedding was performed and it was found that the (radial) spectrum tends to a constant (*i.e.*, levels off) at small wavenumbers, whose value decreases as the size of the embedding domain increases. The spectrum behavior at moderate or large wavenumbers, however, was only weakly affected (for the 2048^2-pixel extended domain).

In the limit of an infinite embedding domain, the (compact-support and finite) jet-fluid concentation field would be localized at the origin, whose 2-D spectrum would be a constant, resulting in zero value of the (2-D) spectrum as $\kappa \rightarrow 0$ (this would also be the limiting value of the radial spectrum). Note that, if the (2-D) spectra were continuous, the radial spectra would also tend to 0 as $\kappa \rightarrow 0$, for any domain size, by virtue of the definition of the radial spectrum (*cf.* multiplication by κ in equation (1.9)). It is, therefore, the discrete nature of the present spectra (and the finite extent of the imaged jet-fluid concentration field) that result, in part, in the shape of the radial spectra in figure 7.

At high wavenumbers, a decrease of the spectra with increasing Reynolds number is evident from figure 7. This effect is not a consequence of inadequate resolution; the spatial spectra diverge at rather low wavenumbers, with a separation that does not appreciably increase with wavenumber and, in particular, is not characteristic of fixed-pole, low-pass filtering. The dynamic range of the scalar image data can be seen to be, approximately, 50 dB, corresponding to a signal-to-noise (amplitude) ratio of 300:1.

The Reynolds number dependence of the scalar power spectra in figure 7 is consistent with the notion of increased molecular mixing, resulting in a decrease in scalar variance with increasing Reynolds number, previously documented on the basis of (temporal) scalar fluctuation measurements on the centerline of liquid-phase, turbulent jets (*cf.* Miller & Dimotakis 1991b). Notably, this behavior is not encountered in gas-phase jets, in the same Reynolds number range, and must, therefore, be attributed to the lower (liquid-phase) molecular diffusivity, *i.e.*, Schmidt number effects (*cf.* Miller 1991, figure 7.2 and related discussion).

CHAPTER 2

Turbulent mixing: classical scalar measures

The two-dimensional, spatial measurements of the jet-fluid concentration allow an investigation of the structure of turbulent mixing in the similarity plane of liquid-phase jets. Knowledge of statistics in any one such (constant-z) plane, in the far field, is enough to provide the statistics in any other, constant-z plane (in the far field). In this chapter, some classical measures of the scalar field, as well as of the isoscalar (level-set) surfaces, are analyzed: the probability-density function of the scalar field, the area enclosed by the scalar level sets, and a measure of the (maximum) isoscalar spatial extent or largest scale. While the first two measures are directly related, they offer complementary insight into the structure of turbulent mixing. The third measure provides a length scale appropriate for the normalization of various (fractal) coverage statistics (*cf.* chapters 3, 4, and 5). The Reynolds-number and scalar-threshold dependence of these measures is investigated. Several of the characteristics of these measures are also discernible, directly, in the isosurfaces superimposed on the scalar-field image data, examples of which are included. Additional measures of the multiscale geometry of the isosurfaces, such as scale-dependent-fractal (SDF) dimensions or volume-fill fraction, and their relation to the scale distribution, as well as other measures of geometric structure and complexity, are discussed in chapters 3, 5, and 6.

2.1 Scalar probability density function

The jet-fluid-concentration probability-density function (pdf), estimated as a histogram of the scalar values over the imaged field, is shown in figure 8 for the Reynolds numbers investigated. This was computed from ensemble-averaged histograms of six scalar images for $Re \simeq 9.0 \times 10^3$ and from three scalar images for $Re \simeq 4.5 \times 10^3$ and $Re \simeq 18 \times 10^3$ (*cf.* figures 3, 4, and 5). Lines of increasing solidity denote increasing Reynolds number. The scalar values are normalized by a constant reference concentration, c_{ref}, where $c_{\mathrm{ref}}/c_0 \simeq 2.2 \times 10^2$; *cf.* equation (1.2). Low scalar values in figure 8 are generally encountered in the outer portion of the images (tank fluid), while high values are encountered in the interior of the images near the jet centerline, as indicated in figures 3, 4, and 5.

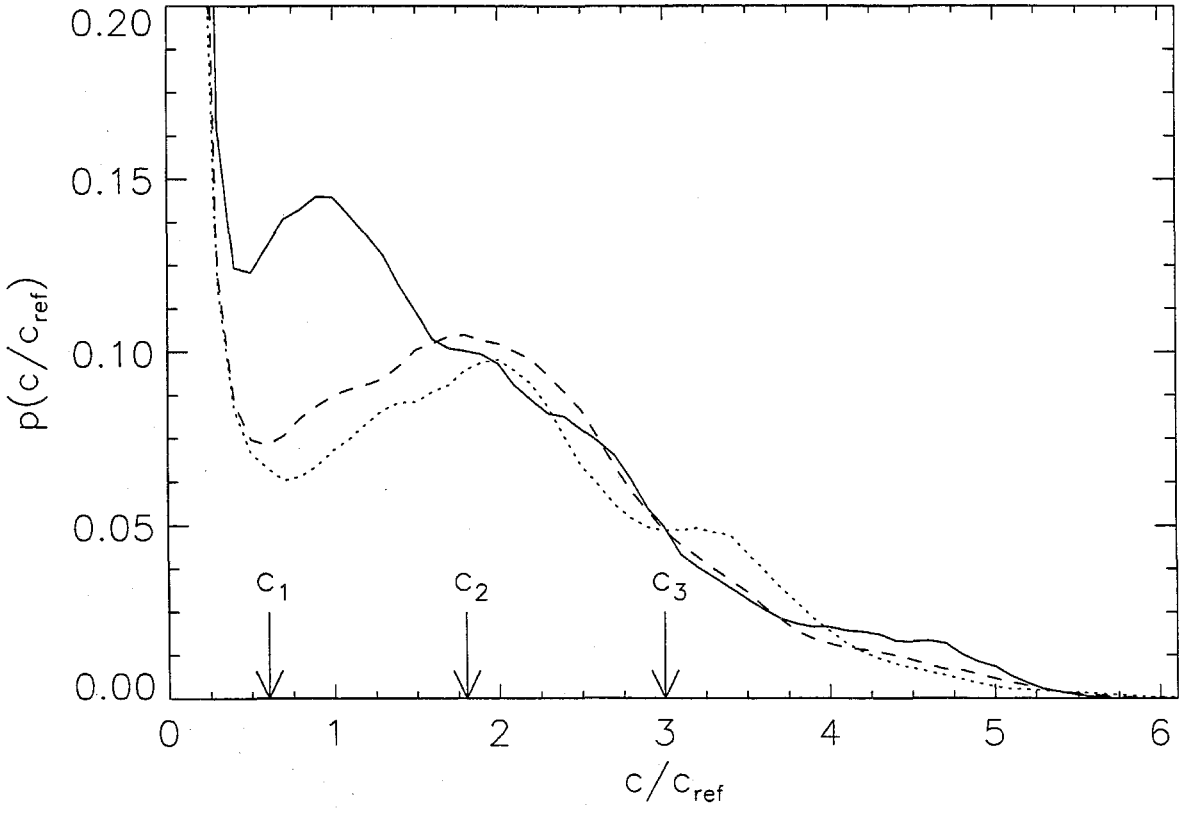

FIGURE 8 Jet-fluid concentration pdf in the far-field ($z/d_0 = 275$) of a turbulent jet, as a function of Reynolds number. $Re \simeq 4.5 \times 10^3$: dotted line; $Re \simeq 9.0 \times 10^3$: dashed line; $Re \simeq 18 \times 10^3$: solid line. Three scalar-threshold values, c_1, c_2, and c_3, are also indicated.

Figure 8 shows that, in the Reynolds number range investigated, the shape of the scalar pdf changes qualitatively with increasing Reynolds number. The peak of the mixed-fluid concentration pdf shifts to lower values, with a relatively well-defined mixing transition occurring between $Re \simeq 9.0 \times 10^3$ and $Re \simeq 18 \times 10^3$. The pdf values depicted in figure 8 are normalized over the field-of-view, which is the same for all images. Figure 8 shows that the (mixed-fluid) pdf values increase with increasing Reynolds number. This implies that the (mixed) jet-fluid concentration scalar field covers a larger fraction of the imaged region with increasing Reynolds number. The change in the nature of the scalar pdf with increasing Reynolds number, evident in figure 8, occurs in the same range of Reynolds numbers which has been documented to produce a transition to fully-developed turbulence in jets as well as other flows (*cf.* Dimotakis 1993).

The scalar-pdf behavior in figure 8 indicates that isoscalar measures can be expected to be threshold as well as Reynolds-number dependent. In the subsequent analysis, three representative scalar thresholds were chosen for the computation of scalar and isoscalar measures: $c_1/c_{\rm ref} = 0.6$, $c_2/c_{\rm ref} = 1.8$, and $c_3/c_{\rm ref} = 3.0$, as indicated in figure 8. The intermediate threshold, c_2, corresponds to the peak of the pre-transition pdf's, *i.e.*, at $Re \simeq 9.0 \times 10^3$ and $Re \simeq 4.5 \times 10^3$. The lowest threshold, c_1, corresponds to the outer isosurfaces for all Reynolds numbers investigated and to the vicinity of the local minimum of the pdf for the lower Reynolds numbers, for which PLF behavior has been reported (*cf.* Sreenivasan 1991). The high threshold, c_3, was chosen to investigate high-level behavior, mindful to avoid potential spatial resolution limitations that could be encountered at higher levels yet.

2.2 Examples of isoscalar surfaces

Examples of isoscalar surfaces (contours) at $Re \simeq 4.5 \times 10^3$, for the three scalar thresholds, c_1, c_2, and c_3, are shown in figures 9a-c, respectively. The isosurfaces are superimposed on the image data of figure 3, from which they are derived. Figures 10a-c and figures 11a-c show isoscalar surfaces at $Re \simeq 9.0 \times 10^3$ and $Re \simeq 18 \times 10^3$, respectively, for scalar thresholds c_1, c_2, and c_3. These isoscalar surfaces were constructed from the measured scalar-field data using bilinear B-splines and are depicted, in these figures, using boundary-outline pixels (*cf.* Appendix A).

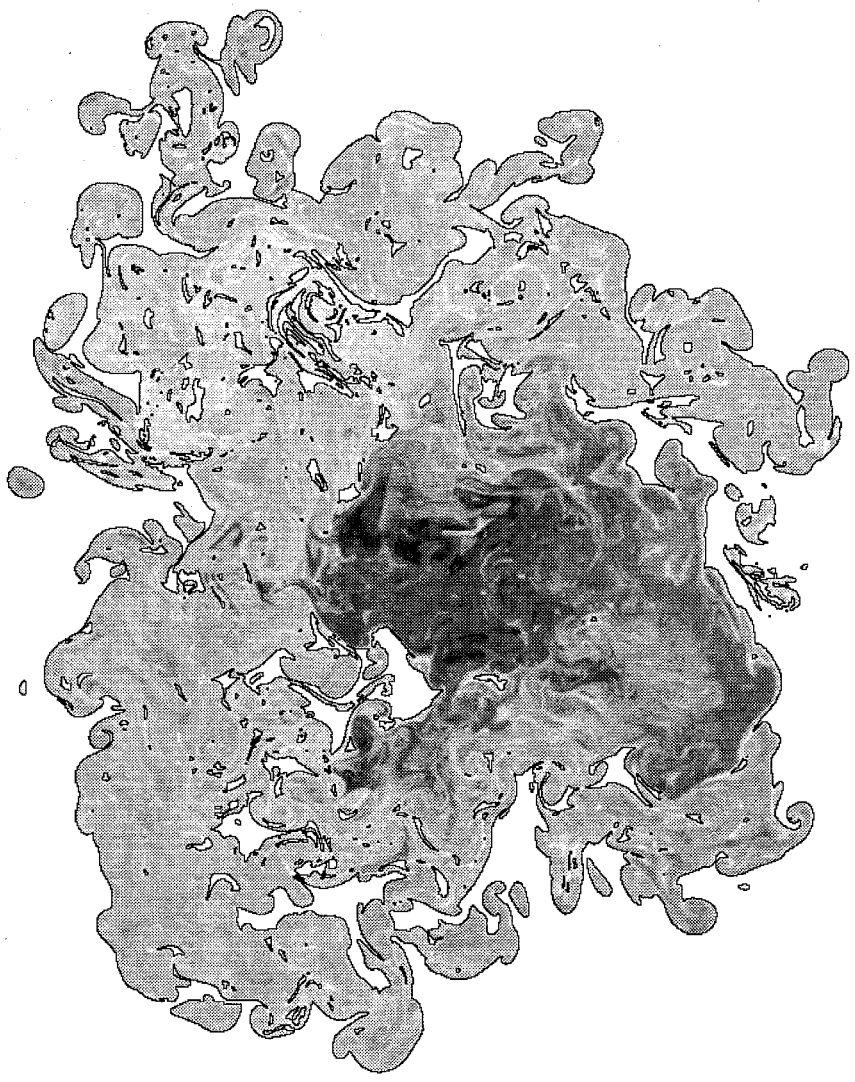

FIGURE 9 Isoscalar surface at $Re \simeq 4.5 \times 10^3$, superimposed on the image data of figure 3. (a) Threshold level, $c = c_1$.

FIGURE 9 (b) $c = c_2$.

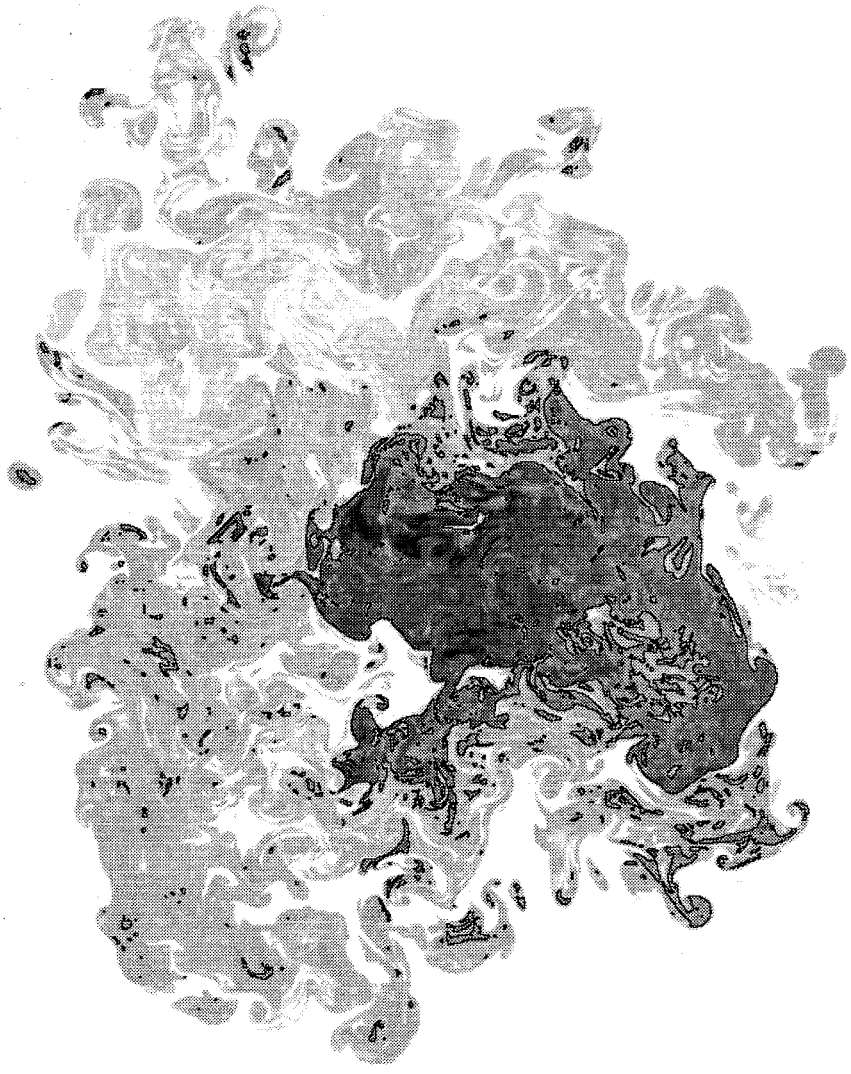

FIGURE 9 (c) $c = c_3$.

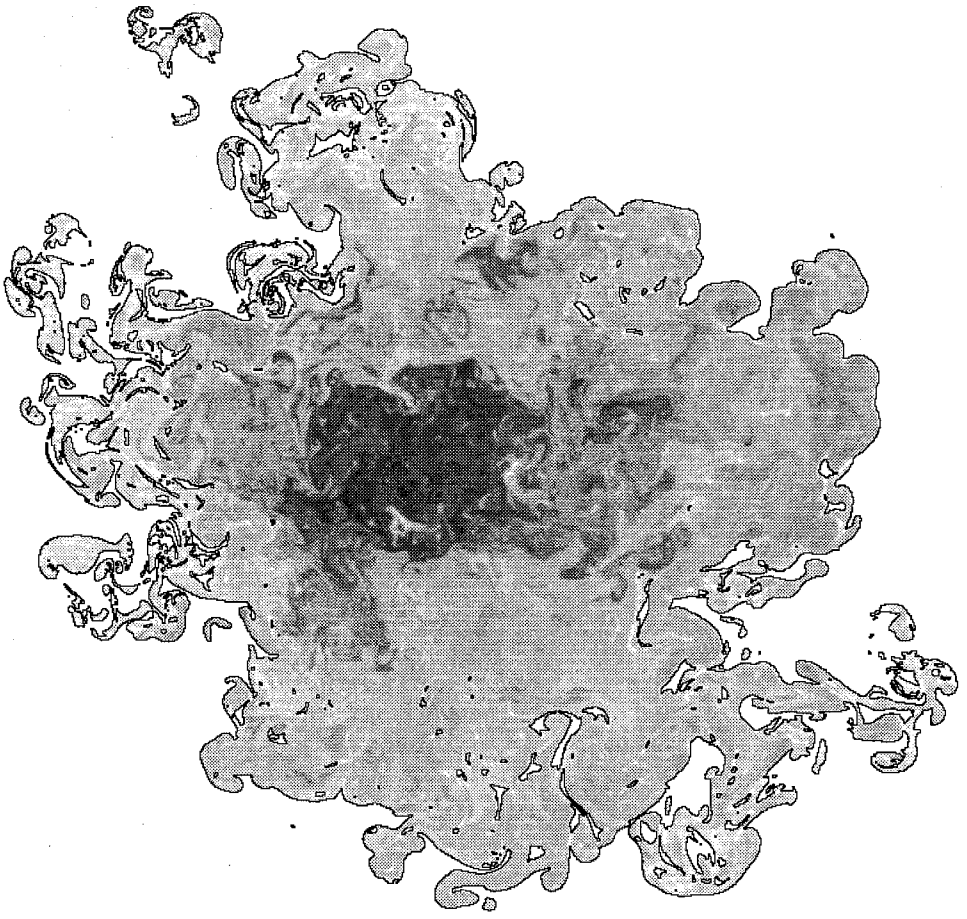

FIGURE 10 Isoscalar surface at $Re \simeq 9.0 \times 10^3$, superimposed on the image data of figure 4. (a) Threshold level, $c = c_1$.

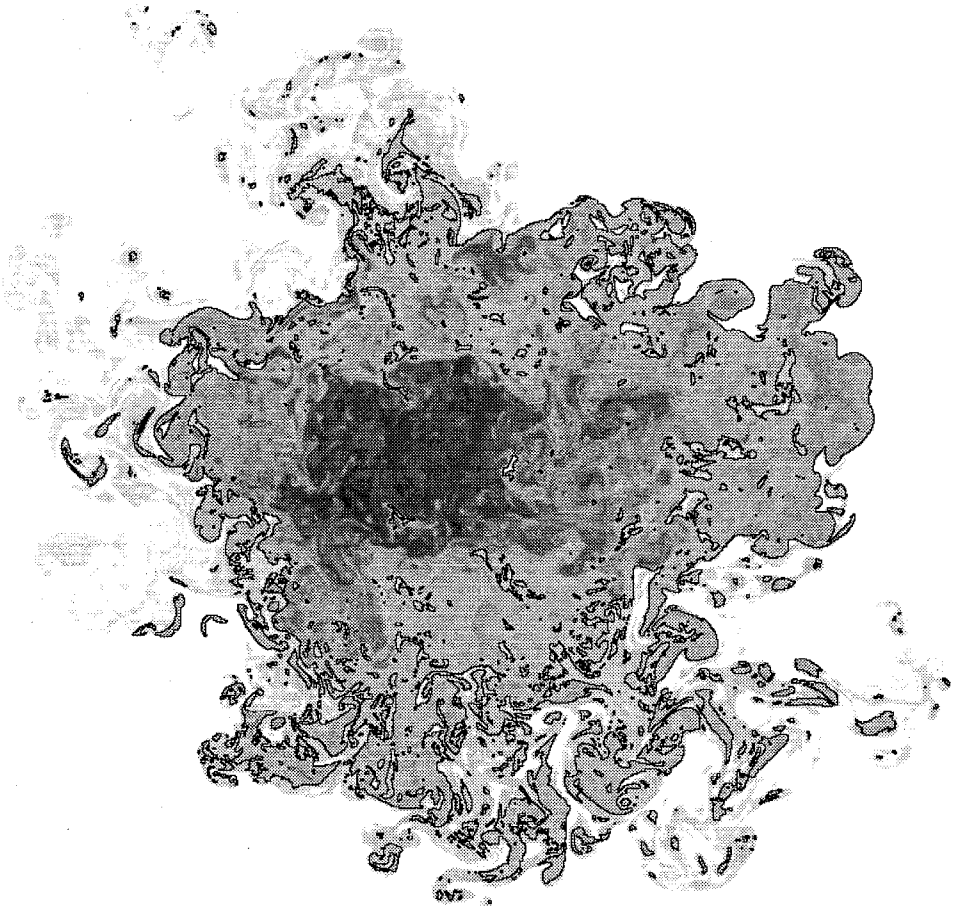

FIGURE 10 (b) $c = c_2$.

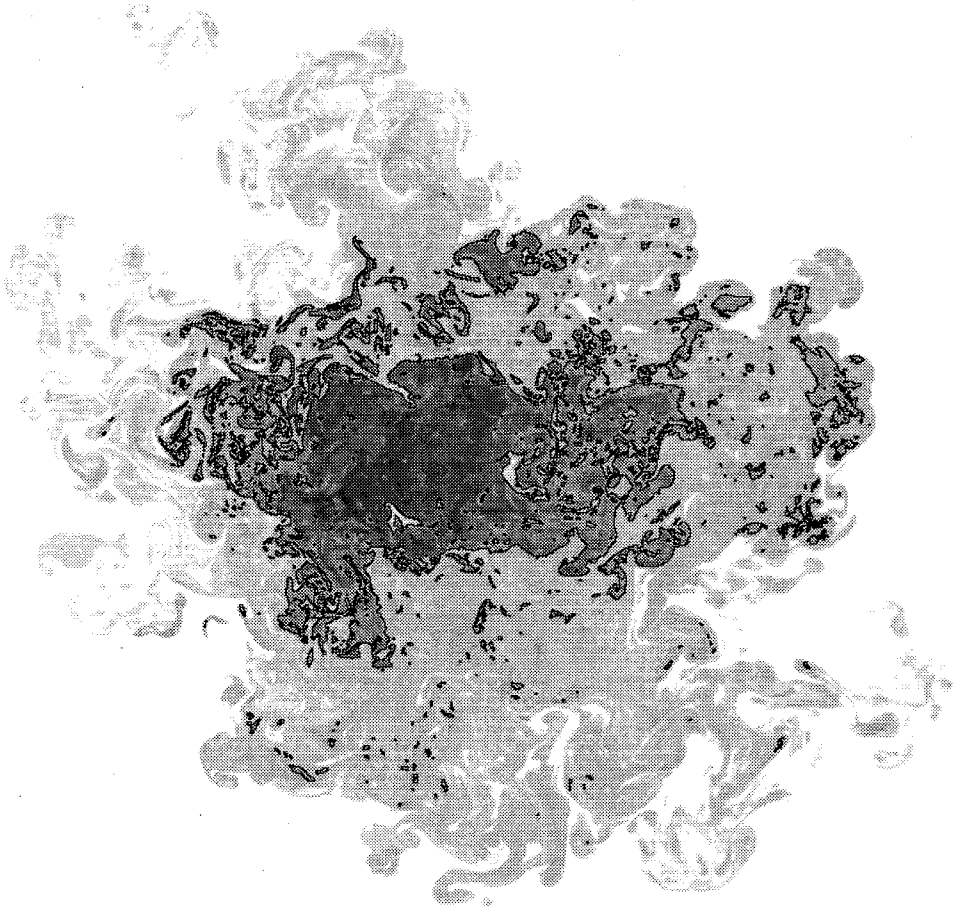

FIGURE 10 (c) $c = c_3$.

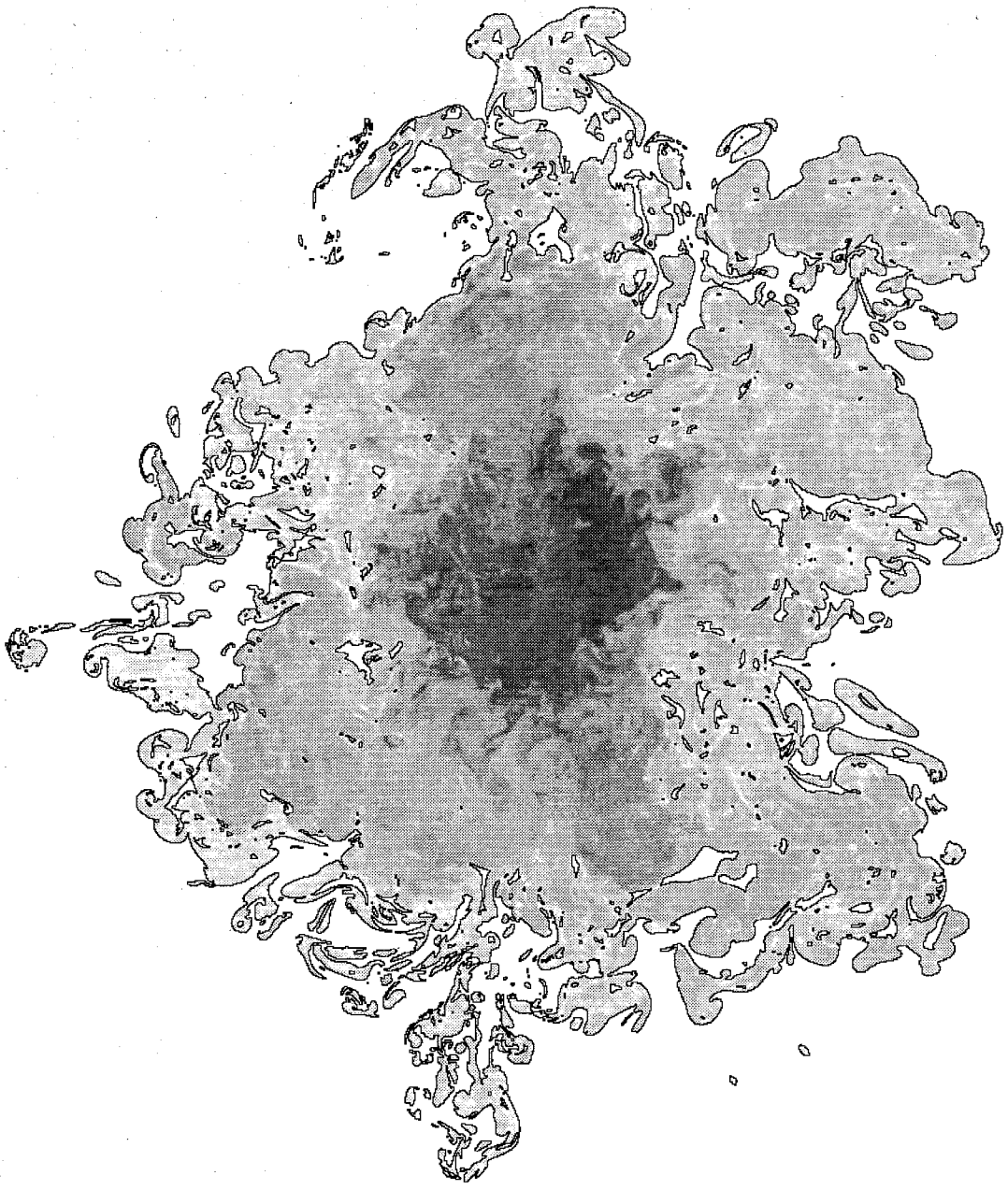

FIGURE 11 Isoscalar surface at $Re \simeq 18 \times 10^3$, superimposed on the image data of figure 5. (a) Threshold level, $c = c_1$.

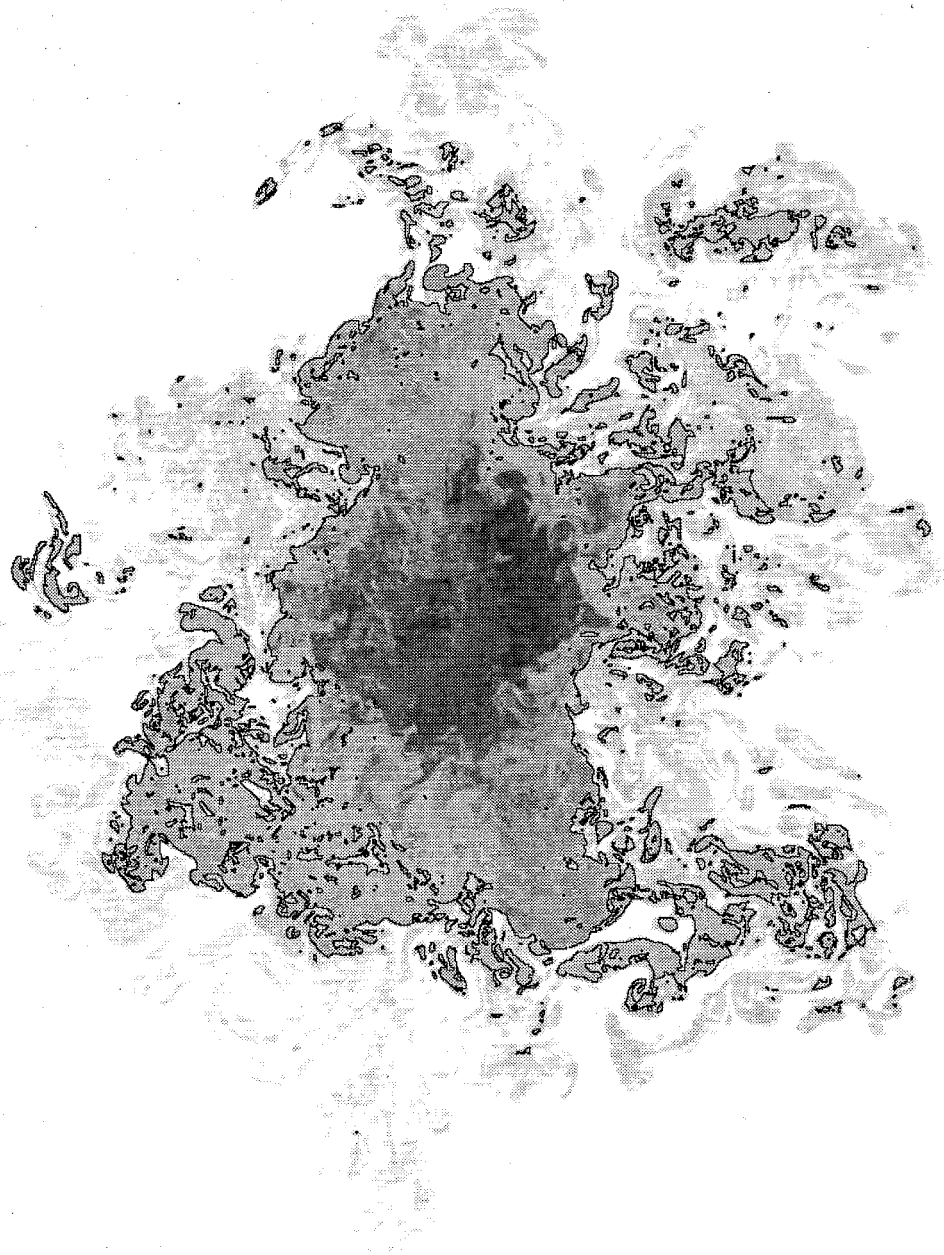

FIGURE 11 (b) $c = c_2$.

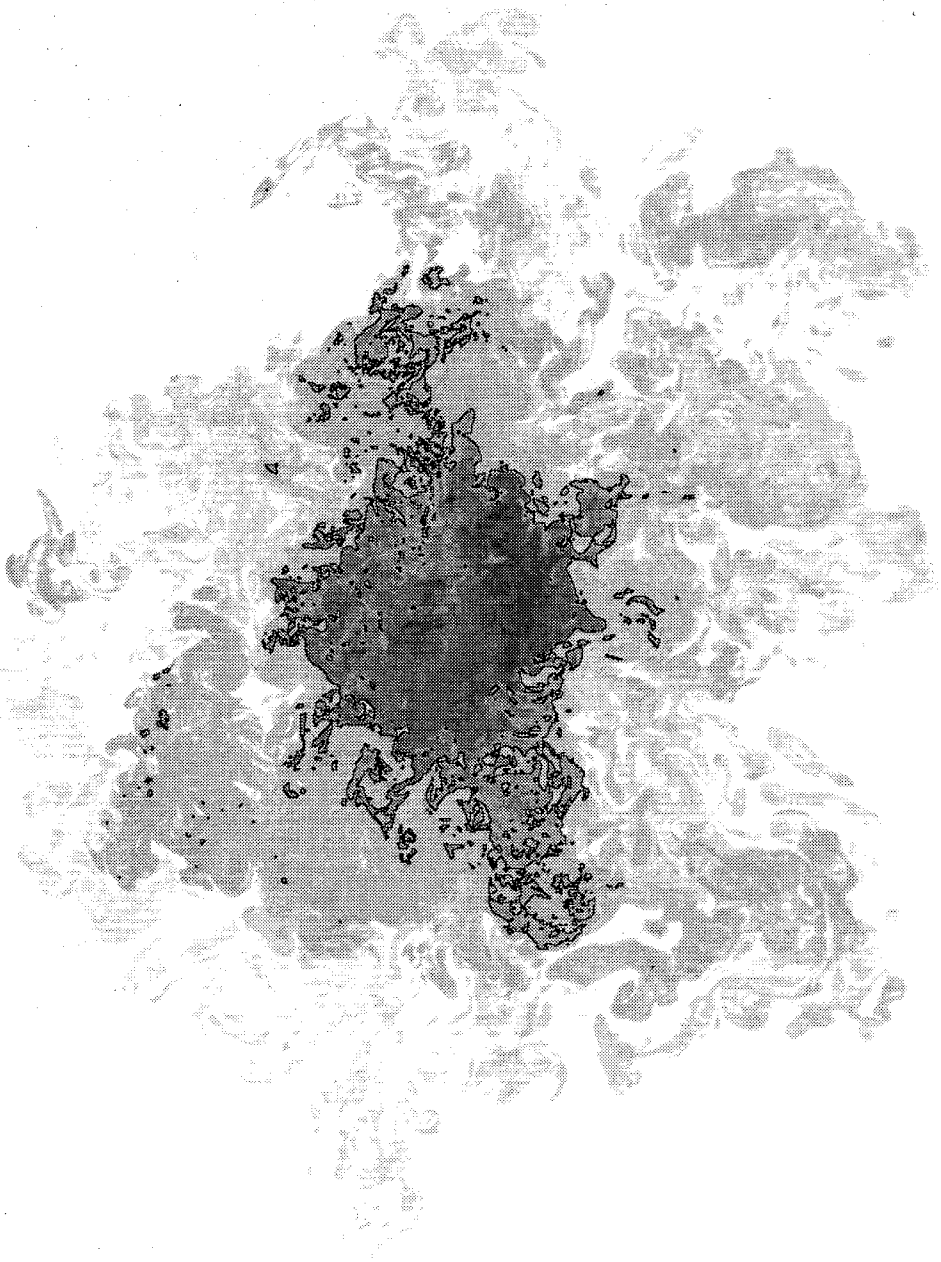

FIGURE 11 (c) $c = c_3$.

2.3 Area enclosed by scalar level sets

The area enclosed by the isoscalar surfaces (2-D level sets), at a level c, scaled by the square of the distance downstream, *i.e.*, $A(c)/z^2$, is shown in figure 12, as a function of scalar threshold and Reynolds number. This quantity was computed as the summation of the area of all regions of the scalar field with values larger-than-or-equal-to the threshold, c. For the computation of this area, the isosurfaces were represented using bilinear B-splines (*cf.* Appendix A). In the case of non-premixed hydrocarbon jet flames, for example, this area measure would represent the fraction of the cross-section occupied by unburnt jet fluid, *e.g.*, fuel, for a scalar level chosen to coincide with the stoichiometric fuel-to-air mixture fraction.

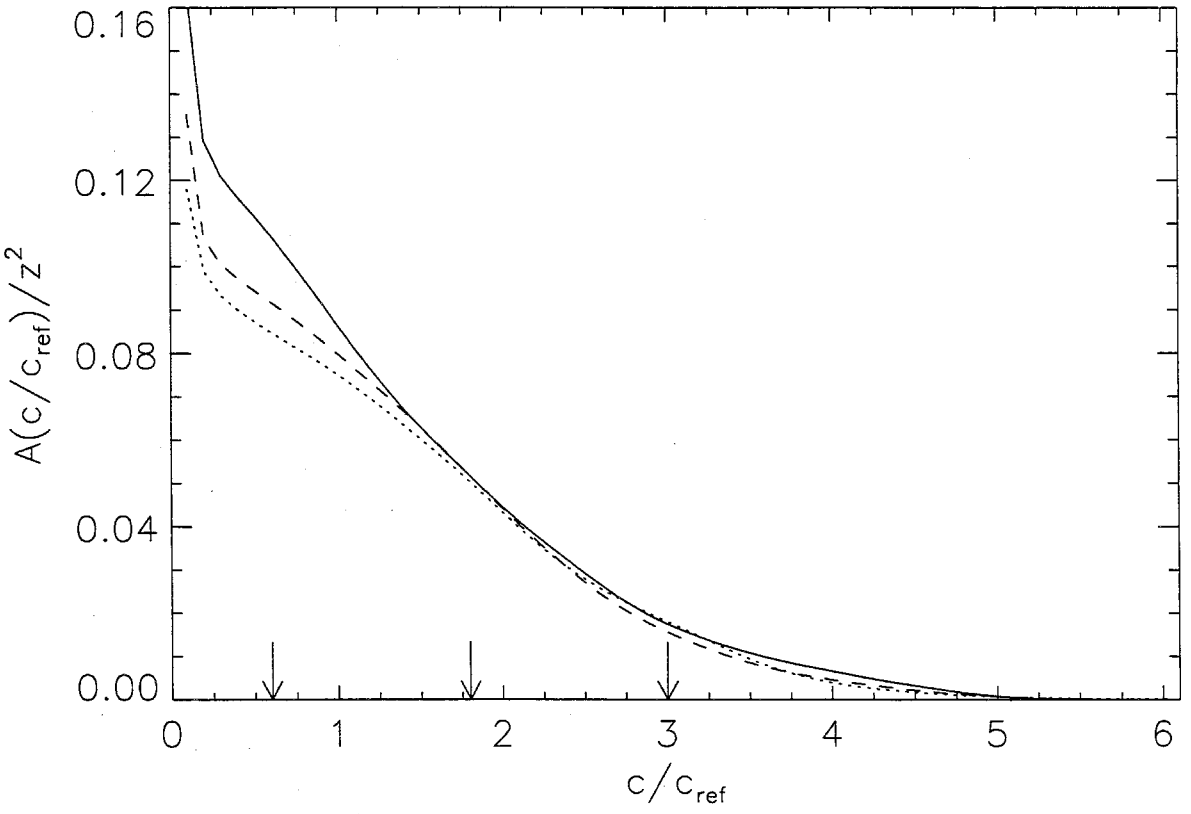

FIGURE 12 Area, A, enclosed by isoscalar surfaces as a function of scalar threshold and Reynolds number. $Re \simeq 4.5 \times 10^3$: dotted line; $Re \simeq 9.0 \times 10^3$: dashed line; $Re \simeq 18 \times 10^3$: solid line. Arrows label c_1, c_2, and c_3 scalar threshold values (*cf.* figure 8).

The area measure, $A(c)$, is an integral measure of the scalar field, representing the imaged cross-section where jet fluid has not yet mixed down to the level, c. It can also be expressed as an integral of the spatially-normalized pdf of scalar values, *i.e.*,

$$A(c)/A_0 \;=\; \int_c^\infty p(c')\,\mathrm{d}c' \;, \tag{2.1}$$

where $A_0 = \ell_0^2$ is the total area of the image field (this consistency requirement was confirmed with the two expressions independently estimated from the image data, as described above). Equation (2.1) is equivalent to the geometric interpretation of the scalar pdf, in terms of the differential area (volume) between isosurfaces separated by a differential scalar interval, *i.e.*, for these two-dimensional data, $p(c)\,\mathrm{d}c = |\mathrm{d}A(c)|/A_0$ (*e.g.*, Kuznetsov & Sabel'nikov 1990, p. 27).

The area enclosed by the outer isosurfaces, at a given threshold, is seen to increase with increasing Reynolds number. Additionally, this behavior is seen to occur in a range of lower thresholds that diminishes with increasing Reynolds number. Conversely, higher threshold regions do not exhibit conspicuous Reynolds number effects, with variations well within our statistical confidence for this measure. These observations may be explained by appreciating that lower-scalar-level isosurfaces are generally encountered in the outer regions of the jet (*cf.* figures 9a-c, 10a-c, and 11a-c), where lower velocities, increased viscous effects, and higher sensitivity to the flow Reynolds number can be expected.

2.4 Isoscalar bounding-box size

The extent of the scalar isosurfaces (*cf.* figures 9a-c, 10a-c, and 11a-c) allows the local, mixed-fluid extent to be estimated. This can be computed by identifying the bounding box that encloses each isosurface, in general, or the smallest circumscribing rectangle (*cf.* Tricot 1995), in two dimensions. Figure 13 depicts such a bounding box, identified for the isosurface in figure 10a, as well as the extent of the field-of-view. Note that, while this rectangle is oriented along the field-of-view axes, the near-circular symmetry of the individual two-dimensional scalar power spectra (*cf.* figure 6), as well as the ensemble-averaging over separate realizations, renders

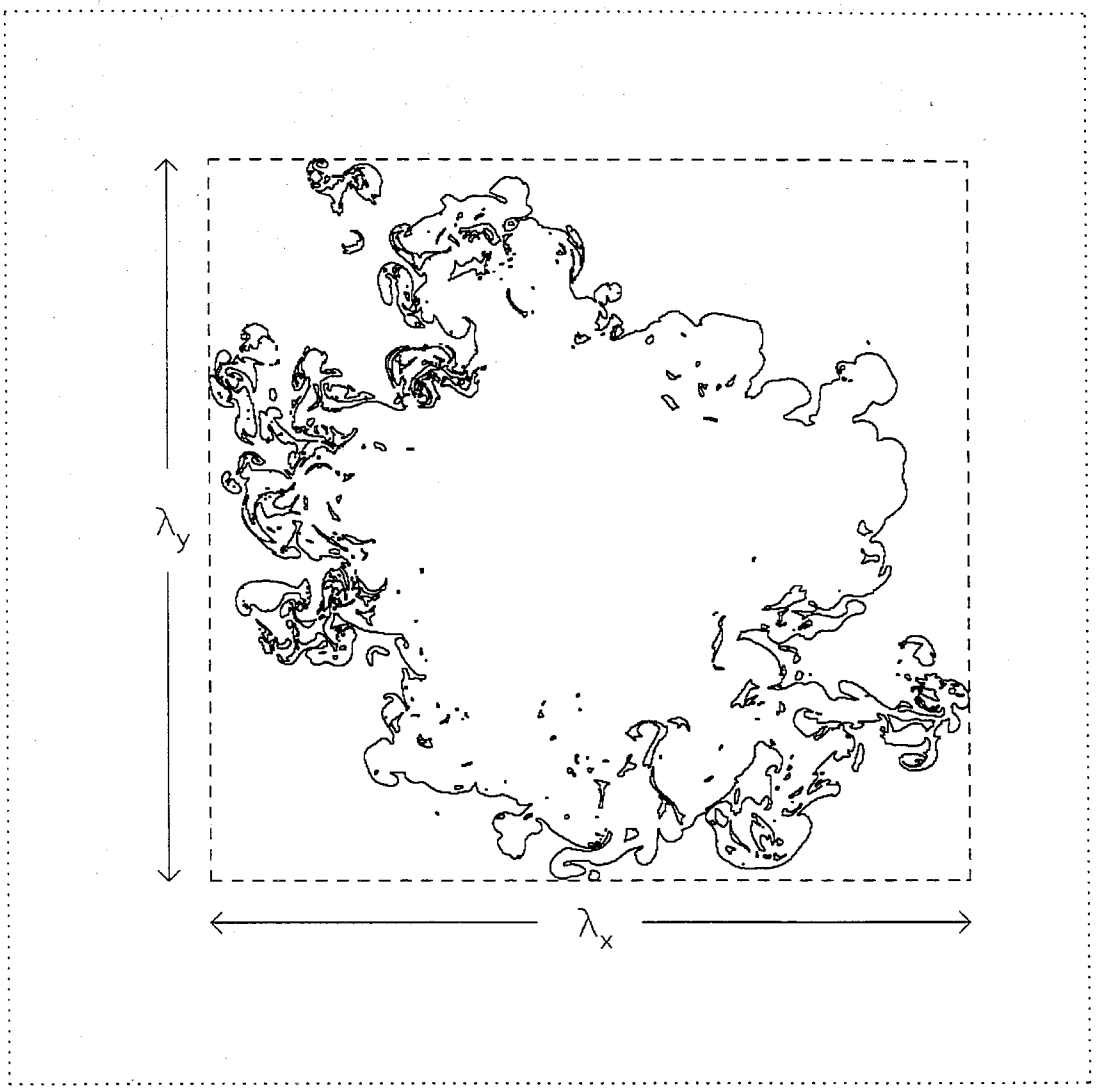

FIGURE 13 Bounding box (dashed line) for the level set of figure 10a. Dotted line: field-of-view boundaries.

it a useful measure. The isoscalar spatial extent, $\delta_{\rm b}$, was computed as the square root of the area of the rectangle (bounding box), *i.e.*,

$$\delta_{\rm b} \equiv (\lambda_x \lambda_y)^{1/2} \quad , \tag{2.2}$$

where λ_x and λ_y are the lengths of the two sides of the circumscribing rectangle; *cf.* equation (A.1) and related discussion.

Figure 14 shows the ensemble-averaged spatial extent scaled by the distance

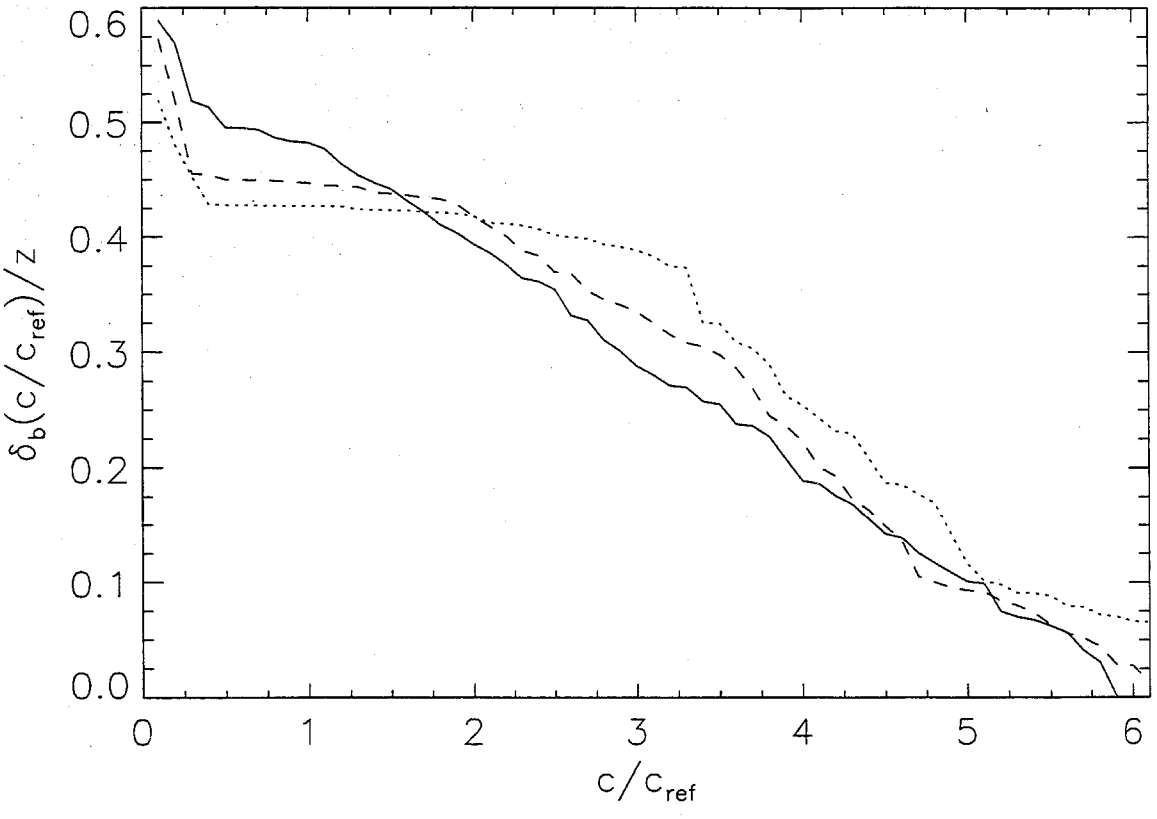

FIGURE 14 Isoscalar spatial extent, δ_b, based on bounding box, as a function of scalar threshold and Reynolds number. $Re \simeq 4.5 \times 10^3$: dotted line; $Re \simeq 9.0 \times 10^3$: dashed line; $Re \simeq 18 \times 10^3$: solid line.

downstream, δ_b/z, as a function of scalar threshold and Reynolds number. Alternatively, $\delta_b/2$ is a measure of the maximum distance from the jet axis where a particular scalar value will be encountered. As expected, the isoscalar spatial extent, δ_b, decreases monotonically with increasing scalar threshold, at a given Reynolds number. As with the scalar pdf's and the area measure, a qualitative change in the dependence of δ_b on the scalar value, c/c_{ref}, can be seen as the Reynolds number is increased from 4.5×10^3 to 18×10^3. The spatial extent of the outer isosurfaces increases with increasing Reynolds number, while the extent of the inner isosurfaces decreases with increasing Reynolds number. In addition, the variation of δ_b with c/c_{ref} appears to approach a straight line as the Reynolds number is increased (*cf.* figure 14), *i.e.*,

$$\frac{\delta_b}{z} \longrightarrow \alpha - \beta \frac{c}{c_0} , \tag{2.3}$$

with $\alpha \simeq 0.6$ and $\beta \simeq 0.1\, c_0/c_{\rm ref} \simeq 22$; *cf.* equation (1.2). This behavior, in addition to the changes in the nature of the scalar pdf's and area enclosed by the level sets noted above, provides further evidence of a mixing transition in this range of Reynolds numbers.

At the intermediate scalar threshold, c_2, corresponding to the peak of the pre-transition pdf's, the isoscalar spatial extent, $\delta_{\rm b}$, is seen to be (approximately) Reynolds-number independent (figure 14), at least for the Reynolds numbers investigated. This feature will be exploited in the analysis of Reynolds-number effects on the geometry of the isoscalar surfaces, *i.e.*, comparisons of geometric measures, at different Reynolds numbers, will be made at this intermediate threshold.

2.5 Isosurface spacing

As noted in section 2.1 (Eq. 3.1 and related discussion), the scalar pdf, $p(c)$, is equivalent to the area enclosed by the isoscalar surfaces (contours), $A(c)$, *i.e.*,

$$p(c) = \frac{1}{A_0} \frac{|{\rm d}A(c)|}{{\rm d}c} \ . \tag{2.4}$$

This can be related to the mean isosurface spacing (per unit c), $h(c)$, in terms of the (total) isoscalar arc-length*, $L(c)$, and an integral of the inverse of the (2-D) scalar gradient, $\nabla_2(c)$, along the isoscalar contours, Γ_c, *i.e.*,

$$h(c) \equiv \left\langle \left| \frac{\partial c}{\partial n} \right|^{-1} \right\rangle_c = \frac{1}{L(c)} \int_{\Gamma_c} \left| \frac{\partial c}{\partial n} \right|^{-1} {\rm d}s_c = \frac{1}{L(c)} \frac{|{\rm d}A(c)|}{{\rm d}c} \ , \tag{2.5}$$

(*e.g.*, Kuznetsov and Sabel'nikov 1990, p. 27). In view of equations (2.4) and (2.5), the mean isosurface spacing (per unit c) can be written as,

$$h(c) = \frac{p(c)}{L(c)/A_0} \ , \tag{2.6}$$

---

* The arc-length was computed using a biquadratic B-spline representation of the isoscalar contours; see Appendix C.

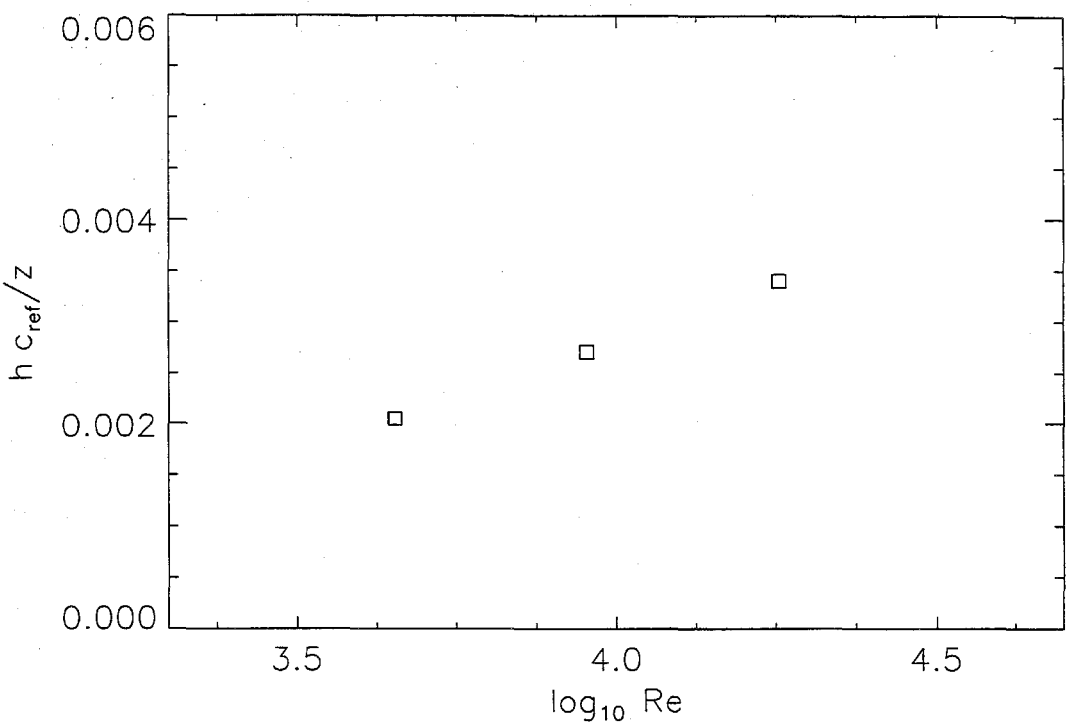

FIGURE 15 Reynolds-number dependence of isosurface spacing (per unit c), $h(c; Re)$, at the intermediate scalar threshold, c_2.

and can be identified, therefore, as the ratio of the scalar-pdf value to the perimeter-to-area ratio of the isoscalar contours.

The Reynolds number dependence of $h(c; Re)$, at the intermediate scalar threshold, c_2, is depicted in figure 15. The data indicate that the isosurface spacing increases with increasing Reynolds number, at the c_2 threshold, in the Reynolds number range investigated. This indicates a higher degree of (local) scalar-field homogenization (molecular mixing) with increasing Reynolds number, at this threshold. This behavior will be further investigated using fractal-geometric measures of the isosurfaces; *cf.* chapter 5.

CHAPTER 3

Scale-dependent-fractal geometry

In this chapter, various fractal measures of complex surfaces (*e.g.*, isosurfaces in turbulence or turbulent mixing) are considered. In particular, a generalization of (power-law) fractal (PLF) geometry is described that extends the notion of the (PLF, constant) fractal dimension to that of a scale-dependent-fractal (SDF) dimension. The resulting SDF framework can accommodate more complex geometries and can be used to model (in terms of, for example, stochastic-geometric simulations) multiscale structures whose complexity, as measured by the fractal dimension, for example, can be scale-dependent.

After a brief summary of PLF geometry and a critical review of reports and proposals of PLF scaling in turbulence, as well as some reports and conjectures of (what would be termed here) SDF scaling in a variety of phenomena exhibiting natural complexity, the framework of SDF geometry is described. A comparison of SDF properties to the more-restrictive PLF properties is made. Various measures related to SDF coverage statistics are considered: the SDF dimension, the coverage fraction, and the coverage length (for curves). The implications of SDF behavior regarding the resulting nonlinear and nonlocal geometric-scaling behavior are addressed.

3.1 Review of power-law-fractal (PLF) geometry

Characterizations of the geometry of isosurfaces in turbulence, in particular, and of other complex structures encountered in natural phenomena, in general, require extending notions of Euclidean geometry. One such extension was proposed by Mandelbrot (1967, 1975b, 1977, 1982) who suggested that fractional (non-integer) dimensions can be used to describe complex geometries in nature. The word *fractal* was coined by Mandelbrot (1975a,b) to denote geometric objects that exhibit power-law scaling, *i.e.*, objects characterized by constant, fractional (in general) dimensions. He regarded such objects as, "... rough and fragmented to the same degree at all scales" (Mandelbrot 1989). In the following, the original (power-law scaling) fractal geometry will be denoted as PLF (power-law-fractal). As originally defined by Mandelbrot, a "power-law" fractal would be a redundant term. The present terminology is used to distinguish it from more general, scale-dependent-fractal (SDF) behavior that is encountered with the scalar isosurfaces in the present experiments, as well as with other complex geometries, as discussed below. PLF geometry has been applied to the description of a wide variety of natural phenomena (*e.g.*, Mandelbrot 1982). In these descriptions, PLFs are used to characterize the geometry in a finite range of scales that is bounded by upper- and lower-cutoff scales, "a property we can assume for all objects arising as a result of any physical process" (Vicsek 1992). The underlying point of view, in such descriptions of natural objects as PLFs, is that, "... over certain ranges of scale they appear very much like [power-law] fractals and at such scales may usefully be regarded as such." (Falconer 1990, p. xxi) — square-bracket insert mine. Fluid turbulence, a phenomenon long recognized to possess complex structure, was considered by Mandelbrot (1975a,b) as a candidate for PLF geometry.

Ever since Richardson's (1961) analysis of data on the length of coastlines and borders between countries and Mandelbrot's (1967) subsequent interpretation and proposals, it has become appreciated that convoluted curves and surfaces can be regarded as possessing scale-dependent length and area, respectively, that increase as the measurement resolution is extended to smaller and smaller scales. This is a consequence of the presence of ever-finer features that are encountered as the scale of measurement is reduced, in many phenomena. One particular form of

this scale dependence is a power-law function. The resulting fractal, or power-law-fractal (PLF), geometry has been proposed as an appropriate framework for the characterization of various complex structures in nature (*e.g.*, Mandelbrot 1967, 1975b, 1977, 1982).

PLF curves in a plane, for example, have a coverage-length, $L_2(\lambda)$, that increases in a power-law manner with decreasing scale, λ, *i.e.* (*cf.* Richardson 1961),

$$L_2(\lambda) \propto \lambda^{1-D_2} \tag{3.1}$$

(with a dimensional prefactor), where $1 < D_2 \leq 2$ is the PLF dimension. The subscript 2, here, denotes the two-dimensional embedding (Euclidean) space of these curves. The coverage-length, $L_2(\lambda)$, is defined in terms of the (box) coverage, $N_2(\lambda)$, which is the number of (nonoverlapping, Euclidean) tiles (2-D boxes) of size λ needed to cover the curve, *i.e.*,

$$L_2(\lambda) \equiv \lambda N_2(\lambda) \ , \tag{3.2}$$

where, for PLF curves, the coverage follows a power-law,

$$N_2(\lambda) \propto \lambda^{-D_2} \ , \tag{3.3}$$

also, presumably, with a dimensional prefactor and a scaling exponent given by the (negative of the) constant, PLF dimension, D_2.

In a d-dimensional embedding space, PLF sets are characterized by a geometric coverage, $N_d(\lambda)$, given by the number of (nonoverlapping, Euclidean) boxes (tiles, in 2-D), of size λ, needed to cover the set, that follows a power-law, *i.e.*,

$$N_d(\lambda) \propto \lambda^{-D_d} \ , \tag{3.4}$$

also with a dimensional prefactor, where $d_t < D_d \leq d$ is the PLF dimension, and d_t is the (integer-valued) topological dimension of the set. PLF relations, such as equations (3.1), (3.3), and (3.4), describe scale-independent geometric-scaling laws. From such power-law relations, the PLF dimension is identified as the scaling exponent of the coverage, *i.e.*,

$$D_d = -\frac{\mathrm{d}\log N_d(\lambda)}{\mathrm{d}\log\lambda} \ , \tag{3.5}$$

in a range of scales (only logarithms of dimensionless scales are allowed; for notational simplicity, the (constant) normalizing length will be omitted sometimes). This PLF dimension can be expected to be constant if, and only if, the coverage, $N_d(\lambda)$, follows an exact power-law, *i.e.*, only for geometric structures possessing scale self-similarity.

Mandelbrot (1975a) had pointed out that, "turbulent shapes... almost cry out for proper geometrical description" and proposed that PLF geometry may be applicable to turbulence (Mandelbrot 1975a,b) suggesting a PLF dimension of $D_3 = 8/3$ for isoscalar surfaces in homogeneous turbulence with Kolmogorov-Gauss scaling (obtained by analyzing random, Gaussian fields with Kolmogorov variance). Welander (1955) had also proposed PLF geometry as a model for the geometry of interfaces advected in turbulence. In the last ten years, or so, the geometry of isosurfaces in turbulence has been the object of various experimental, numerical, as well as theoretical studies. Several investigators have reported PLF behavior in the geometry of turbulence. Sreenivasan & Meneveau (1986) reported experimental findings of PLF dimensions, $D_1 = 0.32$ and $D_2 = 1.33$, for isoscalar measurements in a turbulent jet, from which they argued that $D_3 = 2.33$ for the (three-dimensional) isoscalar surfaces. Sreenivasan, Prasad, Meneveau, & Ramshankar (1989) found a PLF dimension of $D_2 = 1.36$ for isoscalar jet data, with $D_2 = 1.35 \pm 0.05$ as a mean value for various turbulent shear flows, and offered arguments for a value of $D_3 = 7/3$ based on Reynolds number similarity. Prasad & Sreenivasan (1990) analyzed three-dimensional data of the isoscalar surfaces in turbulent jets and reported a PLF dimension of $D_3 = 2.35 \pm 0.04$. A theoretical estimate for a PLF dimension of $D_3 = 2.5$ was obtained by Constantin (1989, 1990a), later refined to $D_3 = 8/3$ (Constantin, Procaccia, & Sreenivasan 1991; Constantin 1994a,b; and Constantin & Procaccia 1994), based on isosurface-area bounds obtained from the scalar advection-diffusion equation with Kolmogorov scaling for the advecting velocity field (as well as the assumption that such a PLF, constant dimension exists).

A lack of PLF scaling had been noted, however, by Sreenivasan (1991, p. 553) for isoscalar surfaces in the interior of the jet. In contrast, Constantin, Procaccia, & Sreenivasan (1991), reported PLF scaling in the jet interior, with $D_3 = 2.67$, citing the same isosurface for which Sreenivasan (1991, p. 553) had originally concluded

that there was no PLF scaling. In particular, Constantin, Procaccia & Sreenivasan (1991) suggested PLF dimensions of $D_3 = 8/3$, for isoscalar surfaces in the jet interior, and $D_3 = 7/3$, for isoscalar surfaces near the jet boundary. Procaccia, Brandenburg, Jensen, & Vincent (1992) pointed out, however, that "the theory [of Constantin *et al.* (1991)] cannot exclude the possibility that the scaling exponent D depends on [the scale] r" (inserts in square brackets mine). Procaccia *et al.* (1992) analyzed isosurfaces of vorticity in three-dimensional homogeneous turbulence, using the direct-numerical-simulation data of Vincent & Meneguzzi (1991), and concluded that, "... it is impossible to state with confidence that the [PLF] behavior [of the vorticity isosurfaces] is clear-cut." Lane-Serff (1993) reported a threshold-dependent PLF dimension of isoscalar surfaces in liquid-phase jet and plume flows, with a minimum value of $D_2 = 1.23$, computed by fitting a straight line using a least-squares fit. He noted, however, that "there is a distinct curve [*i.e.*, curvature, in the coverage plots]" but attributed this to "the small range between integral and Kolmogorov scales at the Reynolds numbers of [the] experiments". Flohr & Olivari (1994) analyzed isoscalar surfaces in gas-phase turbulent jets and reported "constant [PLF] scaling behavior over a wide range [of scales]" with a threshold-dependent PLF dimension exhibiting a maximum value. For the outer isoscalar surfaces, they suggested a PLF dimension of $D_2 = 1.30 \pm 0.05$. Sreenivasan (1994) suggested a PLF dimension of $D_3 = 2.35 \pm 0.05$ for outer isoscalar surfaces in turbulent jets, with PLF scaling "over much of the interval between the integral scale and the Kolmogorov scale," and a PLF dimension of $D_3 = 2.67 \pm 0.05$ for inner isoscalar surfaces in turbulent jets, in a scaling range "smaller" than that for the outer isosurfaces, indicating the degree of confidence of his results as "fairly certain".

Takayasu (1982) had argued, however, that the dynamics of turbulent flow vary with scale, and had suggested that, as a consequence, descriptions of the geometry of turbulence may be expected to require fractal dimensions that are functions of scale and not constant. To support his conjecture, Takayasu invoked Reynolds number similarity. Interestingly, the same principle was invoked by Sreenivasan *et al.* (1989) to argue for PLF behavior and a constant, fractal dimension. Takayasu characterized the geometry of the path of a one-dimensional random-walk particle with finite mean-free-path, using a scale-dependent fractal (SDF) dimension, and conjec-

tured the applicability of SDF dimensions to turbulent diffusion. In random walks with finite mean-free-path, particles perform correlated, or inertial, random walks when observed at scales larger or smaller than the mean-free-path scale (Takayasu 1982). As a model of turbulent diffusion, Taylor (1921) had considered a modified random walk in which he allowed for particles with inertia, *i.e.*, a random walk with correlated steps. Taylor's modification of the random walk illustrated the nature of turbulent diffusion as a correlated random walk (*cf.* McComb 1991). Borgas (1993) has offered Lagrangian-statistic arguments for a SDF dimension of particle trajectories in turbulent flow.

Miller & Dimotakis (1991a) reported on experiments in the far field of liquid-phase turbulent jets, in which no PLF behavior was found for scalar level sets derived from either point, line, or space-time (streak-image) measurements of the jet-fluid-concentration field, at least for thresholds in the vicinity of the mean of the scalar pdf. In particular, they found a SDF dimension, $D_1(\lambda)$, for scalar level sets derived from one-dimensional temporal and spatial data, with a smooth variation from 0, at the smallest scales, to 1, at the largest scales. They also reported values of $D_{1+1}(\lambda)$, increasing continuously with scale, from near 1 to almost 2, for isoscalar contours derived from space-time data (one space dimension plus time), in the neighborhood of the axis of turbulent jets. Sreenivasan (1991) commented on the Miller & Dimotakis (1991a) findings, suggesting they could be attributable to differences between temporal and spatial data. See also Kerstein (1991) for an alternate discussion. Dimotakis (1991) argued, generally, that for scales λ that are dimensional, as is the case here, there are dimensional and similarity issues that arise with expressions like equation (3.4) and that, in particular, characteristic scales are necessary for PLF scaling, in contrast with previous proposals. Gluckman, Willaime, & Gollub (1993) conducted experiments in thermal turbulence and found that thermal isosurfaces do not display PLF scaling, while scalar isosurfaces show a limited range of "approximately-[power-law-]fractal" scaling.

3.2 Scale-dependent-fractal (SDF) geometry

A scale-dependent-fractal (SDF) set may be regarded as a geometric object characterized by a fractal dimension that is a function of the scale λ, *i.e.*, $D_d(\lambda)$, in a range of scales. The subscript, d, denotes the embedding (Euclidean) dimension for the object. SDF sets obey general geometric-scaling laws and allow for more complex geometric structures than PLF sets, which are, by definition, restricted to scale-invariant complexity. The difference between a PLF dimension, D_d, and a SDF dimension, $D_d(\lambda)$, can be illuminated by considering a hierarchy of complex patterns (*cf.* Mikhailov & Loskutov 1991):

- Level 1: Classical Euclidean patterns (*e.g.*, circle)
- Level 2: Scale-invariant complexity (PLFs)
- Level 3: Scale-dependent complexity (SDFs)

At the lowest level of complexity (level 1), simple Euclidean objects, such as circles, spheres, have structure only at a certain (large) scale and are associated with the integer-valued embedding dimension, d. A higher level of complexity (level 2) is possible for objects for which structure persists at all scales; these objects are PLFs. Level 2 objects are associated with a PLF dimension, D_d. For PLFs, it is the *same structure* that persists at various scales. A higher level yet (level 3) can occur for objects that have structures of variable complexity at different scales; this is the level of SDFs. Level 3 objects are characterized by a SDF dimension, $D_d(\lambda)$. SDFs can be seen, therefore, as scale-dependent generalizations of PLFs.

Various phenomena with natural complexity have been reported to exhibit SDF behavior. Different investigators have employed terminologies to denote $D_d(\lambda)$. Some have also suggested models for the observed SDF behavior. As noted above, Takayasu (1982) found SDF behavior in characterizing the geometry of the path of random-walk particles. Using a real-space renormalization argument, he derived an expression for the successive coverage of a one-dimensional random walk with finite mean-free path. Takayasu initially used the term "differential fractal dimension," later employing the term "scale-dependent fractal dimension" (Takayasu 1992). Suzuki (1984) reported SDF behavior for Japanese coastlines and suggested a SDF Koch curve model. Suzuki used the term "transient fractal dimension" and

"transient fractals" to describe SDF properties. Mark & Aronson (1984) reported SDF behavior in the analysis of topographic surfaces and used the term "scale-dependent fractal dimension." Chilés (1988) studied fractured rocks and reported a continuously-varying "local similarity dimension" as a function of scale. Chilés suggested several models for SDF behavior, including SDF Cantor dust. A smooth variation of the coverage dimension with scale was found by Miller & Dimotakis (1991a) in their analysis of turbulent-jet scalar data, as noted above. In characterizing the distribution of galaxies in the universe, Castagnoli & Provenzale (1991) suggested that "... it is probably necessary to consider models whose scaling and fractal properties vary with the spatial scale." In addition, Brandt *et al.* (1991), in their analysis of solar granulation data, found "... a smooth transition of the fractal dimension from small to large granules." Rigaut (1991) studied surfaces of biological tissues, using microscopic biometry, and also reported SDF behavior. In an analysis of the alveolar geometry of lungs of prematurely-born rabbits, he reported a "drifting fractal dimension" with scale and used the term "semi-fractals" for SDFs. The term "scale-dependent fractal dimension", employed by Mark & Aronson (1984) and Takayasu (1992), has been adopted here.

It is appropriate, in my opinion, to call the resulting objects "scale-dependent fractals" (SDFs), since the word "fractal", coined by Mandelbrot (1975a,b) from the Latin *fractus*, means "fragmented", as he notes (Mandelbrot 1982, p. 4), and need not be excluded from referring to scale-dependent (fragmented) behavior.

3.3 Box coverage

Consider a set, $\mathcal{S}$, embedded in a d-dimensional space, E_d, and contained in a d-dimensional bounding box of size δ_b. Consider, also, successive partitions of the δ_b-box into non-overlapping, λ-size interior boxes that fill the δ_b-box volume (*cf.* Appendix for the two-dimensional implementation adopted here). The geometric (box) coverage, $N_d(\lambda)$, of the set, $\mathcal{S}$, is defined as the minimum number of nonoverlapping partition λ-boxes needed to cover the set. It follows that,

$$\mathcal{S} \subset \bigcup_{i=1}^{N_d(\lambda)} B_d^{(i)}(\lambda) \ , \tag{3.6}$$

where $B_d(\lambda)$ denotes a d-dimensional box, interior to the bounding box, of size λ, *i.e.*, of volume λ^d, with $B_d^{(i)}(\lambda) \cap B_d^{(j)}(\lambda) = \emptyset$, for $i \neq j$. The d-dimensional volume (area in 2-D) of the portion of space visited by the set, at the coverage scale λ, is, therefore, $\lambda^d N_d(\lambda)$.

The notions of coverage measure, and capacity dimension, introduced by Hausdorff (1919) and Kolmogorov and Tihomirov (1959), were defined in the limit of $\lambda \to 0$. Equation (3.6), however, allows the study of coverage statistics at any (finite) coverage scale, λ. In particular, the specification of nonoverlapping partition boxes, in equation (3.6), permits the coverage *fraction* to be identified as a geometric probability, which can, in turn, be connected to a distribution of geometric scales of the set, as will be discussed below.

The size of the bounding box, δ_b, provides a useful measure of the largest scale exhibited by the set. At this scale, the coverage count is unity (by construction), *i.e.*,

$$N_d(\delta_b) = 1 \ . \tag{3.7}$$

For the level sets considered above, for example, for which the bounding box is the two-dimensional ($d = 2$) circumscribing rectangle, δ_b is given by the square-root of the area of the two-dimensional circumscribing rectangle; *cf.* (2.2). At all scales, the coverage count defined above has the property that,

$$\frac{\mathrm{d}N_d(\lambda)}{\mathrm{d}\lambda} \leq 0 \ , \tag{3.8}$$

i.e., at any scale smaller than the bounding-box scale, the coverage count will decrease (or remain constant) with decreasing scale (*cf.* Miller & Dimotakis 1991a, Appendix).

3.4 Definition and properties of SDF dimension

The SDF (box) dimension is the scale-dependent generalization of the PLF dimension. It can be defined (*e.g.*, Takayasu 1982, 1992, Miller & Dimotakis 1991a, Dimotakis 1991), at a coverage scale λ, as,

$$D_d(\lambda) \equiv -\frac{\mathrm{d}\log N_d(\lambda)}{\mathrm{d}\log\lambda} \ , \tag{3.9}$$

in terms of the geometric coverage, $N_d(\lambda)$; *cf.* (3.6). The geometry of an object will be SDF if, in a range of scales,

$$\frac{\mathrm{d}D_d(\lambda)}{\mathrm{d}\lambda} \neq 0 \ , \tag{3.10}$$

while it will be PLF (*i.e.*, $D_d = \text{const.}$) if,

$$\frac{\mathrm{d}D_d(\lambda)}{\mathrm{d}\lambda} = 0 \ . \tag{3.11}$$

SDF dimensions, defined through equations (3.9) and (3.10), allow for the description of phenomena whose geometric-scaling laws are scale-dependent, as can be expected to be admissible in general.

The SDF dimension, $D_d(\lambda)$, can be expected to tend to the topological dimension, d_t, at the smallest scales, and to the embedding dimension, d, at the largest scales, *i.e.*,

$$D_d(\lambda) \longrightarrow \begin{cases} d_\mathrm{t}, & \text{as} \quad \lambda \rightarrow 0; \\ d, & \text{as} \quad \lambda \rightarrow \delta, \end{cases} \tag{3.12}$$

where δ is the largest characteristic scale of the set (*cf.* Dimotakis 1991). For spatial data confined in a bounding box, the SDF dimension will approach the embedding dimension at the scale $\delta = \delta_\mathrm{b}$ (the bounding-box size).

If $D_d(\lambda)$ is monotonic with scale, the limiting values in equation (3.12) will also be the bounding values. Non-monotonicity of the SDF dimension (in a range of scales) is possible, however, for cluster-like structures (for example). Scale-local clustering can lead to values of the SDF dimension that are below the topological dimension, in a range of scales.

The SDF geometric-coverage law that follows from equation (3.9) is given, in differential form, by

$$\frac{\mathrm{d}N_d(\lambda)}{N_d(\lambda)} \;=\; -\,D_d(\lambda)\,\frac{\mathrm{d}\lambda}{\lambda}\;, \tag{3.13}$$

i.e., the SDF dimension of a set, at a scale λ, can be identified as the fractional decrease in coverage, $-\,\mathrm{d}N_d/N_d$, per unit fractional increase in scale, $\mathrm{d}\lambda/\lambda$. Note that, if $D_d(\lambda) \neq$ const., the SDF differential-coverage relation (3.13) does *not* imply a power-law-like coverage, *i.e.*, $N_d(\lambda) \not\propto \lambda^{-D_d(\lambda)}$; *cf.* (3.4).

Integrating the differential coverage relation (3.13), from a reference scale, λ_1, to a scale, λ, we see that a SDF dimension implies a geometric-scaling coverage law given by (*cf.* Takayasu 1982, 1992)

$$\frac{N_d(\lambda)}{N_d(\lambda_1)} \;=\; \exp\left\{\,-\int_{\lambda_1}^{\lambda} D_d(\lambda')\,\frac{\mathrm{d}\lambda'}{\lambda'}\,\right\} \;=\; \exp\left\{\,\int_{\lambda}^{\lambda_1} D_d(\lambda')\,\frac{\mathrm{d}\lambda'}{\lambda'}\,\right\}\;. \tag{3.14}$$

In particular, if the largest scale of the set, δ_{b}, is the reference scale, we have,

$$N_d(\lambda) \;=\; \exp\left\{\,\int_{\lambda}^{\delta_{\mathrm{b}}} D_d(\lambda')\,\frac{\mathrm{d}\lambda'}{\lambda'}\,\right\}\;, \tag{3.15}$$

since $N_d(\delta_{\mathrm{b}}) = 1$; *cf.* (3.7). Equation (3.15) should be contrasted with the scale-local relation (3.4) for PLFs. For SDFs, the coverage can be seen to be a nonlocal function of scale, with geometric structure across the whole range of scales potentially contributing to the coverage at any one scale.

For the isoscalar contours considered above, the SDF coverage can be written, therefore, as,

$$N_2(\lambda) \;=\; \exp\left\{\,\int_{\lambda}^{\delta_{\mathrm{b}}} D_2(\lambda')\,\frac{\mathrm{d}\lambda'}{\lambda'}\,\right\}\;, \tag{3.16}$$

where, for the two-dimensional space here, $\delta_{\mathrm{b}} = \sqrt{\lambda_x \lambda_y}$ is the size of the bounding box, with λ_x and λ_y the lengths of the two circumscribing-rectangle sides; *cf.* (2.2).

3.5 Coverage length

A useful measure, related to the coverage, is the (scale-dependent) d_t-dimensional size of the set, defined as,

$$\mathcal{V}_d(\lambda) \equiv \lambda^{d_t} N_d(\lambda) \ , \tag{3.17}$$

where d_t denotes the topological dimension of the set. In particular, for the level sets considered above ($d_t = d - 1 = 1$), this quantity, with the units of length, becomes the coverage-length (distinct from arc-length, due to the box nature of the coverage process) of the isoscalar contours, $L_2(\lambda)$, *cf.* (3.2), and can be computed from,

$$\frac{L_2(\lambda)}{\delta_b} \equiv \frac{\lambda}{\delta_b} N_2(\lambda) \ , \tag{3.18}$$

where the coverage-length is scaled by the size of the bounding-box, δ_b.

The coverage-length, at a scale λ, is, therefore, given by,

$$\frac{L_2(\lambda)}{\delta_b} = \frac{\lambda}{\delta_b} \exp\left\{ \int_{\lambda}^{\delta_b} D_2(\lambda') \frac{\mathrm{d}\lambda'}{\lambda'} \right\} \ . \tag{3.19}$$

Note, again, the nonlinear and nonlocal scaling as compared to PLF behavior; *cf.* equation (3.1).

The small-scale limit of the coverage-length, *i.e.*,

$$\frac{L_2(\lambda \to 0)}{\delta_b} = \lim_{\lambda \to 0} \left[\frac{\lambda}{\delta_b} N_2(\lambda) \right] \ , \tag{3.20}$$

provides a finite (dimensionless) measure, at the smallest scales, for one-dimensional ($d_t = 1$) level sets embedded in a two-dimensional space ($d = 2$), such as the isoscalar (level) sets considered above. In particular, it is a dimensionless measure of the surface-to-volume ratio (perimeter-to-area ratio, in 2-D) of the isosurfaces, in terms of the isoscalar bounding-box area, δ_b^2, *i.e.*, $L_2(\lambda \to 0)/\left(\delta_b^2\right)^{1/2}$.

3.6 Coverage fraction

Another useful measure based on the coverage is the coverage fraction, $F_d(\lambda)$, or volume-fill fraction, of the set at a scale λ, defined as (*cf.* Dimotakis 1991),

$$F_d(\lambda) \equiv \frac{N_d(\lambda)}{N_{d,\mathrm{tot}}} = \left(\frac{\lambda}{\delta_\mathrm{b}}\right)^d N_d(\lambda) \ , \tag{3.21}$$

where $N_{d,\mathrm{tot}}$ is the total number of d-dimensional boxes of size λ that can fit in the bounding box. It can be identified as the geometric probability that a randomly placed λ-box, interior to the bounding box, contains part of the set.

For level sets derived from two-dimensional data ($d = 2$), the coverage fraction can be computed from,

$$F_2(\lambda) \equiv \left(\frac{\lambda}{\delta_\mathrm{b}}\right)^2 N_2(\lambda) \ ; \tag{3.22}$$

cf. (3.18).

The coverage fraction, as opposed to the SDF dimension, must be a nondecreasing function of scale, *cf.* (3.10), *i.e.*,

$$\frac{\mathrm{d}F_d(\lambda)}{\mathrm{d}\lambda} \geq 0 \ , \tag{3.23}$$

at all scales.

The logarithmic derivative of $F_d(\lambda)$ follows from equations (3.21) and (3.9), *i.e.*,

$$\frac{\mathrm{d}\log F_d(\lambda)}{\mathrm{d}\log\lambda} = d - D_d(\lambda) \ , \tag{3.24}$$

so that the behavior of the coverage fraction is characterized by the embedding-dimension-complement of the SDF dimension.

The limiting behavior of the coverage fraction is, *cf.* (3.12),

$$F_d(\lambda) \sim \lambda^{d-d_\mathrm{t}} \ , \qquad \text{as} \qquad \lambda \to 0 \ , \tag{3.25a}$$

and

$$F_d(\lambda) \to 1 \ , \qquad \text{as} \qquad \lambda \to \delta_\mathrm{b} \ . \tag{3.25b}$$

Integrating equation (3.24) from a coverage scale, λ, to the largest scale, δ_b, the SDF relation for the coverage fraction becomes, *cf.* (3.14),

$$F_d(\lambda) \;=\; \exp\left\{ -\int_{\lambda}^{\delta_b} \Big[d \;-\; D_d(\lambda') \Big] \frac{\mathrm{d}\lambda'}{\lambda'} \right\} \;, \tag{3.26}$$

since $F_d(\delta_b) = 1$; *cf.* (3.25b). The degree to which a SDF set fills space, therefore, varies with scale and is dependent on the geometric behavior at other scales.

3.7 Nonlinear and nonlocal geometric scaling

The implications of SDF geometry, as illustrated in equations (3.14), (3.19), and (3.26), are that geometric structures across a wide range of scales can contribute to the scaling behavior at any one scale, λ. This is manifested, for example, in the coverage, coverage-length, or volume-fill fraction. For these measures, the scaling becomes nonlinear (in logarithmic coordinates).

In SDF geometry, the SDF dimension, $D_d(\lambda)$, is no longer a scaling exponent; recall the discussion of equation (3.13). It does, however, quantify the departure of the set from the topological dimension at a given scale, and indicates the type of structure (or, more precisely, the complexity of structure type) present at any one scale. By definition, it measures the (fractional) rate of increase of the coverage with descreasing scale (inreasing resolution); *cf.* equation (3.13).

SDF geometry provides the means to model nonlinear and nonlocal geometric scaling, in terms of simulations based on models of scale distributions (see next chapter). From the above considerations, it is concluded that SDF geometry provides a more inclusive framework than PLF geometry that can be used to the natural complexity exhibited by multiscale phenomena, in general, and by turbulence, in particular.

CHAPTER 4

Scale distribution

Many phenomena in nature are characterized by complex geometries, possessing a wide range of coexisting spatial and/or temporal scales that participate in the dynamics, *e.g.*, turbulent flow, or biological organisms and many others (see, for example, Mandelbrot 1982, Nonnenmacher *et al.* 1994). Measures that are employed to characterize the geometry of such phenomena can also be useful for the computation of quantities of practical interest, *e.g.*, fractal dimensions of isoscalar surfaces in turbulent mixing to estimate the volume-fill fraction, or surface-to-volume ratio of cell boundaries that limits the fluid flux for a given osmotic gradient (*e.g.*, Welling *et al.* 1996).

In this chapter, a geometric framework is presented that connects the scale-dependent-fractal (SDF) dimension (Catrakis & Dimotakis 1996a,b) to the distribution of measures of (spatial or temporal) scales. A 1-D formalism for stochastic point sets is derived and demonstrated on several distributions of spacing scales. Statistically homogeneous velocity, or species-concentration, threshold crossings (level sets), arising in turbulence would constitute such 1-D point sets, for example. Similarly, level sets of 1-D cuts through 2-D geometries consisting of lines, or 3-D geometries consisting of surfaces, would also constitute such point sets. An extension of this theory to higher dimensions is also developed, in terms of a measure of scale appropriate for multidimensional geometries.

4.1 1-D theory: spacing scales

To investigate 1-D, multiscale, geometries first, consider a stochastic, statistically homogeneous, point process on the real line, *e.g.*, space or time, with a distribution of spacing scales, *i.e.*, interval-lengths between successive events of the process, described by a probability density function (pdf), $p_1(l)$, where l denotes a (nonnegative) spacing scale, *cf.* figure 16. The fraction of length spanned by a l-scale will be $m_1(l) \propto l\,p_1(l)$. The probability (density) that a random location, with uniform measure on the real line, lies in a l-spacing is, therefore,

$$m_1(l) = \frac{l\,p_1(l)}{l_{\rm m}} , \quad \text{where,} \quad l_{\rm m} \equiv \int_0^\infty l p_1(l) \mathrm{d}l , \tag{4.1}$$

cf. figure 16.

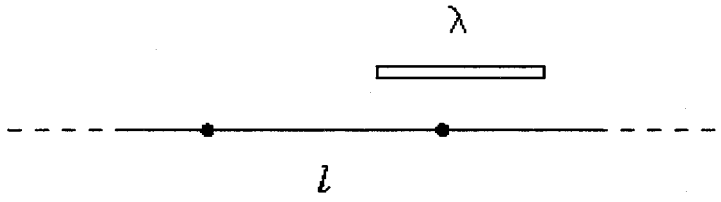

FIGURE 16 Spacing scale, l, and coverage scale (tile size), λ, for a stochastic point process (indicated by filled circles) on the real line.

The geometric probability that a λ-tile, randomly located on the real line (with uniform measure), is "empty", *i.e.*, contains no transitions (points), can be written as,

$$\tilde{p}_1^{\rm E}(\lambda) = \int_0^\infty p_1^{\rm E}(\lambda \mid l)\, m_1(l)\, \mathrm{d}l . \tag{4.2}$$

In this expression, $p_1^{\rm E}(\lambda \mid l)$, the conditional probability that a randomly-placed λ-tile contains no transitions, given that it lies in a l-spacing, is given by (*cf.* figure 16),

$$p_1^{\rm E}(\lambda \mid l) = \begin{cases} 0 , & \text{for } \lambda > l ; \\ 1 - \lambda/l , & \text{for } \lambda \leq l . \end{cases} \tag{4.3}$$

The probability that a λ-tile lies in a l-spacing is given by the geometric weighting of the scales, $m_1(l)$; *cf.* equation (4.1). By a λ-tile lying in a l-spacing we mean that a chosen (reference) point of the tile, *e.g.*, the left endpoint of the tile, lies in a l-spacing, *cf.* figure 16. The probability that a λ-tile does not contain any transitions is then (*cf.* equations (4.1)–(4.3)),

$$\tilde{p}_1^{\mathrm{E}}(\lambda) \;=\; \int_\lambda^\infty \left(\frac{l-\lambda}{l_{\mathrm{m}}}\right) p_1(l)\,\mathrm{d}l \;. \tag{4.4}$$

To make the connection to coverage statistics, consider a L-record, $L \gg l_{\mathrm{m}}$, partitioned in λ-tiles, $\lambda \leq L$. Let $N_1(\lambda;L)$ be the coverage count, *i.e.*, the (ensemble-averaged) number of nonoverlapping, contiguous λ-tiles necessary to cover all points (threshold level transitions) in the L-record. Consider the coverage fraction, $F_1(\lambda)$, *i.e.*, the ratio of the number of tiles that cover transitions to the total number of tiles (Dimotakis 1991c, Catrakis & Dimotakis 1996a). For homogeneous statistics, this can be written as,

$$F_1(\lambda) \;=\; 1 - \lim_{L/\lambda\to\infty}\left\{\frac{N_1^{(\mathrm{E})}(\lambda)}{N_1^{(\mathrm{T})}(\lambda)}\right\} \;=\; 1 - \tilde{p}_1^{\mathrm{E}}(\lambda)\;, \tag{4.5}$$

where $N_1^{(\mathrm{T})}(\lambda) = N_1(\lambda) + N_1^{(\mathrm{E})}(\lambda)$ is the total number of λ-tiles and $N_1^{(\mathrm{E})}(\lambda)$ is the number of empty λ-tiles in the L-record.** The coverage fraction can then be expressed as (*cf.* equation (4.4)),

$$F_1(\lambda) \;=\; 1 - \int_\lambda^\infty \left(\frac{l-\lambda}{l_{\mathrm{m}}}\right) p_1(l)\,\mathrm{d}l \;=\; \frac{1}{l_{\mathrm{m}}}\int_0^\lambda \int_{\lambda'}^\infty p_1(l)\,\mathrm{d}l\,\mathrm{d}\lambda\;. \tag{4.6}$$

The limiting behavior of $F_1(\lambda)$, at small or large coverage scales, is then,

$$F_1(\lambda) \quad \begin{cases} \sim\; \lambda/l_{\mathrm{m}} \to 0\;, & \text{as } \lambda \to 0\;; \\ \to\; 1\;, & \text{as } \lambda \to \infty\;. \end{cases} \tag{4.7}$$

The corresponding SDF dimension (Dimotakis 1991c, Catrakis & Dimotakis 1996a),

$$D_1(\lambda) \;\equiv\; -\frac{\mathrm{d}\log N_1(\lambda)}{\mathrm{d}\lambda} \;=\; 1 - \frac{\mathrm{d}\log F_1(\lambda)}{\mathrm{d}\log\lambda} \tag{4.8}$$

** An incorrect relation between $F_1(\lambda)$ and $\tilde{p}_1^{\mathrm{E}}(\lambda)$ has been given in Vassilicos 1991 and Vassilicos & Hunt 1991. Equation 2.4 in those references reads (in the present notation), $F_1(\lambda) = 1 - \int_\lambda^\infty \tilde{p}_1^{\mathrm{E}}(\lambda')\mathrm{d}\lambda'$.

(the latter in 1-D) can be expressed in terms of the pdf of spacing scales, *i.e.*,

$$D_1(\lambda) \;=\; 1 - \frac{\lambda \int_\lambda^\infty p_1(l)\,\mathrm{d}l}{l_\mathrm{m} - \int_\lambda^\infty (l-\lambda)\,p_1(l)\,\mathrm{d}l} \;=\; 1 - \frac{\lambda \int_\lambda^\infty p_1(l)\,\mathrm{d}l}{\int_0^\lambda \int_{\lambda'}^\infty p_1(l)\,\mathrm{d}l\,\mathrm{d}\lambda'} \;. \tag{4.9}$$

Two limiting cases follow from equation (4.9),

$$D_1(\lambda) \;\rightarrow\; \begin{cases} 0 \;, & \text{as } \lambda \rightarrow 0 \;; \\ 1 \;, & \text{as } \lambda \rightarrow \infty \;, \end{cases} \tag{4.10}$$

as required for the coverage of 1-D transition sets (*cf.* Dimotakis 1991c). Equation (4.9) can be viewed as a SDF transform, connecting $p_1(l)$ to $D_1(\lambda)$.

4.2 Inverse relations in 1-D

Inverse relations connecting the pdf of spacing scales to the SDF dimension (or coverage fraction) can also be obtained. From equation (4.6), we have,

$$\frac{\mathrm{d}F_1(\lambda)}{\mathrm{d}\lambda} \;=\; \frac{1}{l_\mathrm{m}} \int_\lambda^\infty p_1(l)\,\mathrm{d}l \;, \tag{4.11}$$

and, therefore,

$$p_1(l) \;=\; -\,l_\mathrm{m}\,\frac{\mathrm{d}^2 F_1(l)}{\mathrm{d}l^2} \;. \tag{4.12}$$

Note that a relation similar to equation (4.12) was obtained by Longuet-Higgins (1958) in the context of zero-crossings of random Gaussian functions. The mean spacing scale, l_m, can then be written as (*cf.* equation (4.11)),

$$\frac{1}{l_\mathrm{m}} \;=\; \lim_{\lambda\rightarrow 0} \left\{ \frac{\mathrm{d}F_1(\lambda)}{\mathrm{d}\lambda} \right\} \;, \tag{4.13}$$

in agreement with the small-scale behavior of the coverage fraction (*cf.* equation (4.7)). Since the coverage fraction can also be written in terms of the SDF dimension as (Catrakis & Dimotakis 1996a)

$$F_1(\lambda) \;=\; \exp\left\{ -\int_\lambda^\infty \Big[1 - D_1(\lambda')\Big]\,\frac{\mathrm{d}\lambda'}{\lambda'} \right\} \;, \tag{4.14}$$

it follows that,

$$\frac{\mathrm{d}F_1(\lambda=0)}{\mathrm{d}\lambda} \;=\; \lim_{\lambda\rightarrow 0} \left\{ \frac{1}{\lambda} \exp\left[-\int_\lambda^\infty [1 - D_1(\lambda')]\,\frac{\mathrm{d}\lambda'}{\lambda'} \right] \right\} \;. \tag{4.15}$$

Combining equations (4.12), (4.14), and (4.15) we obtain the (inverse) relation connecting the pdf of spacing scales to the SDF dimension, *i.e.*,

$$p_1(l) = \frac{l_m}{l^2}\left\{D_1(l)\left[1 - D_1(l)\right] + l\,\frac{dD_1(l)}{dl}\right\} \times \exp\left\{-\int_l^\infty \left[1 - D_1(l')\right]\frac{dl'}{l'}\right\} , \tag{4.16}$$

where the mean scale, l_m, is given by (*cf.* Eqs. 4.13 and 4.15),

$$l_m = \lim_{l\to 0}\left\{l\,\exp\left[\int_l^\infty \left[1 - D_1(l')\right]\frac{dl'}{l'}\right]\right\} . \tag{4.17}$$

4.3 Alternative 1-D theory: largest-empty-tile scales

An alternative measure of geometric scale, in 1-D, that can also be connected to coverage statistics, is the largest-empty-tile scale. This scale is the size of the largest tile, (centered) at a random location, that is empty. The pdf of this scale, $f_1(\lambda)$, is also the probability (density) that a random point is a distance $\lambda/2$ away from the nearest element of the point set (and, equivalently, it is proportional to the number fraction of intervals greater than λ), given by,

$$f_1(\lambda) = \int_0^\infty h_E(\lambda \mid l)\, m_1(l)\, dl , \tag{4.18}$$

where the conditional probability, $h_E(\lambda \mid l)$, that a randomly-placed λ-tile is the largest-empty-tile, given that it lies in a l-interval, is given by,

$$h_E(\lambda \mid l) = \begin{cases} 0, & \text{if } \lambda > l \\ 1/2l, & \text{if } \lambda = l \\ 1/l, & \text{if } \lambda < l \end{cases} , \tag{4.19}$$

and the probability that a λ-tile lies in a l-spacing is given by $m_1(l)$, *cf.* equation (4.2) and related discussion. Note that, in equation (4.19), for the case $\lambda = l$, there is only one point $\lambda/2$ away from the nearest element of the set (*i.e.*, the point that is at the middle of the l-interval), while for $\lambda < l$, there are two points that are $\lambda/2$ away. The distribution of largest-empty-tile scales can be connected, therefore, to the distribution of spacing scales, *i.e.*,

$$f_1(\lambda) = \frac{1}{2l_m}\lim_{\epsilon\to 0}\int_{\lambda-\epsilon}^{\lambda+\epsilon} p_1(l)\, dl + \frac{1}{l_m}\lim_{\epsilon\to 0}\int_{\lambda+\epsilon}^{\infty} p_1(l)\, dl . \tag{4.20}$$

For finite $p_1(l)$, this simplifies to,

$$f_1(\lambda) \;=\; \frac{1}{l_{\rm m}} \int_{\lambda}^{\infty} p_1(l)\,{\rm d}l \;=\; \frac{{\rm d}F_1(\lambda)}{{\rm d}\lambda} \;, \tag{4.21}$$

and, consequently, the distribution of largest-empty-tile scales can be connected to the (1-D) coverage statistics (combining Eqs. 4.6, 4.9, and 4.21), *i.e.*,

$$D_1(\lambda) \;=\; 1 \;-\; \frac{\lambda\, f_1(\lambda)}{\int_0^{\lambda} f_1(\lambda')\,{\rm d}\lambda'} \;, \tag{4.22}$$

and,

$$f_1(\lambda) \;=\; \frac{1 - D_1(\lambda)}{\lambda} \exp\left\{ -\int_{\lambda}^{\delta} [1 \;-\; D_1(\lambda')]\, \frac{{\rm d}\lambda'}{\lambda'} \right\} \;, \tag{4.23}$$

which offer alternative SDF transforms (*cf.* Eqs. 4.9 and 4.16).

4.4 Applications of 1-D theory

Zero-crossings of velocity signals derived from 1-D measurements in turbulent boundary layers have been reported as well approximated by Poisson statistics (Sreenivasan, Prabhu, and Narasimha 1983, Kailasnath and Sreenivasan 1993). Constant fractal (PLF) dimensions were reported derived from such signals (Sreenivasan 1991). The SDF dimension corresponding to Poisson point processes, *i.e.*,

$$p_1(l)\,{\rm d}l \;=\; \exp(-l/l_{\rm m})\,{\rm d}l/l_{\rm m} \;, \tag{4.24}$$

is given by,

$$D_d(\lambda) \;=\; 1 \;-\; \frac{\lambda/l_{\rm m}}{e^{\lambda/l_{\rm m}} - 1} \;; \tag{4.25}$$

cf. equation (4.9). Figure 17 compares $D_d(\lambda)$, from equation (4.25), to the coverage dimension from five Monte-Carlo simulations. For each simulation, a randomly-placed L-record, where $L/l_{\rm m} = 1000$, was successively partitioned into smaller λ-tiles and the coverage count computed for each λ. The error bars indicate the standard deviation of the ensemble-averaged Monte-Carlo estimates. Such SDF behavior may be expected to be encountered in geometries generated by natural phenomena that are described by Poisson statistics.

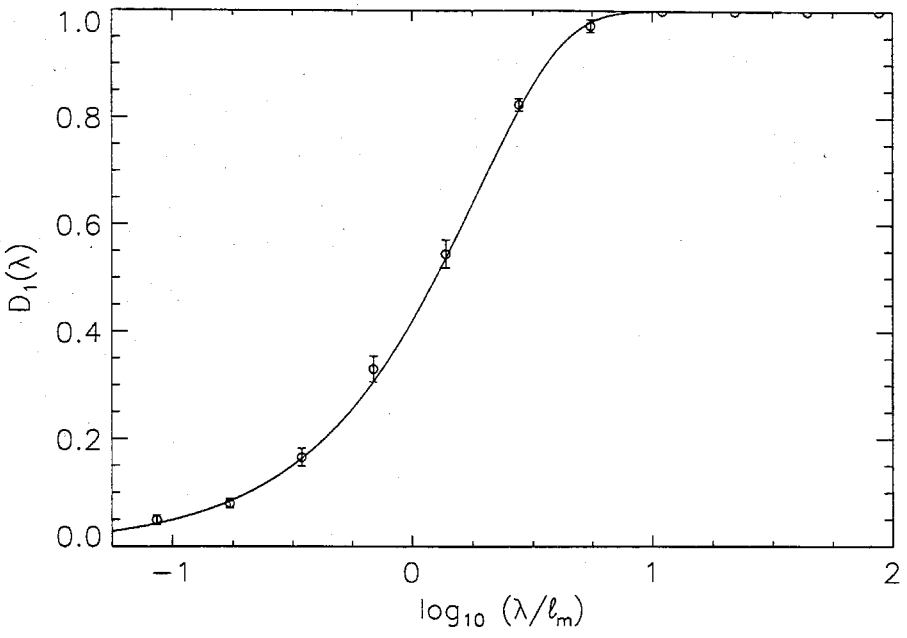

FIGURE 17 SDF dimension, $D_1(\lambda)$, for exponential pdf of spacing scales with $\alpha = 0.5$. Theory: solid line (4.25); simulations: circles.

Exploratory investigations of the *mean* zero-crossing frequency (mean spacing scale, l_m) of 1-D velocity signals in turbulence had been reported by Liepmann (1949). No measurements of the pdf of zero-crossing scales were reported, however, until the 1970's-80's (see Sreenivasan, Prabhu, and Narasimha 1983, and references therein). This can be appreciated in terms of the technological developments in high-speed, real-time data acquisition needed for these measurements.†

In several turbulent flows, level crossings of 1-D scalar and velocity measurements have been reported as well approximated by the lognormal distribution. In turbulent jets, a lognormal distribution was indicated for level crossings of 1-D scalar measurements (Miller and Dimotakis 1991a). Lognormal statistics were also indicated for level-crossings of 1-D scalar measurements in plumes dispersing in the atmospheric surface layer (Yee *et al.* 1995) as well as zero-crossings of 1-D velocity measurements in turbulent boundary layers (Sreenivasan, Prabhu, and Narasimha 1983; in addition to exponential-distribution fits). The SDF dimension corresponding to a lognormal distribution,

$$p_1(l)\,\mathrm{d}l \;=\; \exp\left\{-\left[\ln(l/l_m)/\sigma + \sigma/2\right]^2/2\right\}\,\mathrm{d}l/(\sqrt{2\pi}\sigma l)\;, \qquad (4.26)$$

† D. Coles, private communication.

is given by,

$$D_1(\lambda) = 1 - \left\{ 1 + \frac{l_m}{\lambda} \left[\frac{1 + \mathrm{erf}\left[(\ln(\lambda/l_m)/\sigma - \sigma/2)/\sqrt{2} \right]}{1 - \mathrm{erf}\left[(\ln(\lambda/l_m)/\sigma + \sigma/2)/\sqrt{2} \right]} \right] \right\}^{-1} ; \qquad (4.27)$$

cf. equation (4.9). A comparison between this expression and results from five Monte-Carlo simulations, with $L/l_m = 3000$ records, is shown in equation (18). The results agree with previous simulations that used a lognormal point-spacing distribution (Miller and Dimotakis 1991a). Generally speaking, stochastic fragmentation processes result in lognormal distributions, as noted by Kolmogorov (1941), as do fusion/agglomeration processes (Lopez 1977).

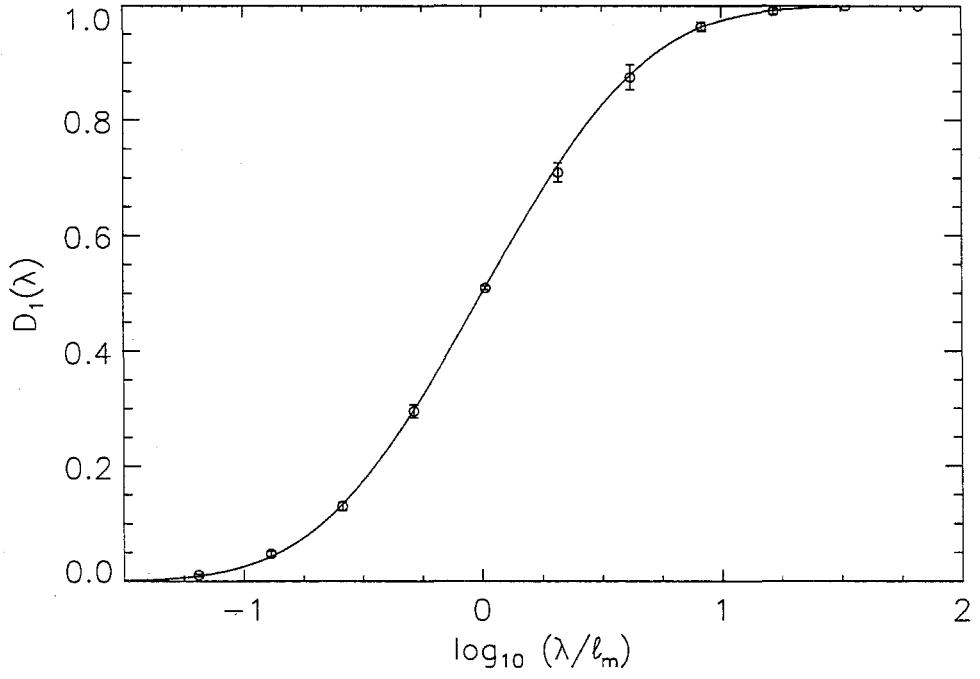

FIGURE 18 $D_1(\lambda)$, for lognormal pdf of spacing scales with $\sigma = 1$. Theory: solid line (4.27); simulations: circles.

Power-law scaling statistics, over a finite range of scales, *e.g.*,

$$p(l)\,\mathrm{d}l = \begin{cases} a\,\mathrm{d}l/l_1\,, & \text{for } l \le l_1\ ; \\ a\,(l/l_1)^{-\nu}\mathrm{d}l/l_1, & \text{for } l_1 < l \le l_2\ ; \\ 0\,, & \text{for } l_2 < l\ , \end{cases} \qquad (4.28)$$

with the mean spacing scale, l_m, given by,

$$\frac{l_m}{l_1} = \frac{\nu - 1}{2 - \nu} \left(\frac{\alpha^{2-\nu} - \nu/2}{\nu - \alpha^{1-\nu}} \right) , \qquad (4.29)$$

correspond to a fractal dimension (for $\nu \neq 1, 2$) given by,

$$D_1(\lambda) = \begin{cases} \dfrac{\lambda/l_1}{2\left(\nu - \alpha^{1-\nu}\right)/(\nu-1) \; - \; \lambda/l_1} \\ \dfrac{\beta l_1/\lambda + (1-\nu)(l_2/\lambda)^{\nu-1}}{2 - \nu + \beta l_1/\lambda - (l_2/\lambda)^{\nu-1}} \\ 1 \end{cases} , \tag{4.30}$$

in the respective scale ranges, where $\alpha \equiv l_2/l_1$ and $\beta \equiv \nu(\nu-1)\alpha^{\nu-1}/2$. Figure 19 plots $D_1(\lambda)$, as given by equation (4.30) and as computed from the coverage from five Monte-Carlo simulations with $L/l_m = 4000$ records, for $l_2/l_1 = 1000$ and $\nu = 3/2$.

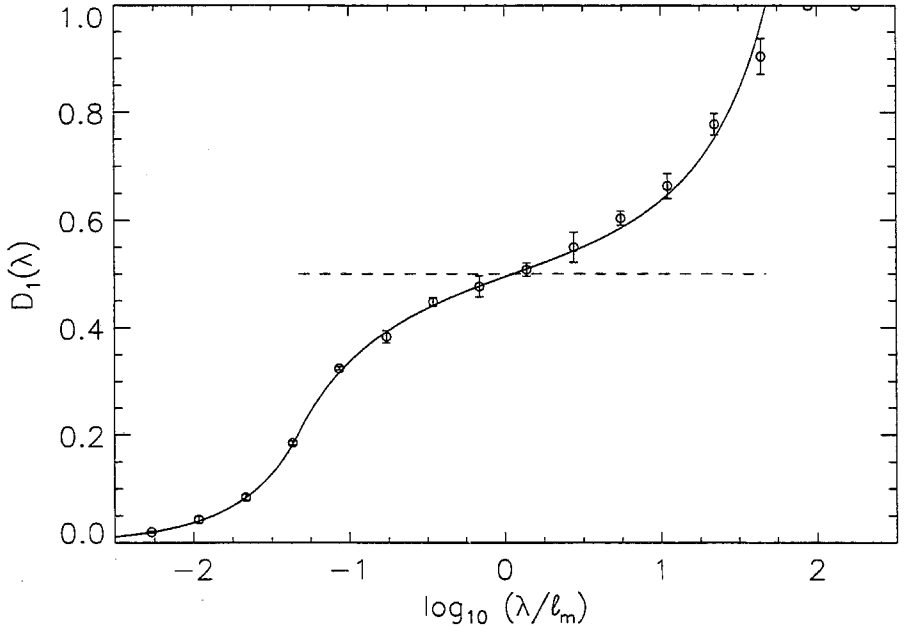

FIGURE 19 SDF dimension, $D_1(\lambda)$, for a power-law pdf of spacing scales with $\nu = 3/2$ and $l_2/l_1 = 1000$. Theory: solid line (4.25); simulations: circles.

In the limit of large l_2/l_1 and for scales $l_1 \ll l \ll l_2$, we have, for $1 < \nu < 2$,

$$D_1(\lambda) \; \rightarrow \; \nu - 1 \; . \tag{4.31}$$

This is indicated in figure 19 by the $D_1 = 1/2$ dashed line, corresponding to $\nu = 3/2$. Conversely, if $D_1(\lambda) = D_1 = \text{const.}$ in the range $\lambda_1 \ll \lambda \ll \lambda_2$, figure 4.16 shows that,

$$p_1(l) \; \sim \; l^{-D_1 - 1} \; , \tag{4.32}$$

in this scale range. The scale dependence of $D_1(\lambda)$ in figure 19 is, in this case, a finite scale-range effect. We conclude that power-law scaling is best assessed in terms of the pdf's $p_1(l)$, or $f_1(\lambda)$.

4.5 Multidimensional theory: largest-empty-box (LEB) scales

In d-dimensional space, an extension of the notion of largest-empty-tile scales allows the connection between coverage statistics and the distribution of the corresponding multidimensional scales. Let $\mathcal{S}$ be a set consisting of points, lines, surfaces, *etc.*, that is embedded in a d-dimensional space, E_d.

For homogeneous spatial statistics, the coverage fraction, $F_d(\lambda)$, can be identified as the geometric probability that a (randomly-placed) λ-box covers part of $\mathcal{S}$; *cf.* (3.21). The coverage fraction can also be interpreted as a cumulative distribution function of a measure of spatial scales, in the following sense. For a scale increment, $\Delta\lambda$, the coverage fraction can be written as,

$$F_d(\lambda+\Delta\lambda) \equiv F_d(\lambda) + \int_{F_d(\lambda)}^{F_d(\lambda+\Delta\lambda)} \mathrm{d}F_d(\lambda') \ . \tag{4.33}$$

The differential coverage fraction, in this integral, can be associated with a probability density function of a measure of scales, $f_d(\lambda)$, where

$$f_d(\lambda) \equiv \frac{\mathrm{d}F_d(\lambda)}{\mathrm{d}\lambda} \ . \tag{4.34}$$

In this expression, $f_d(\lambda)$ is the probability density function of the *largest-empty-box* (LEB) scale, λ, *i.e.*, the size of the largest box that is empty, *i.e.*, covers no part of $\mathcal{S}$, as can be seen by the following considerations.

Consider a λ-box and a $(\Delta\lambda/2)$-wide strip, around the λ-box, as illustrated in figure 20. The identification of $f_d(\lambda)$, in (4.34), with the largest-empty-box scales can be established by considering the probabilities of the following three coverage events:

$$\begin{aligned}
\mathcal{A} &\equiv \{(\lambda+\Delta\lambda)\text{-box covers part of } \mathcal{S}\} \\
\mathcal{B} &\equiv \{\lambda\text{-box covers part of } \mathcal{S}\} \\
\mathcal{C} &\equiv \{(\Delta\lambda/2)\text{-wide strip, around } \lambda\text{-box covers part of } \mathcal{S}\} \ .
\end{aligned}$$

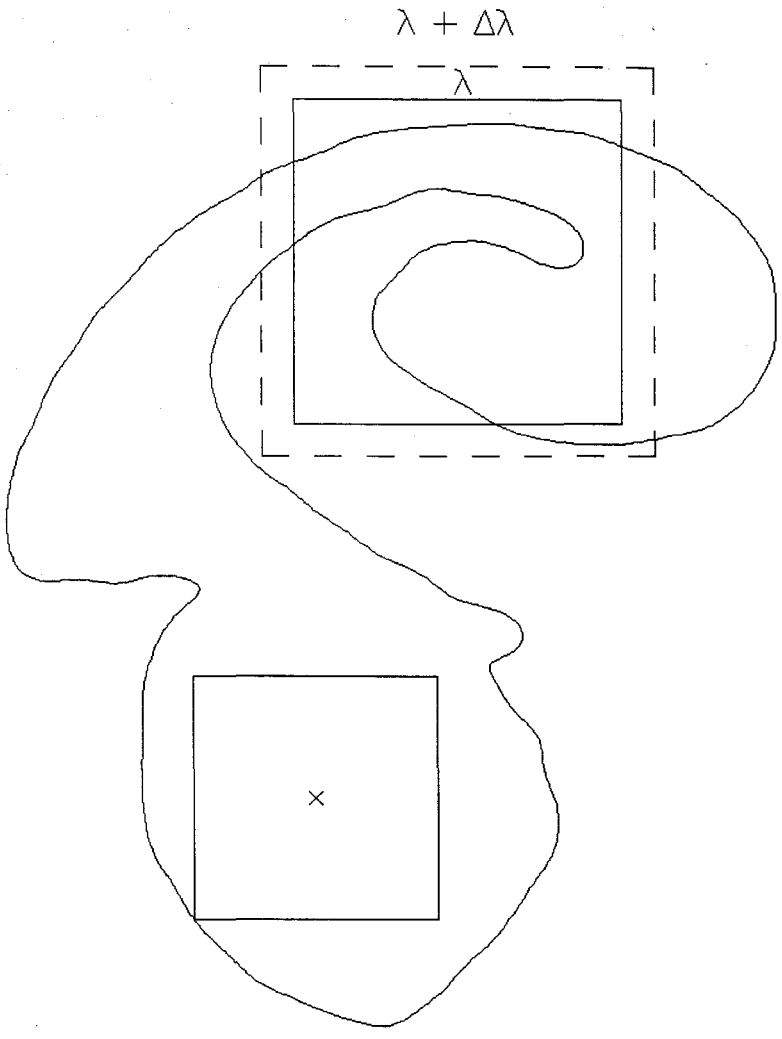

FIGURE 20 Illustration of a λ-box and a $(\lambda + \Delta\lambda)$-box, for relating geometric probabilities of coverage. An example of a LEB is also depicted.

The geometric probabilities of events $\mathcal{A}$, $\mathcal{B}$, and $\mathcal{C}$ are related as follows,

$$\mathcal{P}\{\mathcal{A}\} = \mathcal{P}\{\mathcal{B} \cup \mathcal{C}\} \equiv \mathcal{P}\{\mathcal{B}\} + \mathcal{P}\{\mathcal{C} \cap \overline{\mathcal{B}}\} \ . \tag{4.35}$$

Since,

$$F_d(\lambda + \Delta\lambda) = \mathcal{P}\{\mathcal{A}\} \qquad \text{and} \qquad F_d(\lambda) = \mathcal{P}\{\mathcal{B}\} \ , \tag{4.36}$$

we have, *cf.* (4.33),

$$\int_{F_d(\lambda)}^{F_d(\lambda+\Delta\lambda)} \mathrm{d}F_d(\lambda') = \mathcal{P}\{\mathcal{C} \cap \overline{\mathcal{B}}\} \ , \tag{4.37}$$

which is the probability that the $(\Delta\lambda/2)$-wide strip, around a λ-box, covers part of $\mathcal{S}$ *and* that the λ-box is empty.

This allows the connection between the coverage statistics and the distribution of this (multidimensional) measure of spatial scales, λ. In this context, this scale is identified as the size of the largest-empty-box that contains a randomly-located point, P, but contains no part of $\mathcal{S}$, *i.e.*, is empty. Equivalently, the scale λ is a measure of (twice) the distance from a point P to the nearest element of $\mathcal{S}$.

From equation (4.34) we see that $f_d(\lambda)$ satisfies the required normalization condition over the range of spatial scales, *i.e.*,

$$\int_0^\infty f_d(\lambda)\,\mathrm{d}\lambda \;=\; F_d(\infty) \,-\, F_d(0) \;=\; 1 \;, \tag{4.38}$$

cf. equations (4.7a,b). Integrating equation (4.34), we have the relation for the SDF coverage,

$$F_d(\lambda) \;=\; \int_0^\lambda f_d(\lambda')\,\mathrm{d}\lambda' \;. \tag{4.39}$$

The SDF dimension, $D_d(\lambda)$, can be expressed, therefore, in terms of the distribution of LEB scales, $f_d(\lambda)$, *i.e.*,

$$D_d(\lambda) \;=\; d \,-\, \frac{\lambda\, f_d(\lambda)}{\int_0^\lambda f_d(\lambda')\,\mathrm{d}\lambda'} \;, \tag{4.40}$$

cf. equation (3.24). This can be inverted to yield the LEB scale pdf from the SDF dimension, $D_d(\lambda)$, directly, *i.e.*,

$$f_d(\lambda) \;=\; \frac{d - D_d(\lambda)}{\lambda}\, F_d(\lambda) \;=\; \frac{d - D_d(\lambda)}{\lambda}\, \exp\left\{ -\int_\lambda^\infty [d \,-\, D_d(\lambda')]\,\frac{\mathrm{d}\lambda'}{\lambda'} \right\} \;; \tag{4.41}$$

cf. equations (3.26) and (4.34), which constitutes, therefore, the SDF transform pair in d-dimensional space.

The small-scale behavior of $f_d(\lambda)$ will be given by,

$$f_d(\lambda) \;\sim\; \lambda^{d-d_t-1} \;\rightarrow\; \begin{cases} \text{constant, as } \lambda \;\rightarrow\; 0, & \text{for } d_t = d-1 \;; \\ 0, \text{ as } \lambda \;\rightarrow\; 0, & \text{for } d_t < d-1 \;, \end{cases} \tag{4.42}$$

cf. equations (3.25a) and (4.34). The large-scale behavior of $f_d(\lambda)$ will be given by, *cf.* (3.25b),

$$f_d(\lambda) \rightarrow 0, \text{ as } \lambda \rightarrow \infty \ . \tag{4.43}$$

Equivalently, the SDF dimension can be expressed in terms of the distribution of the logarithm of LEB scales, $\tilde{f}_d(\log\lambda)$, *i.e.*,

$$D_d(\lambda) \ = \ d \ - \ \frac{\tilde{f}_d(\log\lambda)}{\int_{-\infty}^{\log\lambda} \tilde{f}_d(\log\lambda')\,\mathrm{d}\log\lambda'} \ , \tag{4.44}$$

cf. (4.40), where,

$$\tilde{f}_d(\log\lambda)\,\mathrm{d}\log\lambda \ \equiv \ f_d(\lambda)\,\mathrm{d}\lambda \ , \qquad \text{or,} \qquad \tilde{f}_d(\log\lambda) \ = \ \lambda\, f_d(\lambda) \ , \tag{4.45}$$

with a small-scale behavior given by,

$$\tilde{f}_d(\log\lambda) \ \sim \ \lambda^{d-d_t} \ \rightarrow \ 0 \ , \quad \text{as} \quad \lambda \rightarrow 0 \ , \tag{4.46}$$

unconditionally; *cf.* (4.42).

4.6 Inhomogeneous statistics

The multidimensional theory of the previous section was developed for homogeneous statistics. In this section, this theory is modified to account for (statistically) inhomogeneous, spatial, stochastic geometries, such as the isoscalar surfaces in turbulent-jet mixing. The scalar-field level set considered in this work, contained in the two-dimensional δ_b-box, is such an example.

Consider a set, $\mathcal{S}$, comprised of various geometric structures, *e.g.*, points, lines, surfaces, *etc.*, which is allowed to exhibit inhomogeneous statistics, and is contained in a d-dimensional bounding box of size δ_b, *e.g.*, for the isoscalar contours, the bounding box of size $\delta_\mathrm{b} = \sqrt{\lambda_x \lambda_y}$. The (box) coverage of $\mathcal{S}$ can be related to the distribution of (multidimensional) geometric scales spanned by $\mathcal{S}$, in the following sense. In this case, the coverage fraction, $F_d(\lambda)$, can be identified as the geometric probability that a (randomly-placed) λ-box, interior to the (outer) δ_b-box, covers

part of $\mathcal{S}$; *cf.* (3.21). In general, the probability of covering the set with a λ-box, interior to the $\delta_{\rm b}$-box, will be a function of position within the $\delta_{\rm b}$-box. For spatially inhomogeneous statistics, as is the case for the isoscalar contours considered in this work, the function $F_d(\lambda)$ represents the probability of coverage for a λ-tile placed in the $\delta_{\rm b}$-box without regard to its location.

For a scale increment $\Delta\lambda$, the coverage fraction can be written as,

$$F_d(\lambda+\Delta\lambda) \;=\; \mathcal{P}\{\,\mathcal{G}\cup\mathcal{H}\,\} \;\equiv\; \mathcal{P}\{\,\mathcal{G}\,\} \;+\; \mathcal{P}\{\,\mathcal{H}\cap\overline{\mathcal{G}}\,\}\;, \tag{4.47}$$

where $\mathcal{G}$ denotes coverage of part of $\mathcal{S}$ by a λ-box, interior to the (outer) $\delta_{\rm b}$-box, and $\mathcal{H}$ denotes coverage of part of $\mathcal{S}$ by a $(\Delta\lambda/2)$-wide strip around a λ-box interior to the $\delta_{\rm b}$-box. Since $F_d(\lambda) = \mathcal{P}\{\,\mathcal{G}\,\}$, it follows that

$$\int_{F_d(\lambda)}^{F_d(\lambda+\Delta\lambda)} {\rm d}F_d(\lambda') \;=\; \mathcal{P}\{\,\mathcal{H}\cap\overline{\mathcal{G}}\,\}\;, \tag{4.48}$$

— *cf.* equation (4.33) — which is the probability that a $(\Delta\lambda/2)$-wide strip, around a λ-box randomly placed interior to the $\delta_{\rm b}$-box, covers part of $\mathcal{S}$ *and* that the λ-box is empty.

In the limit, a pdf can be defined, therefore, as,

$$f_d(\lambda) \;\equiv\; \frac{{\rm d}F_d(\lambda)}{{\rm d}\lambda} \tag{4.49}$$

— *cf.* equation (4.34) — where $f_d(\lambda)$ is identified as the pdf of the LEB scales, or the size of the largest box, interior to the $\delta_{\rm b}$-box, that is empty, *i.e.*, covers no part of $\mathcal{S}$. This pdf satisfies the required normalization condition over the range of spatial scales, *i.e.*,

$$\int_0^{\delta_{\rm b}} f_d(\lambda)\,{\rm d}\lambda \;=\; F_d(\delta_{\rm b}) \;-\; F_d(0) \;=\; 1\;, \tag{4.50}$$

cf. equations (3.25a,b) and (4.49).

Therefore, the SDF dimension in d-dimensional space, for inhomogeneous statistics, is also expressible in terms of the pdf (Catrakis & Dimotakis 1996a), *i.e.*,

$$D_d(\lambda) \;\equiv\; d \;-\; \frac{{\rm d}\log F_d(\lambda)}{{\rm d}\log\lambda} \;=\; d \;-\; \frac{\lambda\, f_d(\lambda)}{\int_0^\lambda f_d(\lambda')\,{\rm d}\lambda'}\;. \tag{4.51}$$

This too is invertible for the distribution of LEB scales in terms of the SDF dimension, $D_d(\lambda)$ to yield (*cf.* equation (4.49)),

$$f_d(\lambda) \;=\; \frac{d - D_d(\lambda)}{\lambda} \exp\left\{ -\int_{\lambda}^{\delta_b} [d - D_d(\lambda')] \frac{\mathrm{d}\lambda'}{\lambda'} \right\} \;. \tag{4.52}$$

The small-scale behavior of $f_d(\lambda)$ will be given by,

$$f_d(\lambda) \;\sim\; \lambda^{d-d_t-1} \;\rightarrow\; \begin{cases} \text{constant, as } \lambda \;\rightarrow\; 0, & \text{for } d_t = d-1 \;; \\ 0, \text{ as } \lambda \;\rightarrow\; 0, & \text{for } d_t < d-1 \;, \end{cases} \tag{4.53}$$

cf. equations (3.25a) and (4.49). For the isoscalar contours considered in this work, for which $d_t = 1$ and $d = 2$, the limit of $f_d(\lambda)$ at the small scales can be related to the small-scale limit of the coverage length, *cf.* (3.19) and (3.20), *i.e.*,

$$\delta_b \, f_2(\lambda \rightarrow 0) \;=\; \frac{L_2(\lambda \rightarrow 0)}{\delta_b} \;. \tag{4.54}$$

It follows that this limit is also a measure of the surface-to-volume ratio (perimeter-to-area in 2-D) of the isosurfaces, *i.e.*,

$$f_2(\lambda \rightarrow 0) \;=\; \frac{L_2(\lambda \rightarrow 0)}{\delta_b^2} \;. \tag{4.55}$$

The large-scale limiting behavior of $f_d(\lambda)$ is given by, *cf.* equation (3.25b),

$$f_d(\lambda) \;\rightarrow\; 0, \text{ as } \lambda \;\rightarrow\; \delta_b \;. \tag{4.56}$$

4.7 Remarks

The LEB scale distribution offers an additional interpretation in terms of surface-to-volume ratio. Specifically, for isosurfaces, $f_2(\lambda)$ measures the surface-to-volume ratio (perimeter-to-area ratio in 2-D) of surfaces (contours in 2-D), spaced by $\lambda/2$ (within a proportionality constant) from the isosurface (Huygens construction), with $f_2(\lambda \rightarrow 0)$ a measure of the surface-to-volume ratio of the isosurface (Catrakis and Dimotakis 1996b).

The above analysis shows that SDF-geometric statistics, such as the coverage fraction or dimension, are invertible and can be used to compute the distribution of geometric scales. Specifically, the connection between fractal dimensions (SDF or PLF) and the distribution of LEB scales, of the set being covered, has been obtained in the form of a SDF transform pair which is rewritten here to summarize ((4.9) and (4.16)),

$$\begin{aligned} D_1(\lambda) &= 1 - \frac{\lambda \int_\lambda^\infty p_1(l)\,\mathrm{d}l}{\int_0^\lambda \int_{\lambda'}^\infty p_1(l)\,\mathrm{d}l\,\mathrm{d}\lambda'} \;; \\ p_1(l) &= \frac{l_\mathrm{m}}{l^2}\left\{D_1(l)\left[1 - D_1(l)\right] + l\,\frac{\mathrm{d}D_1(l)}{\mathrm{d}l}\right\}, \\ &\quad \times \exp\left\{-\int_l^\infty \left[1 - D_1(l')\right]\frac{\mathrm{d}l'}{l'}\right\} \end{aligned} \tag{4.57}$$

in one-dimensional space and (4.40) and (4.41),

$$\begin{aligned} D_d(\lambda) &= d - \frac{\lambda\, f_d(\lambda)}{\int_0^\lambda f_d(\lambda')\,\mathrm{d}\lambda'} \;; \\ f_d(\lambda) &= \frac{d - D_d(\lambda)}{\lambda} \exp\left\{-\int_\lambda^\infty \left[d - D_d(\lambda')\right]\frac{\mathrm{d}\lambda'}{\lambda'}\right\} \end{aligned}, \tag{4.58}$$

in multi-dimensional (d-dimensional) space (or, also, in one-dimensional space).

As an example of a scale distribution which is relevant in turbulent mixing, a two-dimensional lognormal model is considered in Section 5.8. Also, in addition to the examples worked out in Section 4.4, other models of one-dimensional scale distributions are included in Appendix D.

CHAPTER 5

Geometry of isosurfaces

Further analysis of the geometry of the isoscalar surfaces, or contours in 2-D (*cf.* chapter 2), derived from the scalar-field data in these experiments, was performed in terms of the following (fractal) measures: the coverage, $N_2(\lambda)$, the coverage-length, $L_2(\lambda)$, the SDF dimension, $D_2(\lambda)$, the coverage fraction, $F_2(\lambda)$, and the distribution of largest-empty-box (LEB) scales, *i.e.*, $f_2(\lambda)$ and $\tilde{f}_2(\log\lambda)$. These were investigated as a function of scalar threshold, for each of the three jet Reynolds numbers in these experiments. Scalar-threshold effects on each measure will be discussed first, and an assessment of Reynolds number effects on the coverage will be discussed near the end of this chapter (section 5.7).

Note that the probability-density function of a field (alone) does not provide enough information to determine *level set* statistics of the (instantaneous) field, such as the ones mentioned above (*cf.* Yee *et al.* 1995). Yet, it is such (level set) statistics that can be relied upon to investigate the multiscale structure of isosurfaces, *e.g.*, by computing the distribution of (LEB) scales of scalar isosurfaces in turbulent mixing, or of other isosurfaces in turbulence, or of interfaces in complex natural phenomena, in general.

5.1 Example of isosurface coverage

The geometric measures to be investigated in this chapter are based on the coverage count of the isosurfaces (contours), $N_2(\lambda; c, Re)$. A new method to compute an estimate of this coverage was developed that removes several shortcomings of conventional box-counting methods. The proposed method successively subdivides the bounding box for the isoscalar (level) set, and computes the number of partition boxes that contain part of the level set. This Bounding-Box Partition Method (BBPM) is discussed in Appendix A, where its performance is compared to conventional box-counting methods. Isosurfaces used in the computation of the coverage-based measures were computed as the level sets of the scalar-image data, using a bilinear B-spline representation of the jet-fluid concentration $c(x, y)$-surface derived from each image. This method removes several difficulties of conventional pixel-based contour-identification methods and yields a representation for the isosurfaces that is well suited for the investigation of coverage-based measures.

To illustrate the nature of the coverage process, as a function of scale, Figures 21a-i depict a sequence of coverage at successively smaller scales, for the isosurface data depicted in figure 9a. In the first stage (figure 21a), the bounding box for the isosurface is depicted, which is subsequently subdivided (partitioned) in the remainder of the sequence. The total number of boxes, $N_{2,\mathrm{tot}}(\lambda)$, as well as the number of boxes that cover part of the isosurface, $N_2(\lambda)$, are stated in the captions corresponding to the figures. In figures 21a-g, all λ-boxes that consititute the partitioned bounding box are depicted; boxes that cover the level set are shown shaded. In figures 21h-i, only those boxes that cover the set are shown, for clarity. A visual inspection of this sequence confirms the expectation that, at the large coverage scales, the isosurface fills the area it is embedded in, while, at the small coverage scales, the area-fraction approaches zero; the coverage boxes converge to the level set, in the limit of small λ-scales.

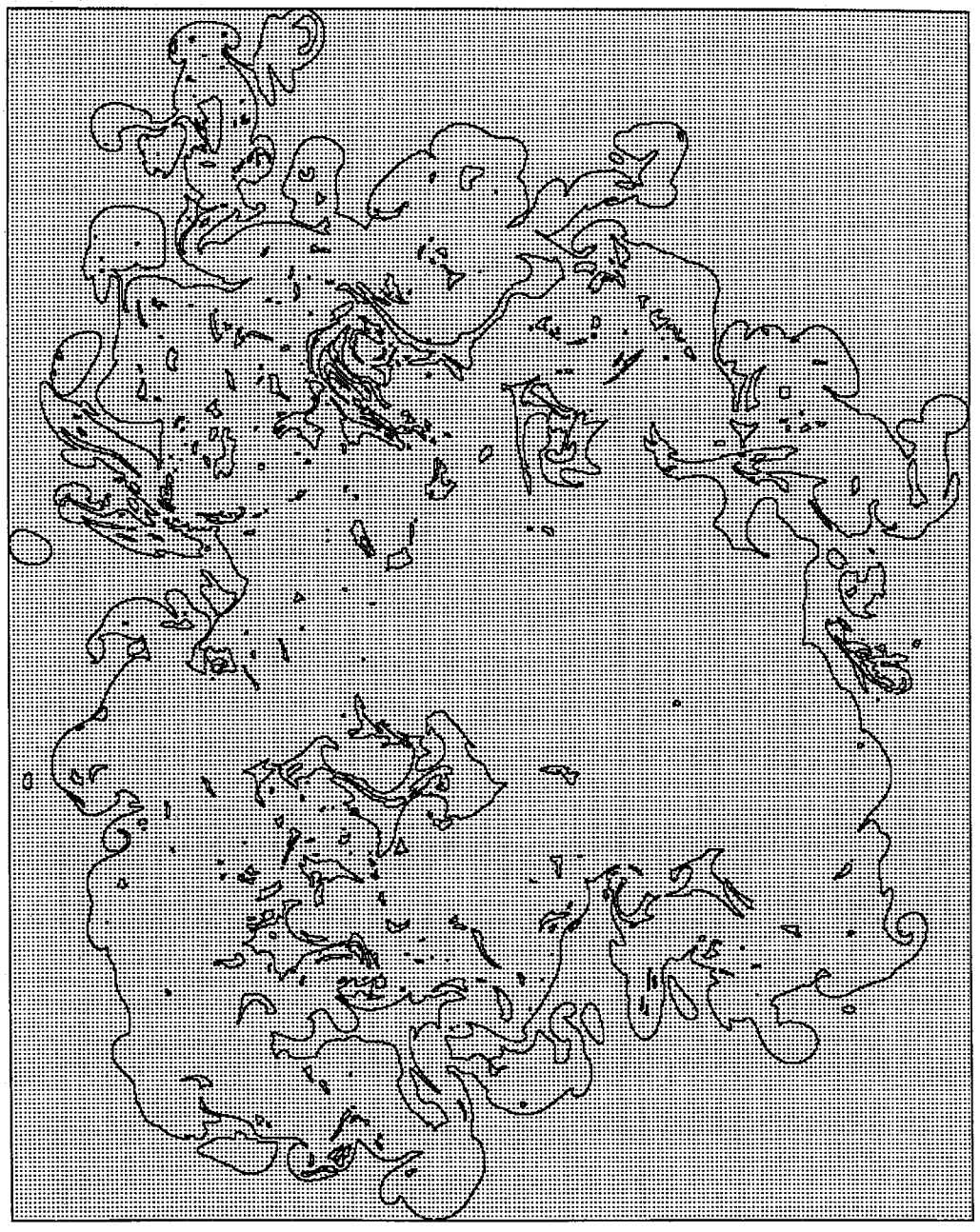

FIGURE 21 Example of isosurface coverage at $Re \simeq 4.5 \times 10^3$ and $c = c_1$ (*cf.* figure 9a). (a) Coverage at $\lambda = \delta_b$: $N_2 = 1$, $N_{2,\mathrm{tot}} = 1$.

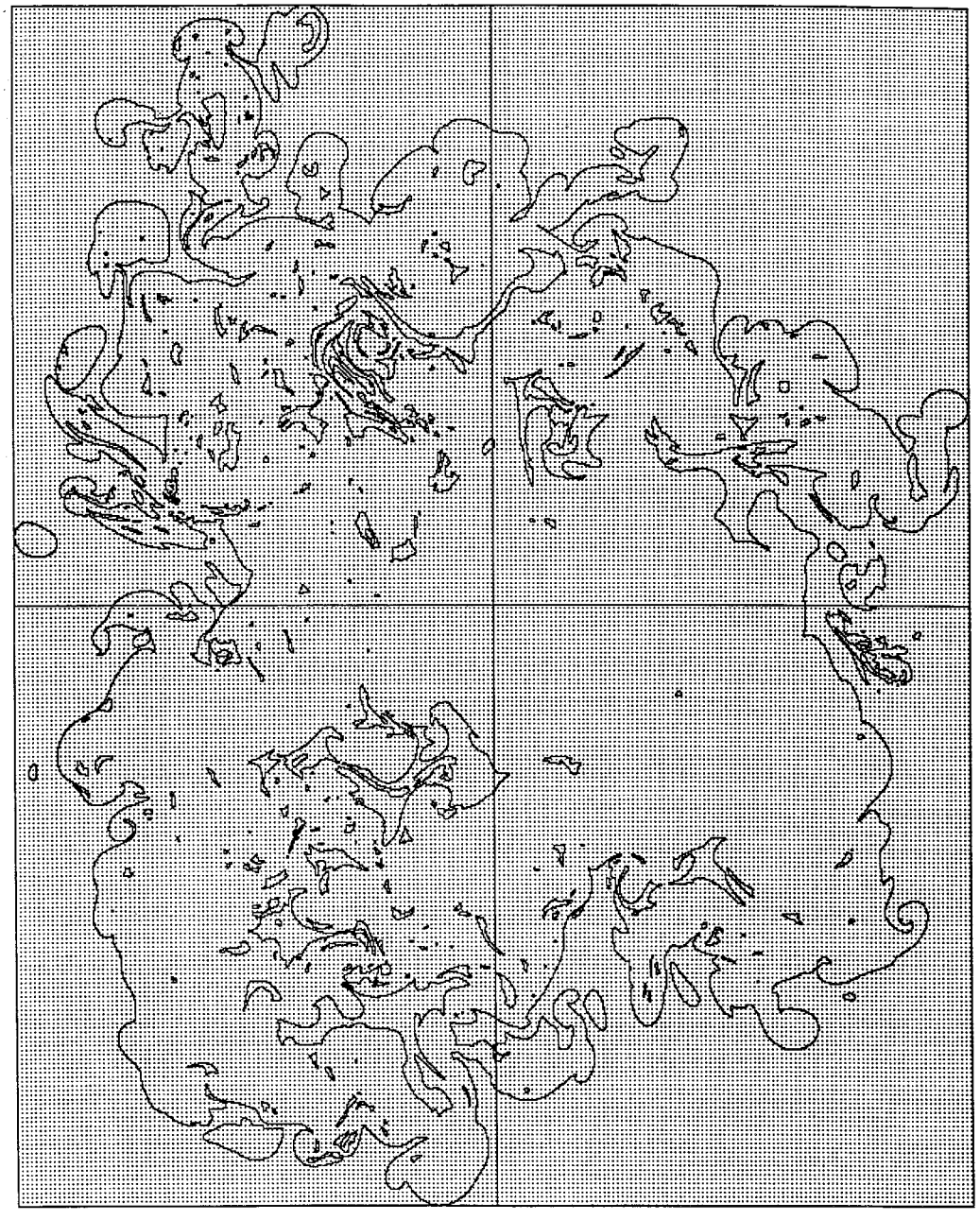

FIGURE 21 (b) $\lambda = \delta_b/2$; $N_2 = 4$, $N_{2,\mathrm{tot}} = 4$.

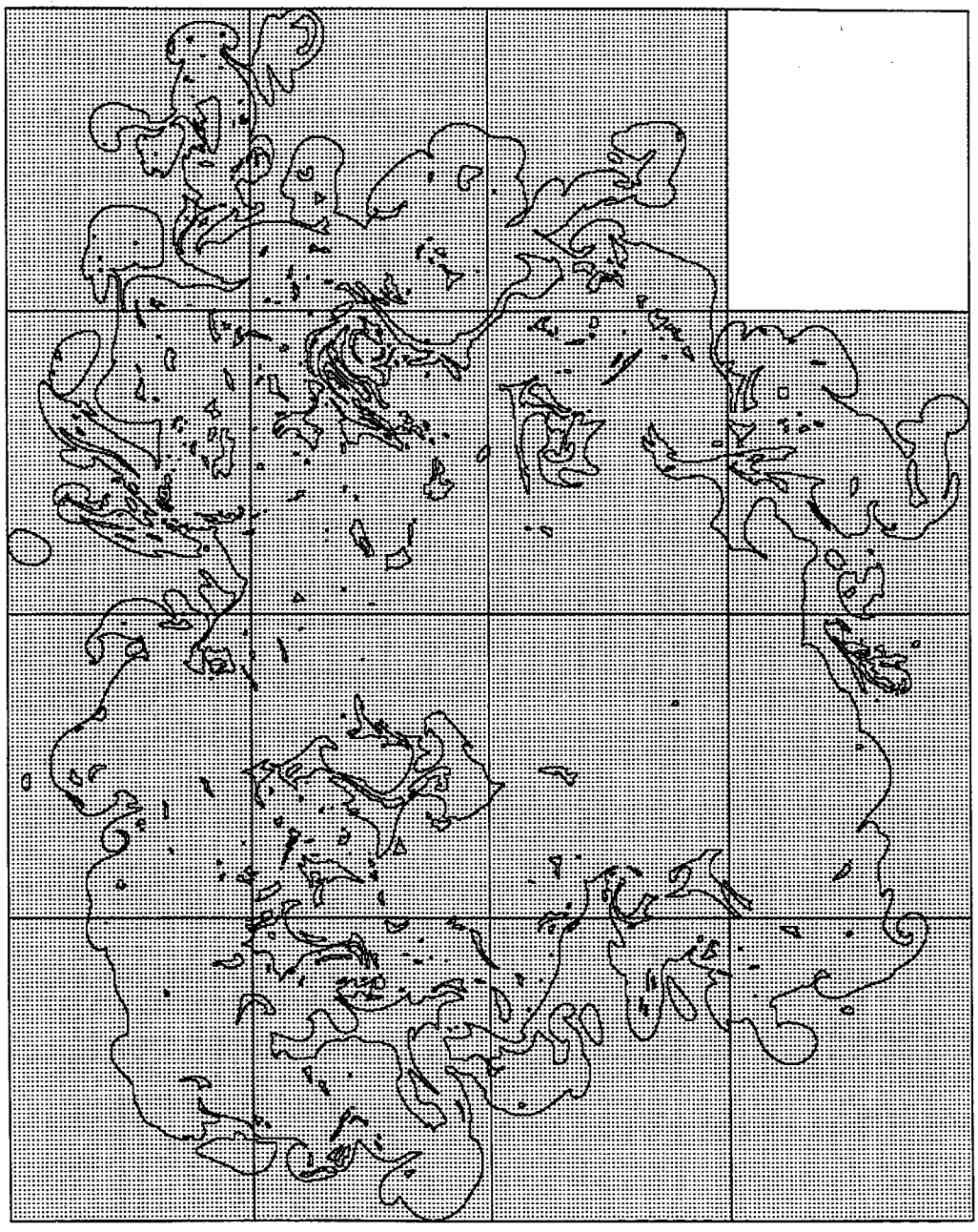

FIGURE 21 (c) $\lambda = \delta_b/4$; $N_2 = 15$, $N_{2,\mathrm{tot}} = 16$.

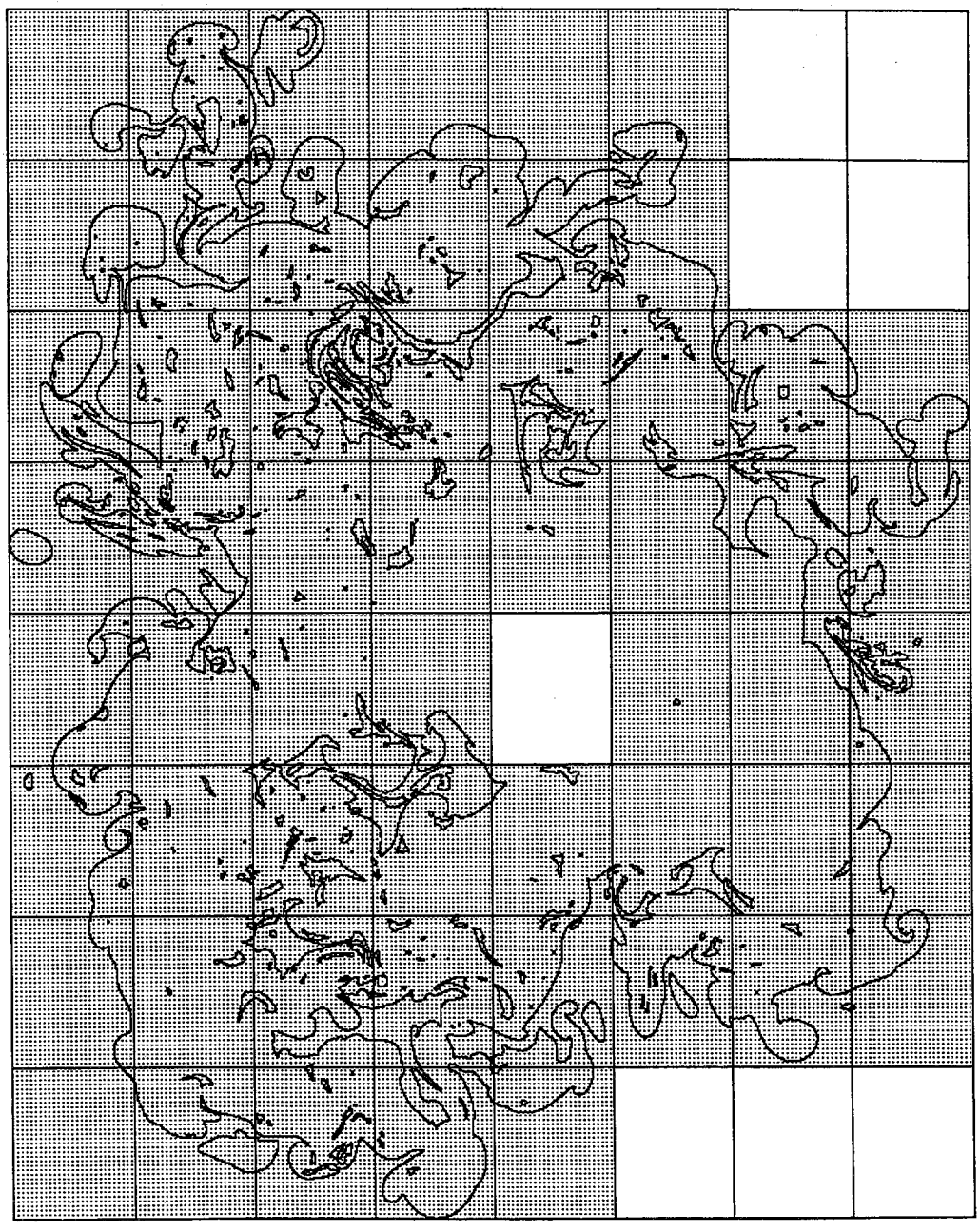

FIGURE 21 (d) $\lambda = \delta_b/8$; $N_2 = 56$, $N_{2,\mathrm{tot}} = 64$.

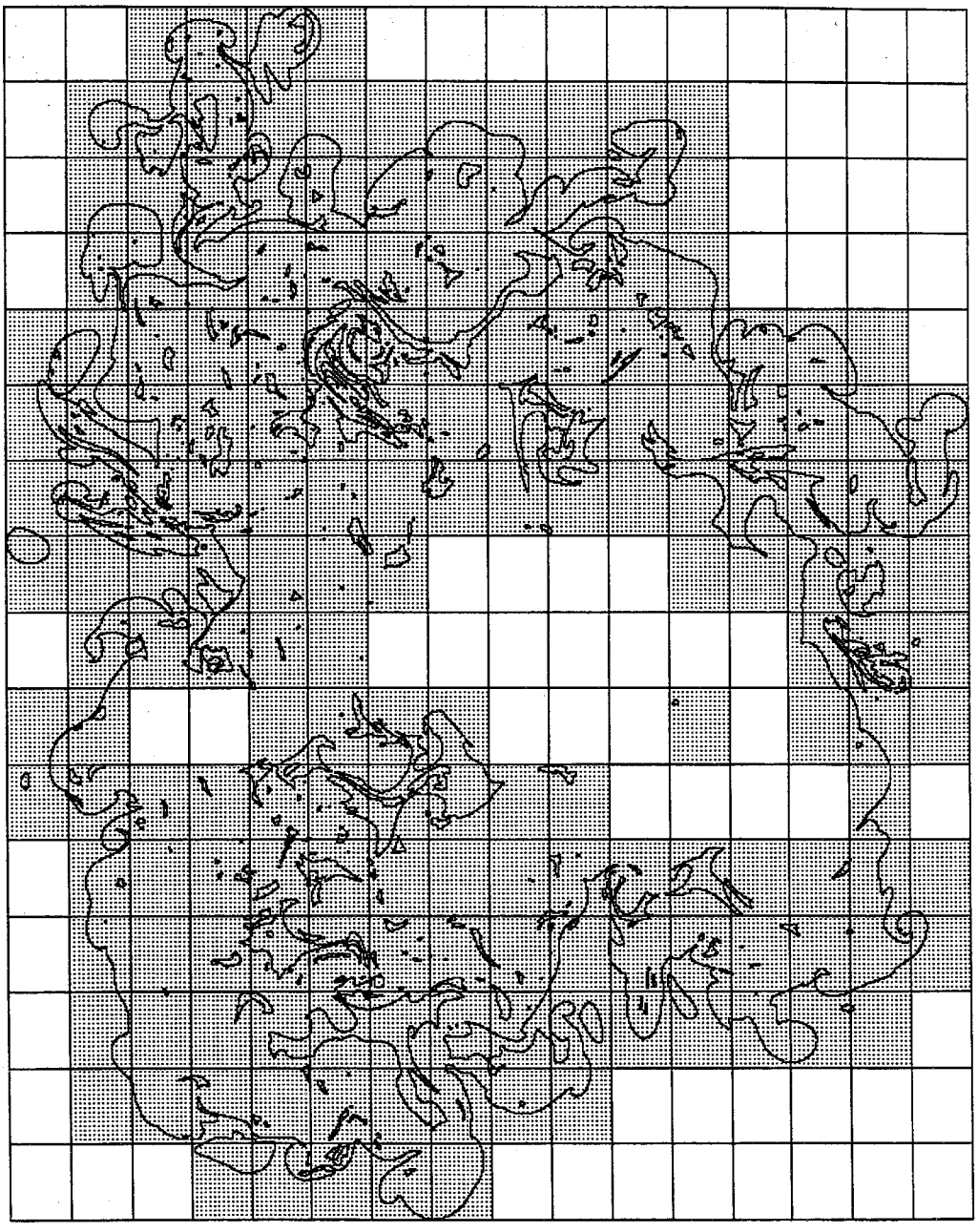

FIGURE 21 (e) $\lambda = \delta_b/16$; $N_2 = 183$, $N_{2,\mathrm{tot}} = 256$.

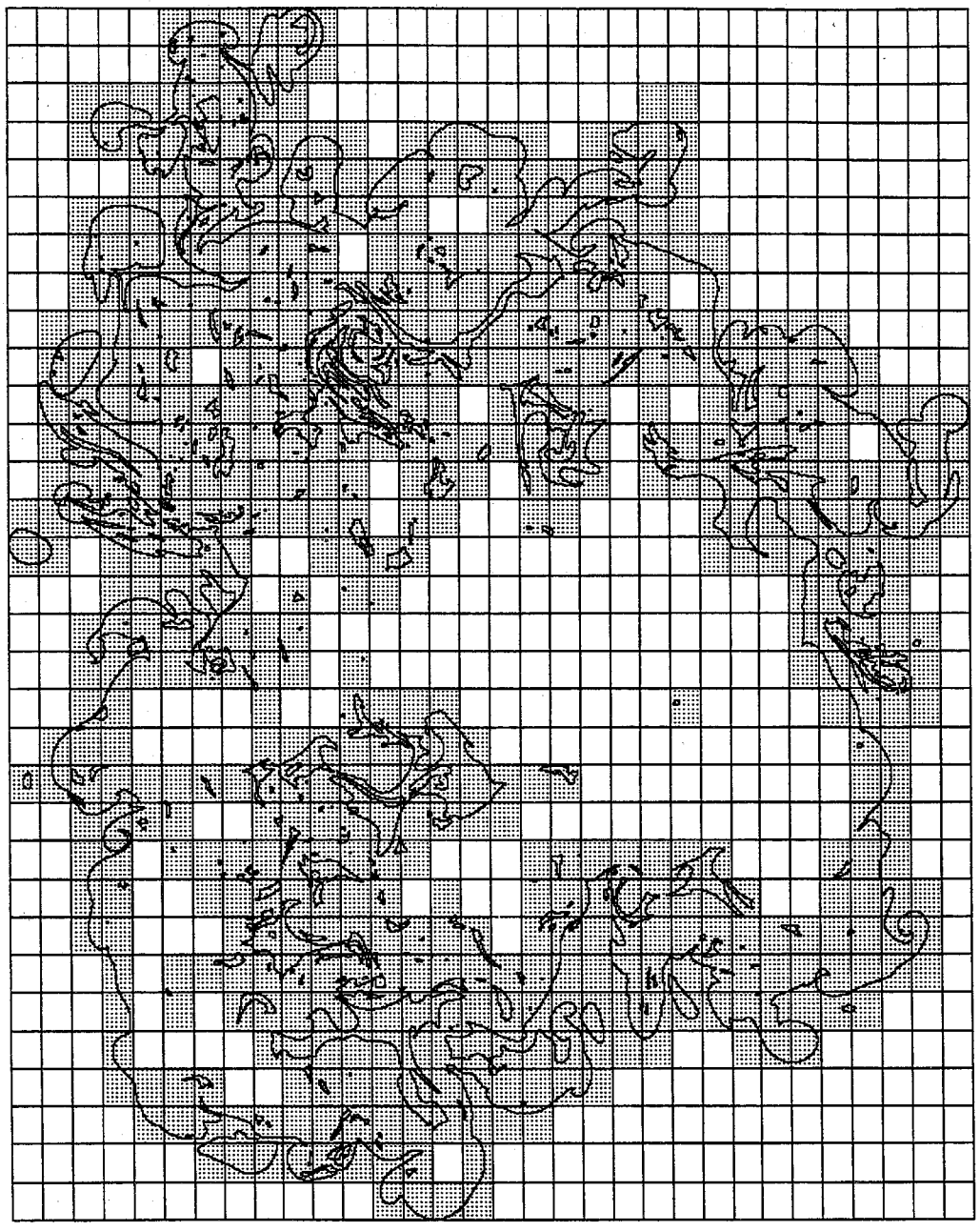

FIGURE 21 (f) $\lambda = \delta_b/32$; $N_2 = 580$, $N_{2,\mathrm{tot}} = 1024$.

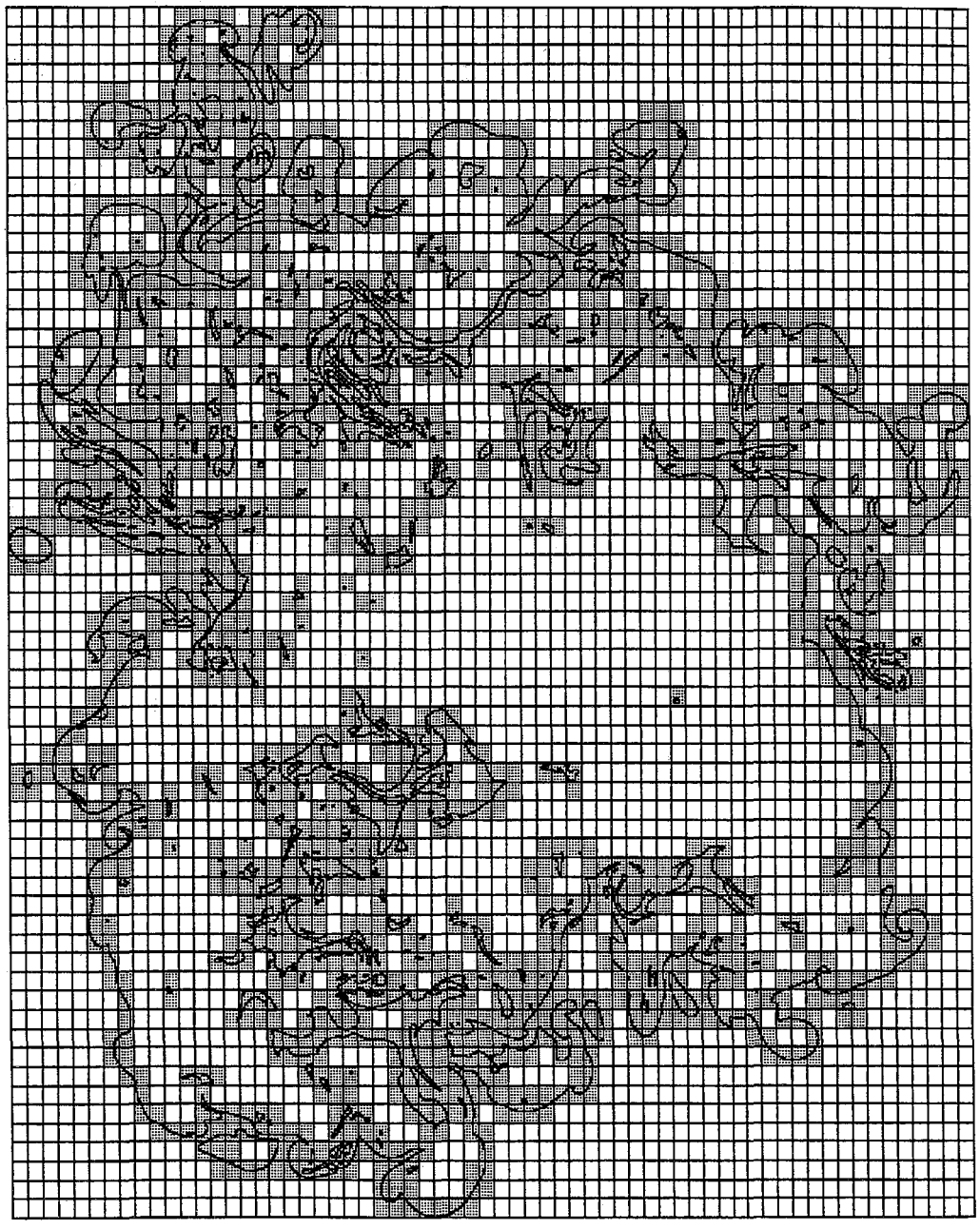

FIGURE 21 (g) $\lambda = \delta_b/64$; $N_2 = 1667$, $N_{2,\mathrm{tot}} = 4096$.

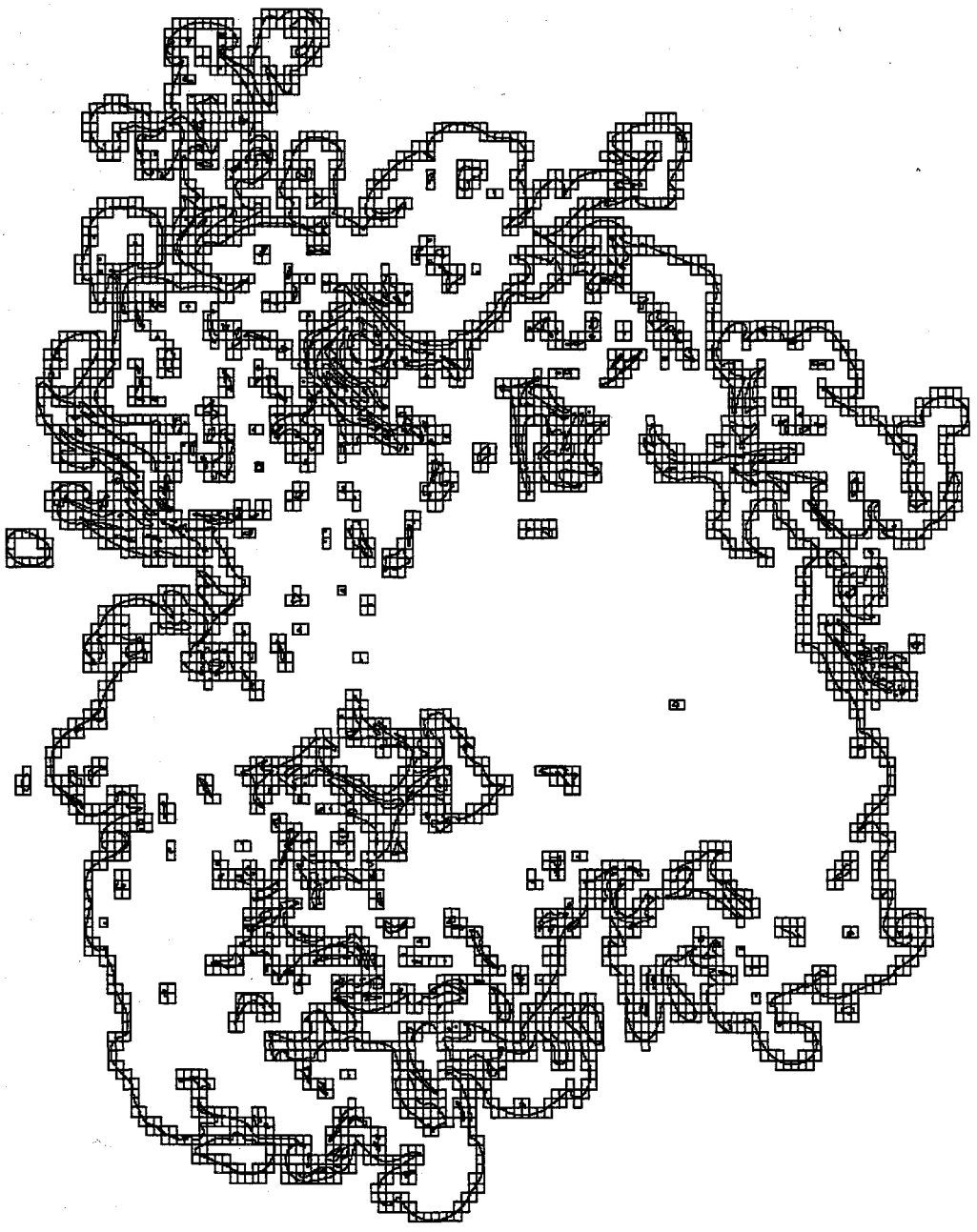

FIGURE 21 (h) $\lambda = \delta_{\rm b}/128$; $N_2 = 4363$, $N_{2,\rm tot} = 16384$.

FIGURE 21 (i) $\lambda = \delta_b/256$; $N_2 = 11238$, $N_{2,\mathrm{tot}} = 65536$.

5.2 Coverage

Figure 22 shows the ensemble-averaged, two-dimensional coverage count, $N_2(\lambda)$, of isoscalar surfaces for $Re \simeq 9.0 \times 10^3$. Coverage counts are plotted for three thresholds, c_1, c_2, and c_3 (*cf.* indicated values in figure 8), with lines of increasing solidity denoting increasing scalar threshold. The points joined by straight-line segments in figure 22 correspond to the coverage counts computed at the indicated λ-scales of the partitioned bounding-box (*cf.* Appendix A). Six images were used to estimate this statistic; the error bars (standard deviation of the mean count) are smaller than the size of the symbols employed in the plot of figure 22 (*cf.* figure A.7 in Appendix A). The spatial scale, λ, is normalized by $\delta_b(c; Re)$, the ensemble-averaged, threshold-dependent bounding-box size (*cf.* figures 13, 14, and related discussion). The coverage counts for the intermediate threshold, $c = c_2$, are seen to be larger than for $c = c_1$, or $c = c_3$, in accord with the scalar pdf behavior at this Reynolds number (*cf.* figure 8).

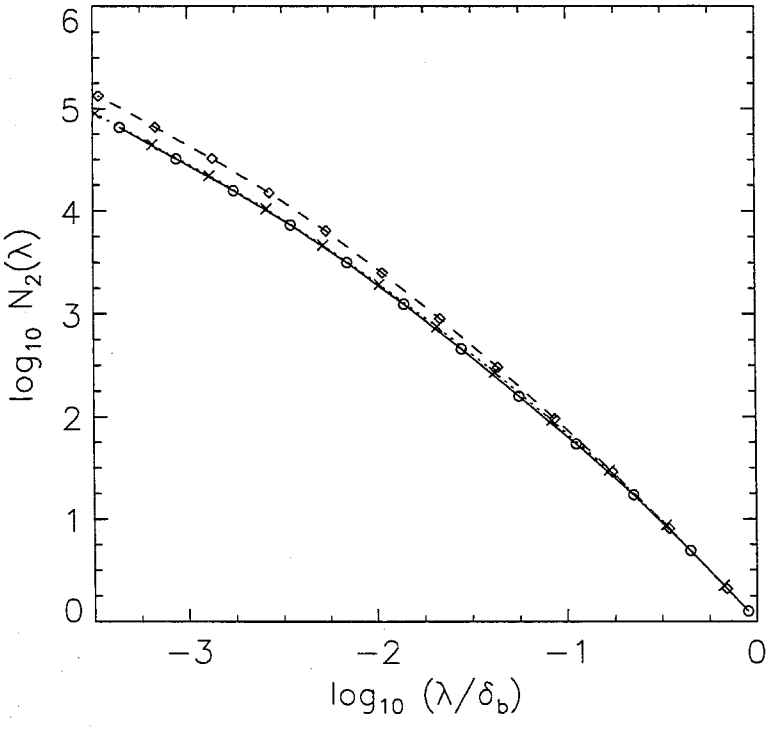

FIGURE 22 Coverage, $N_2(\lambda)$, of isoscalar surfaces at $Re \simeq 9.0 \times 10^3$. $c = c_1$: dotted line, crosses; $c = c_2$: dashed line, diamonds; $c = c_3$: solid line, circles. Recall (*cf.* figure 14) that $\delta_b = \delta_b(c; Re)$.

5.3 Coverage length

Figure 23 shows the ensemble-averaged coverage-length, $L_2(\lambda)$, normalized by the bounding-box size, δ_b, of isoscalar contours for $Re \simeq 9.0 \times 10^3$. The coverage-length, $L_2(\lambda)$, defined in terms of the coverage in equation (3.18), will, in general, be different from (larger than) the arc-length of the (smooth) contours (*cf.* figure A.2 in Appendix A). This geometric measure of the contours, with units of length, is seen to increase in a non-linear fashion with decreasing scale, in logarithmic coordinates; *cf.* equations (3.1) and (3.19). The (normalized) coverage-length is seen to be larger for the intermediate threshold, c_2, in accord with the pdf behavior of scalar values, at this Reynolds number (*cf.* figure 8). For the intermediate threshold, the small-scale limit of the coverage-length, *cf.* (3.20), is approximately equal to $L_2(\lambda \rightarrow 0)/\delta_b \simeq 45$ (*cf.* figure 23), or normalized by the perimeter of a square δ_b-box, $L_2(\lambda \rightarrow 0)/(4\delta_b) \approx 11$. In other words, the turbulent-mixing process generates isoscalar contours with a small-scale coverage-length, approximately 11 times longer than that of the perimeter of the bounding-box, at this scalar threshold and Reynolds number.

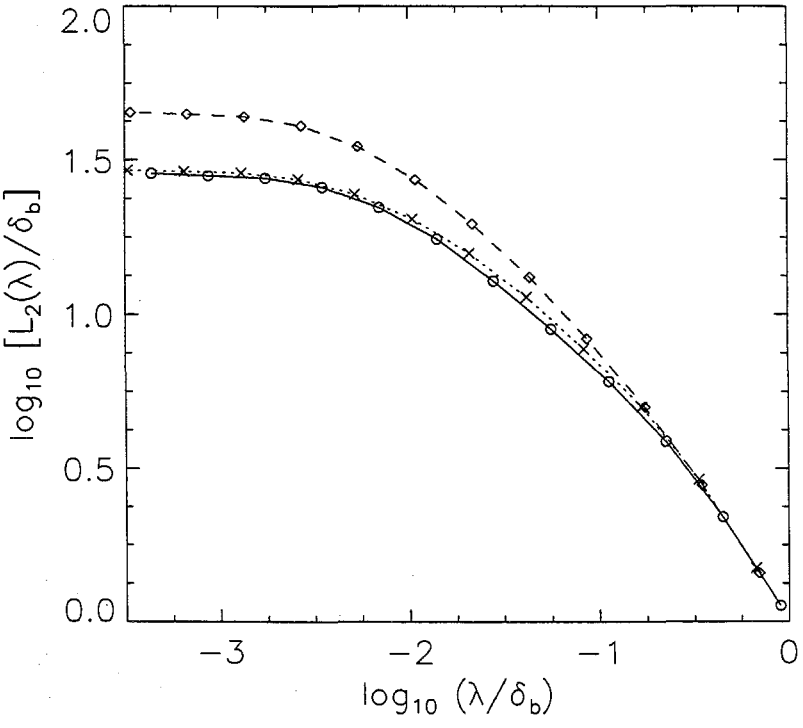

FIGURE 23 Normalized coverage-length, $L_2(\lambda)/\delta_b(c)$, at $Re \simeq 9.0 \times 10^3$. Line/symbol legend as in figure 22.

5.4 Coverage fraction

A plot of the coverage fraction, $F_2(\lambda)$, or volume-fill fraction (area-fraction in 2-D), computed from the coverage counts of figure 22 using equation (3.22), is shown in figure 24. The coverage fraction is a normalized coverage count that is independent of the bounding-box size, $\delta_b(c; Re)$. It can be seen to increase in a non-linear fashion with increasing (logarithmic) scale; *cf.* equations (3.24) and (3.26). Its large-scale behavior reflects the highest volume-fill fraction, with $F_2(\lambda \to \delta_b) \to 1$, as required. The asymptotic behavior at the smallest scales corresponds to the lowest volume-fill fraction, *i.e.*, $F_2(\lambda) \sim \lambda \to 0$, as $\lambda/\delta_b \to 0$, as expected for curves (one-dimensional objects) in a two-dimensional space; *cf.* (3.25) and related discussion. The coverage fraction is largest at $c = c_2$, *i.e.*, near the threshold corresponding to the peak of the scalar pdf (*cf.* figure 8).

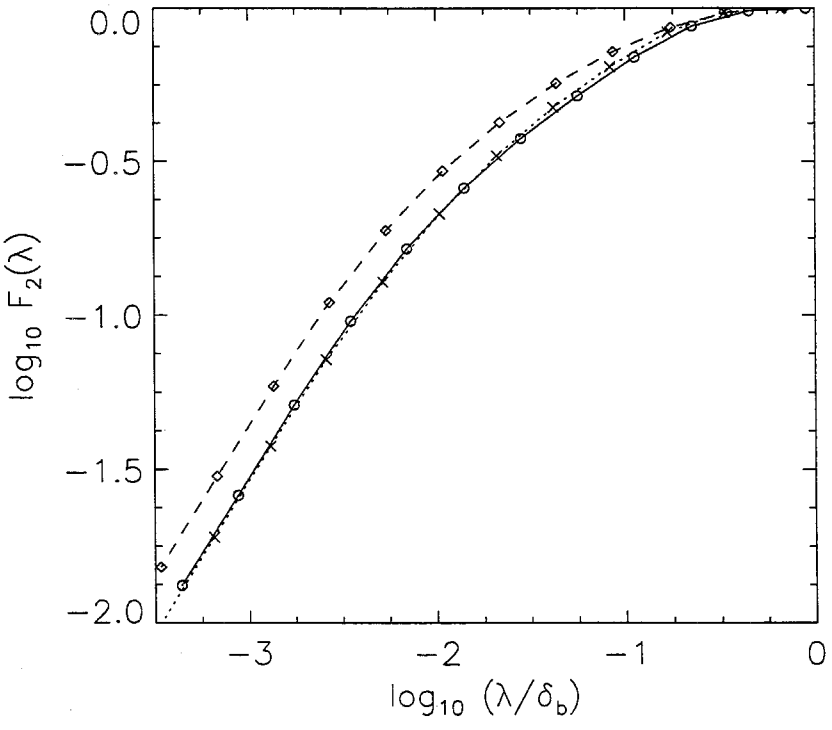

FIGURE 24 Coverage fraction, $F_2(\lambda)$, of isoscalar surfaces at $Re \simeq 9.0 \times 10^3$ (*cf.* figure 22). Line/symbol legend as in figure 22.

5.5 SDF dimension

The SDF dimension, $D_2(\lambda)$, computed from the data in figure 22, using 2nd order finite differences, is shown in figure 25; *cf.* equation (3.9). Error bars for this measure are given in figure A.8 (Appendix A). The spatial scale, λ, is, again, normalized by the ensemble-averaged (threshold-dependent) bounding-box size, $\delta_b(c; Re)$. The threshold dependence of the SDF dimension reflects the scalar pdf behavior at this Reynolds number (*cf.* figure 8), with $D_2(\lambda)$ largest, over most of the scale range, at the intermediate threshold, c_2. It is seen that the dimension is a function of scale and, in particular, not a constant. It is found to increase monotonically and continuously with scale, from near unity, at the smallest scales, to 2, at the largest scales, *i.e.*,

$$\frac{\mathrm{d}D_2(\lambda)}{\mathrm{d}\lambda} > 0 \ , \quad \text{with,} \quad d_t = 1 < D_2(\lambda) < 2 = d \ . \tag{5.1}$$

The bounds are the topological dimension, $d_t = 1$, and the embedding dimension, $d = 2$, as expected for a monotonically-increasing SDF dimension; *cf.* (3.12) and related discussion.

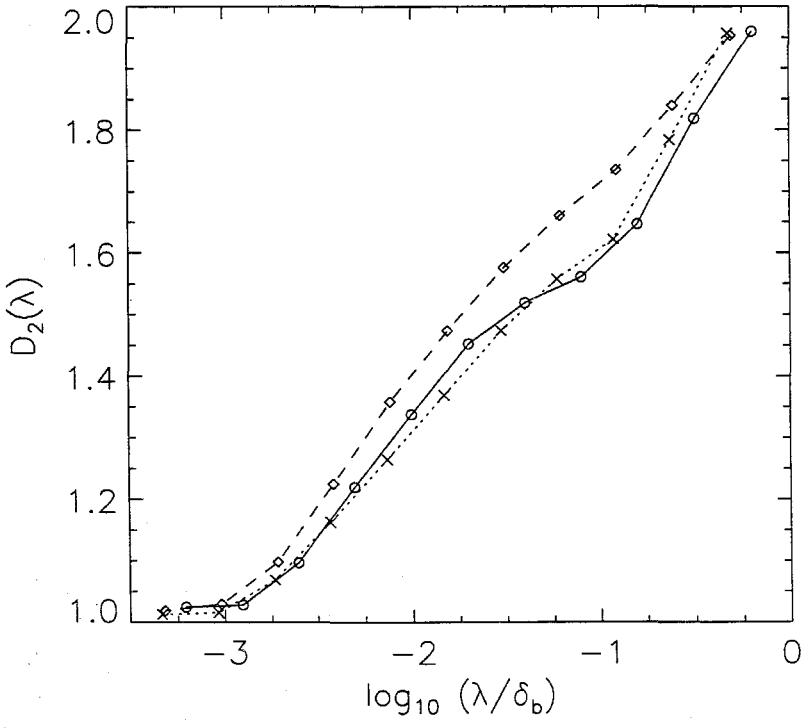

FIGURE 25 SDF dimension, $D_2(\lambda)$, of isoscalar surfaces at $Re \simeq 9.0 \times 10^3$ (*cf.* figure 22). Line/symbol legend as in figure 22.

5.6 Distribution of LEB scales

Figure 26 depicts the probability density function of LEB scales, $f_2(\lambda)$, at $Re \simeq 9.0 \times 10^3$, for three scalar thresholds, computed using equation (4.49). This is a normalized probability density function, over the range of scales; *cf.* (4.50) and related discussion. For a given threshold, $f_2(\lambda)$ is seen to be larger at smaller scales, approaching a constant value at the smallest scales, as expected for level sets consisting of lines in a plane, *i.e.*, for geometric sets with $d_t = d - 1$; *cf.* (4.53) and related discussion. The data indicate a higher probability density of LEB scales, at small scales, for the c_2 threshold corresponding to the neighborhood of the peak of the scalar pdf. Recall that the small-scale limit, $f_2(\lambda \to 0)$, is a measure of the surface-to-volume ratio (perimeter-to-area ratio in 2-D) of the isosurface. The highest surface-to-volume ratio is observed at the c_2 threshold, consistent with the behavior of the coverage length, *cf.* figure 23.

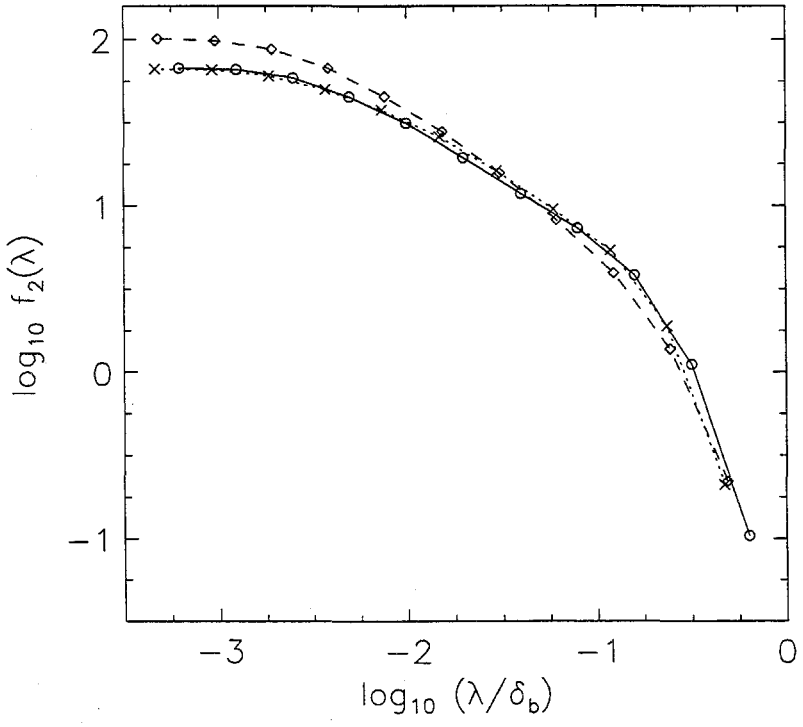

FIGURE 26 Pdf of LEB scales, $f_2(\lambda)$, for isoscalar surfaces at $Re \simeq 9.0 \times 10^3$. Line/symbol legend as in figure 22.

A further measure (that can be used to test for, *e.g.*, power-law scaling behavior of the LEB scale distribution) is the (negative of the) local slope of the LEB scale

distribution, in the coordinates of figure 26. It can be computed as the (negative of the) logarithmic derivative of the LEB scale distribution, defined as,

$$\mu(\lambda) \equiv -\frac{\mathrm{d}\log f_2(\lambda)}{\mathrm{d}\log\lambda} \ , \tag{5.2}$$

and is shown in figure 27, computed using 2nd order finite differences on the data of figure 28. It is seen that $\mu(\lambda)$ is a function of scale, throughout the complete scale range, for the threshold corresponding to the peak of the scalar pdf. Recall that a scale-dependent logarithmic derivative is not a (power-law) exponent; *cf.* discussion of equation (3.13). For threshold values away from the scalar-pdf peak location, a near power-law region is suggested over a (short) range of intermediate scales. This threshold-dependent effect arises for reasons similar to the threshold-dependence exhibited for the SDF dimension (*cf.* figure 25), namely that, away from the mean value of a fluctuating field, level sets can be expected to display characteristic scales as an artifact of the presence of near-extrema (minima or maxima) in the spatial variation of the field values (see Miller & Dimotakis 1991a).

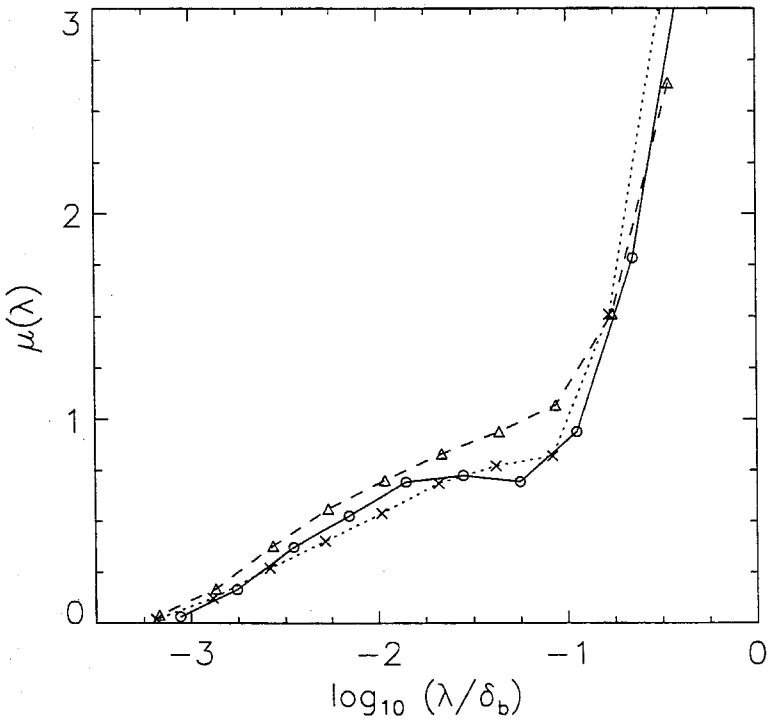

FIGURE 27 Logarithmic derivative, $\mu(\lambda)$, of LEB scale pdf for isoscalar surfaces at $Re \simeq 9.0 \times 10^3$. Line/symbol legend as in figure 22.

For all three thresholds, however, a qualitatively-similar, SDF (non-power-law) behavior of increasing value of $\mu(\lambda)$ with increasing scale is evident, for over a decade of smaller scales. This is related to the near-lognormal distribution of the size of the isoscalar islands and lakes, discussed in Chapter 6, and can be modeled, as will be described below (Section 5.8).

The pdf of the logarithm of LEB scales, $\tilde{f}_2(\log\lambda)$, offers additional interpretation of the scalar-threshold effect on the isosurface geometry. This measure is plotted in figure 28, for the same three scalar thresholds (*cf.* figure 8), at $Re \simeq 9.0\times10^3$. For a given threshold, $\tilde{f}_2(\log\lambda)$ approaches zero at the small as well as large scales, as expected; *cf.* equations (4.46) and (4.53). At the intermediate threshold, c_2, the peak of the log-LEB scale pdf shifts to smaller scales, as compared to the behavior at $c = c_1$ and $c = c_3$. In other words, it is less likely to find a largest λ-size region, at large λ's, that is not visited by the isosurfaces at this threshold. This finding is discernible in the isosurface image data directly, as can be seen in figures 10a-c.

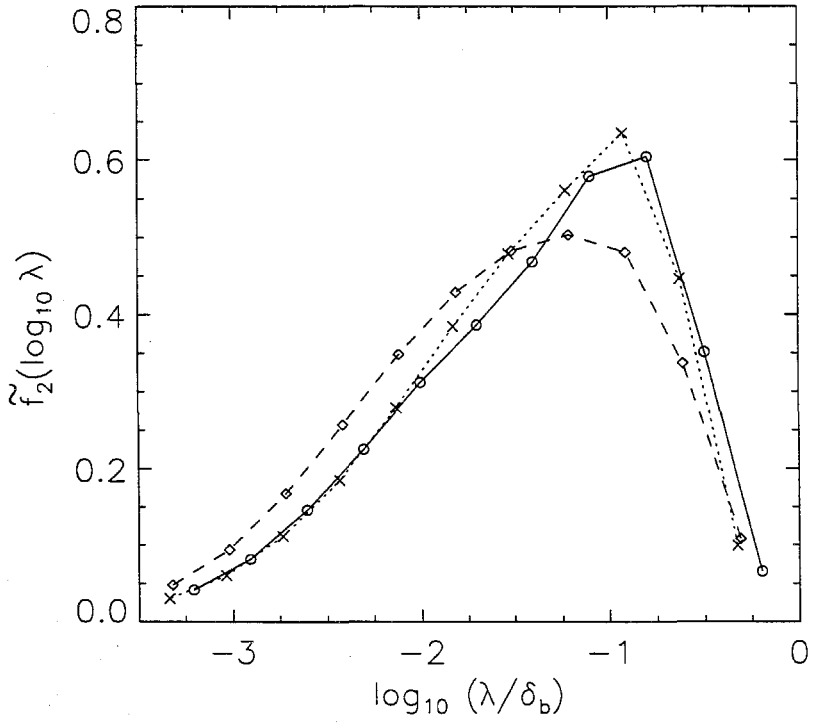

FIGURE 28 Pdf of the logarithm of LEB scales, $\tilde{f}_2(\log\lambda)$, for isoscalar surfaces at $Re \simeq 9.0\times10^3$. Line/symbol legend as in figure 22.

5.7 Reynolds number effects

These statistics allow us to investigate the Reynolds number effects on the scalar field, isosurface geometry, and scalar mixing. Figure 29 shows the *Re*-effect on the coverage length, $L_2(\lambda)$, scaled by the isoscalar bounding-box size, δ_b at the intermediate scalar threshold, c_2; lines of increasing solidity denote increasing *Re*. Recall that, at this threshold and in this *Re* range, the bounding-box size, δ_b, is approximately *Re*-independent (*cf.* figure 14 and related discussion). The data indicate that the small-scale limit, $L_2(\lambda \to 0)$, *decreases* with increasing *Re*, at this threshold. This (perhaps surprising) finding can be seen directly in the image data (*cf.* progression in figures 9b, 10b, and 11b); it can be investigated further in terms of the SDF dimension and scale distribution.

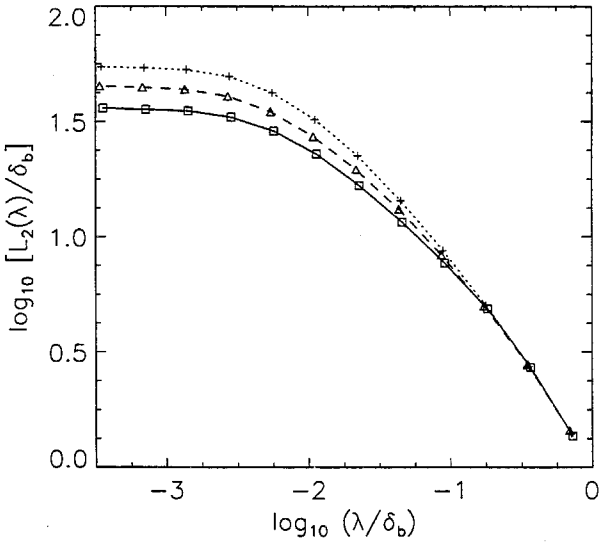

FIGURE 29 Reynolds-number dependence of coverage-length, $L_2(\lambda)/\delta_b$, at the intermediate scalar threshold, c_2. $Re \simeq 4.5 \times 10^3$: dotted line, crosses; $Re \simeq 9.0 \times 10^3$: dashed line, triangles; $Re \simeq 18 \times 10^3$: solid line, squares.

Figure 30 show the *Re*-effect on the SDF dimension. The data indicate that the SDF dimension decreases, in the range of moderate-to-large scales, as *Re* increases. At the same time, the data indicate that, at the smallest and largest scales, the SDF dimension is only weakly dependent on *Re*, if at all. The *Re* effect on the LEB scale pdf, $f_2(\lambda)$, is shown in figure 31. A systematic trend with increasing *Re* is evident. Specifically, the probability density of a LEB scale, at a given large scale, increases with *Re*. This implies that it is progressively easier to find a largest λ-size region, at large λ's, that is not visited by the isosurfaces.

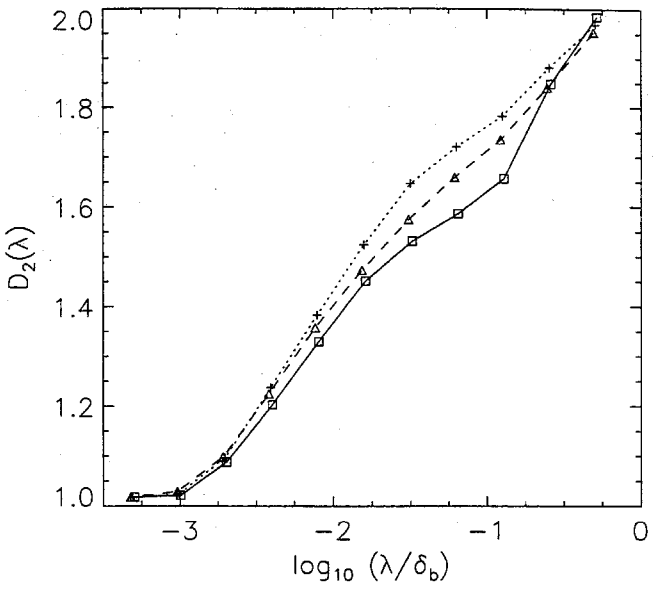

FIGURE 30 Reynolds-number dependence of SDF dimension, $D_2(\lambda)$, at the intermediate scalar threshold, c_2. Line/symbol legend as in figure 29.

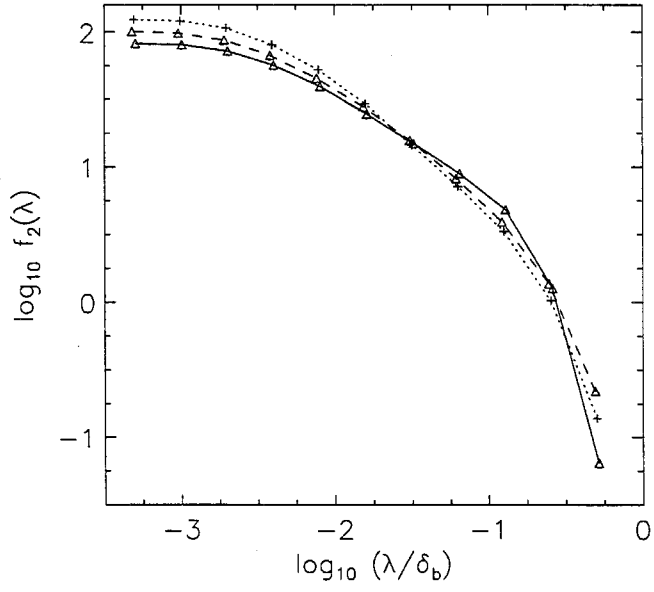

FIGURE 31 Reynolds-number dependence of LEB scale pdf, $f_2(\lambda)$, at the intermediate threshold, c_2. Line/symbol legend as in figure 29.

Figure 32 shows the *Re*-effect on the logarithmic derivative, $\mu(\lambda)$, of the LEB scale pdf; $\mu(\lambda)$ decreaseas with increasing *Re* at intermediate scales. This is consistent with the LEB-scale pdf behavior (*cf.* figure 31). Also, the small-scale behavior of $\mu(\lambda)$ is only weakly dependent on *Re*. Figure 33 depicts the *Re*-effect on the pdf

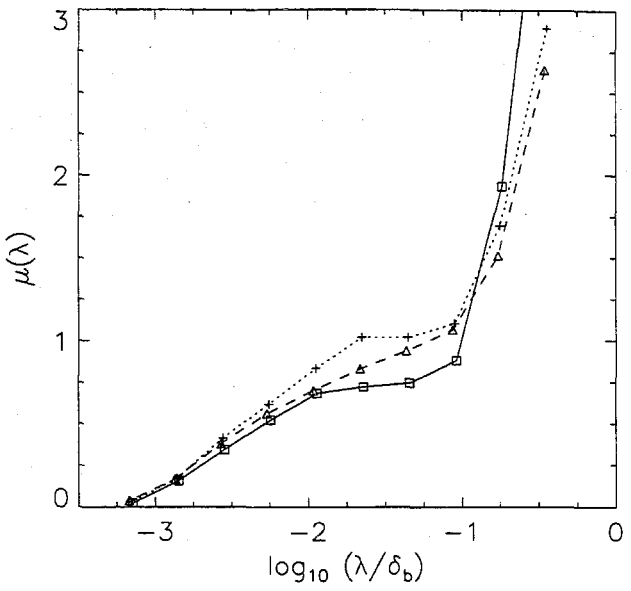

FIGURE 32 Reynolds-number dependence of logarithmic derivative, $\mu(\lambda)$, of LEB scale pdf at c_2. Line/symbol legend as in figure 29.

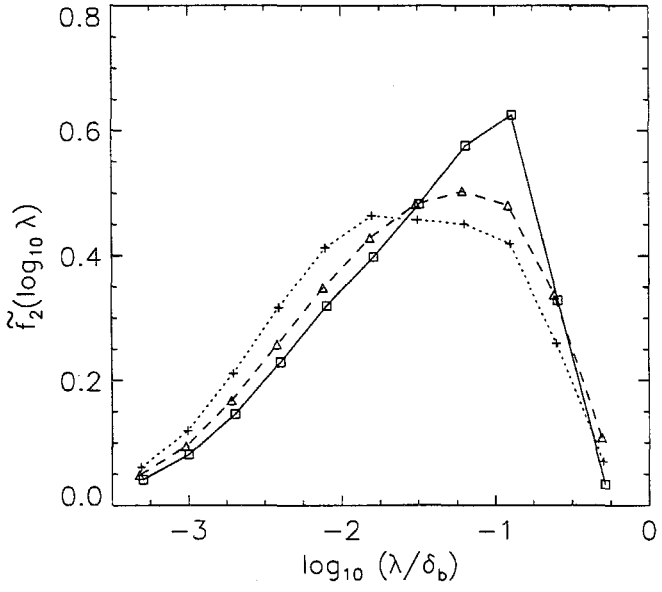

FIGURE 33 Reynolds-number dependence of pdf of logarithm of LEB scales, $\tilde{f}_2(\log\lambda)$, at c_2. Line/symbol legend as in figure 29.

of logarithmic LEB scales, $\tilde{f}_2(\log\lambda)$. A systematic Re-dependence is evident; the peak of this pdf shifts to higher LEB scales with increasing Re. In other words, it is more probable to find a largest λ-size region, at large λ's, that is not visited by the isosurface, as the Reynolds number is increased.

5.8 A model of 2-D LEB scales

As noted in chapter 4, a lognormal distribution of 1-D spacing scales has been reported in turbulent jets (Miller & Dimotakis 1991a) as well as plumes dispersing in the atmospheric surface layer (Yee *et al.* 1995). A lognormal model of 2-D LEB scales will be discussed below. While, at this point, alternative statistics might also provide reasonable fits, further evidence for a lognormal model is provided by the size distribution of isoscalar (2-D) islands/lakes, in the present measurements, which is approximately lognormal (described in chapter 6). These findings, taken collectively, suggest a lognormal model for the SDF behavior of 2-D (or higher-dimensional) measurements. The SDF dimension for a lognormal scale distribution (over all scales) is given by, *cf.* equation (4.27),

$$D_2(\lambda) = 2 - \left\{ 1 + \frac{l_m}{\lambda} \left[\frac{1 + \mathrm{erf}\left[(\ln(\lambda/l_m)/\sigma - \sigma/2)/\sqrt{2} \right]}{1 - \mathrm{erf}\left[(\ln(\lambda/l_m)/\sigma + \sigma/2)/\sqrt{2} \right]} \right] \right\}^{-1} . \qquad (5.3)$$

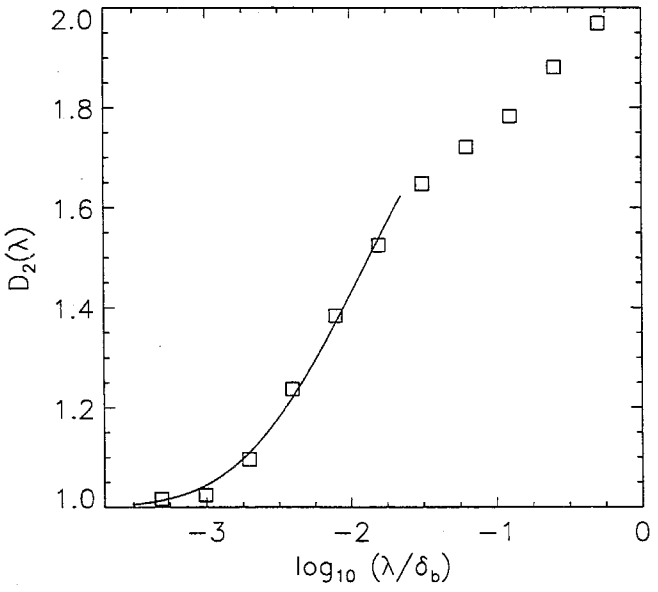

FIGURE 34 Lognormal model compared to measurements of $D_2(\lambda)$.

A comparison with the measured SDF dimension at $Re \simeq 9.0 \times 10^3$ and at a scalar threshold value c_2 is shown in figure 34. The fit (solid line), which assumes for simplicity a lognormal distribution over all scales, is only shown at the smaller scales. The behavior of the model is consistent with the data, mindful that the SDF dimension is a nonlocal statistic which couples the behavior at different scales.

The 2-D model of LEB scales corresponding to the SDF dimension of equation (5.3) can be derived using the inverse relation of equation (4.41), and is given by,

$$f_2(\lambda) \sim \text{erfc}\left[\left\{\ln(\lambda/l_{\rm m})/\sigma + \sigma/2\right\}/\sqrt{2}\right]/2l_{\rm m} \ . \qquad (5.4)$$

Note that this expression is identical to the 1-D LEB-scale distribution for lognormal spacings, and could alternatively be derived using equations (4.18) and (4.27). A fit using this model, at the smaller scales (solid line), is shown in figure 35, with $\log_{10}(l_{\rm m}/\delta_b) \simeq -1.4$ and $\sigma \simeq 1.3$; the deviation at larger scales is due to the jet topology (a single large continent, and many smaller islands/lakes) and is, therefore, a large-scale effect (*cf.* Catrakis & Dimotakis 1996a). Figure 35 shows that a 2-D model of lognormally-derived LEB scales is consistent with the data, at the smaller scales. The LEB-scale distribution is a scale-local statistic, in contrast to the SDF dimension; *cf.* figure 34.

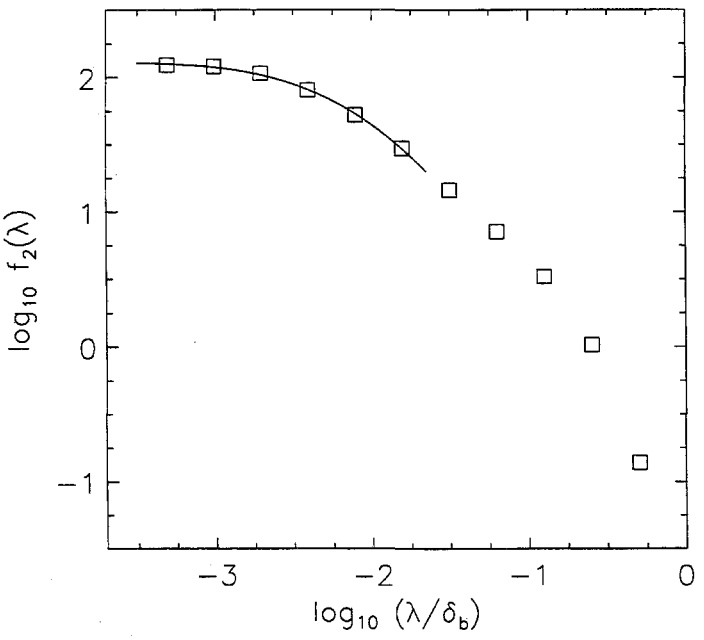

FIGURE 35 Lognormal model and measurement of LEB scale distribution, $f_2(l)$, *cf.* Fig. 34.

5.9 The multiscale nature of turbulent mixing

The above analysis suggests that the multiscale nature of turbulence can be better assessed in terms of the LEB-scale distribution, as compared to the fractal dimension. The former offers a scale-local statistic which can be used to test for geometric-scaling behavior (*i.e.*, power-law or scale-dependent). Notably, while the (smooth) curve suggested by the data in figure 35 is differentiable, *i.e.*, locally has a (straight-line) tangent at any scale, the data exhibit a (strongly) nonlinear scaling for over a decade of small scales.

The precise form of nonlinear scaling is indicated to be lognormally-derived, consistent with other statistical behavior (*e.g.*, size distribution of islands/lakes, *cf.* chapter 6). Lognormal distributions of sizes/scales can arise in fragmentation processes, in general, as noted by Kolmogorov (1941), as can agglomeration (successive-fusion) processes, *e.g.*, turbulent (stochastic) growth of clouds (Lopez 1977). The dynamics of the turbulent jet involve both fragmentation and agglomeration of eddies.

The indications of lognormally-derived isosurface-geometry statistics in jets, may well be expected to be encountered in other turbulent-mixing flows. The cascade process (fragmentation as well as agglomeration) in turbulent jets, in particular, and in turbulence, in general, at high Reynolds numbers, is expected to exhibit (universal) scaling behavior at scales away from the viscous-dominated, as well as largest, scales; *cf.* Kolmogorov (1941).

These results suggest that, in turbulent-mixing (shear) flows in general, any universal, multidimensional geometric statistics (*e.g.*, lognormally-derived LEB scales) are more likely to be encountered at the smaller scales and, additionally, are more likely to be identified through the LEB-scale distribution (as compared to the SDF dimension). Recall that the LEB-scale distribution has the additional intrerpretation that a LEB scale is a measure of the distance from a randomly-chosen point to the nearest element of the isosurface. In the context of combustion, for example, $f_2(\lambda)$ would measure the surface-to-volume (perimeter-to-area in 2-D) ratio of surfaces (contours), λ-equidistant to the burning (isoscalar) surface.

CHAPTER 6

Other measures of geometric complexity

In this chapter, additional measures of the geometric complexity (and structure) of the isosurfaces are investigated. In particular, measures based on area-perimeter properties of the individual isoscalar island/lake structures, identified from the level sets of jet-fluid concentration, are analyzed. A measure of geometric-shape complexity, Ω_d, in d-dimensions, is described in a general context, and applied to the two-dimensional measurements of the scalar isosurface geometry.

Knowledge of such measures would facilitate the description and modeling of turbulent mixing, for example, in addition to the SDF dimension or coverage fraction. In the context of chemical reactions and combustion in non-premixed hydrocarbon turbulent flames, for example, in which the combustion is largely confined to the instantaneous stoichiometric (isoscalar) surface, area-perimeter, or surface-volume, properties of the isoscalar island/lake structures would be required to relate the local burning rate to the time required for local consumption of the unburnt fuel pockets.

In a biological context, quantitative measures of the complex boundary of nephron cells, for example, would be needed to relate the water transport across the cell boundary as a function of the applied osmotic gradient (*e.g.*, Welling *et al.* 1996). In particular, complexity measures that can be connected to the surface-to-volume ratio of such boundary surfaces (or interfaces) would be of primary interest.

6.1 Isoscalar islands and lakes

The level sets of jet-fluid concentration consist of multiple, disjoint, closed, isoscalar contours of varying size and shape, as can be seen directly in figure 36, for example, depicting an isosurface at $Re \simeq 9.0 \times 10^3$ and scalar threshold $c = c_2$. In figure 36, the level set has been superimposed on the scalar field; *cf.* figure 4b. These isoscalar contours are either "islands", or "lakes", depending on whether the neighboring interior isosurfaces are at a higher, or lower, threshold, respectively. In particular, the largest island in each image realization will be referred to as the "continent". The area, A, and perimeter, P, of the islands/lakes was computed from a biquadratic B-spline representation of the level sets, described in Appendix C.

6.2 Size and shape complexity

A useful (and dimensionless) measure of the surface-to-volume ratio of complex surfaces can be defined, in general, as follows. In a d-dimensional space ($d \geq 2$), a useful measure of size of $(d-1)$-dimensional surfaces embedded is $V_d^{1/d}$, where V_d is the (hyper)volume enclosed by the surfaces. Of all surfaces of a given size, $V_d^{1/d}$, the sphere has the least surface area. For a sphere of radius R in d-dimensions, the volume is given by,

$$V_{d,\text{sphere}} = \frac{\pi^{d/2}}{\Gamma(d/2+1)} R^d \ , \tag{6.1}$$

(where Γ denotes the Gamma function) and the surface area is given by,

$$S_{d,\text{sphere}} = \frac{\mathrm{d}}{\mathrm{d}R} V_{d,\text{sphere}} = \frac{\pi^{d/2}\, d}{\Gamma(d/2+1)} R^{d-1} \ , \tag{6.2}$$

so that,

$$S_{d,\text{sphere}} = \frac{\pi^{1/2}\, d}{\Gamma^{1/d}(d/2+1)} \left(V_{d,\text{sphere}}\right)^{(d-1)/d} \ . \tag{6.3}$$

Therefore, for any (closed) surface in d-dimensions, the surface area, S_d, is bounded from below, *i.e.*,

$$S_d \geq \frac{\pi^{1/2}\, d}{\Gamma^{1/d}(d/2+1)} V_d^{(d-1)/d} \ . \tag{6.4}$$

As size increases, this lower bound for the surface area must, therefore, increase. To examine surface-to-volume (or area-to-perimeter) behavior over a range of sizes, it is useful to normalize the area of a surface by the area of an equal-sized sphere. The resulting surface-to-volume measure, denoted here by Ω_d, is a (dimensionless) measure of the complexity of the shape of the surface. It will be unity for spheres and unbounded from above, in general, *i.e.*,

$$1 \leq \Omega_d \equiv \frac{\pi^{1/2}\, d}{\Gamma^{1/d}(d/2+1)} \frac{S_d}{V_d^{(d-1)/d}} \leq \infty \ , \tag{6.5}$$

with the upper limit attainable, for example, for non-rectifiable (fractal) surfaces, *e.g.*, PLF or SDF surfaces.

For two-dimensional (closed) contours, the size is the square-root of the area enclosed by the contour, $A^{1/2}$. Let P and A denote the perimeter and enclosed area of any closed curve in a plane, respectively. Then, the two-dimensional shape complexity, Ω_2, becomes,

$$\Omega_2 \equiv \frac{P}{(4\pi A)^{1/2}} \ , \tag{6.6}$$

and is bounded from below by unity, *cf.* equation (6.5). Ω_2 is a measure of the interfacial arc length, per unit (square-root of) enclosed area.

6.3 Area and perimeter of islands and lakes

Figure 37 is a scatter-plot of the perimeter and size values of the isoscalar island/lake structures at $Re \simeq 9.0 \times 10^3$, for six image realizations (*cf.* figure 10a). Perimeter-size values for a total of 4,368 individual islands and lakes are depicted, corresponding to (an average of) 728 isoscalar islands and lakes for each image realization, at this Reynolds number. As noted above, the scalar threshold for these structures corresponds to the estimated peak of the pdf of the jet-fluid concentration at this Reynolds number. The results, however, are not particularly sensitive to this choice. The size and perimeter values in figure 37 are normalized by the ensemble-averaged, outer spatial extent, δ_b, of the scalar level set at this Reynolds number and scalar threshold. The outer scale, δ_b, is computed as the square-root of the area of the circumscribing rectangle (bounding box) for the level set. The solid boundary line in figure 37 corresponds to the minimum value of the perimeter as a function of size (*cf.* equation (6.5)), *i.e.*, for circles.

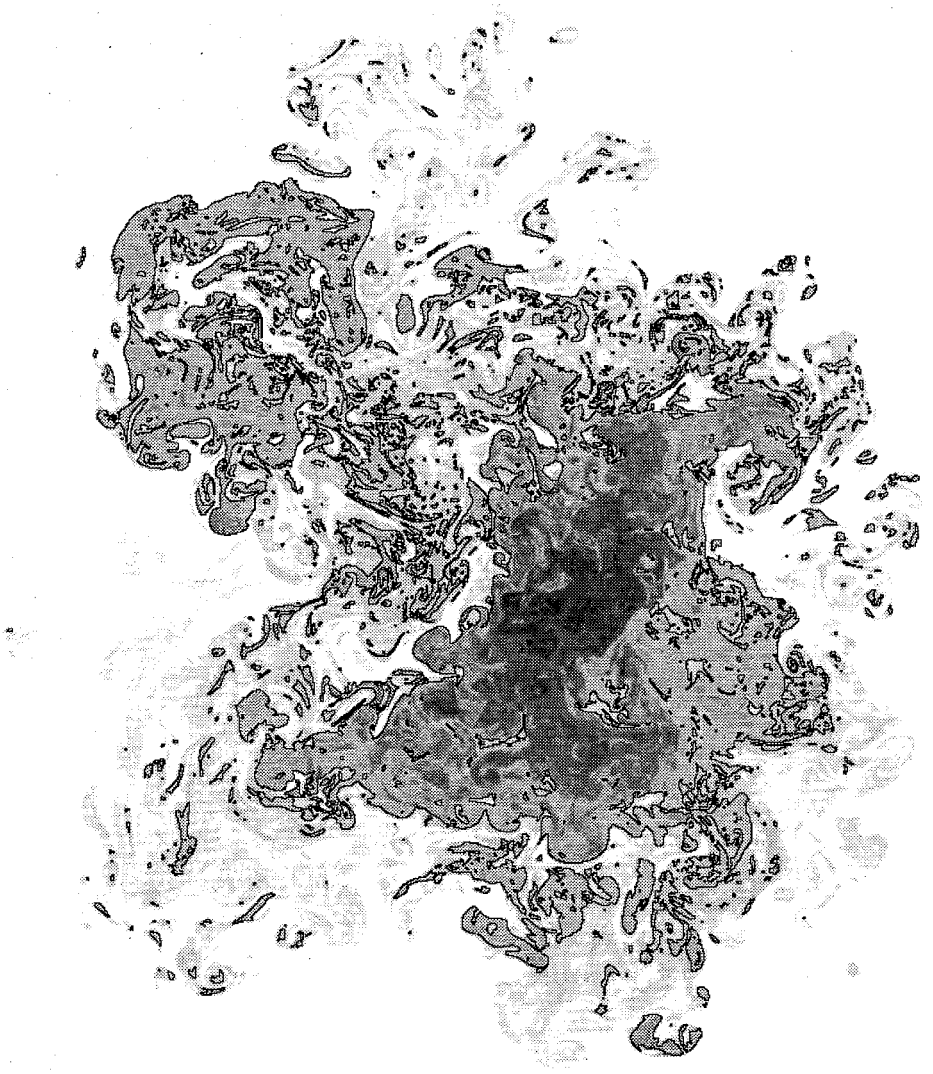

FIGURE 36 Islands, lakes, and continent of an isoscalar (level) set, at $c = c_2$ and $Re \simeq 9.0 \times 10^3$, superimposed on the scalar-field image data of figure 4b.

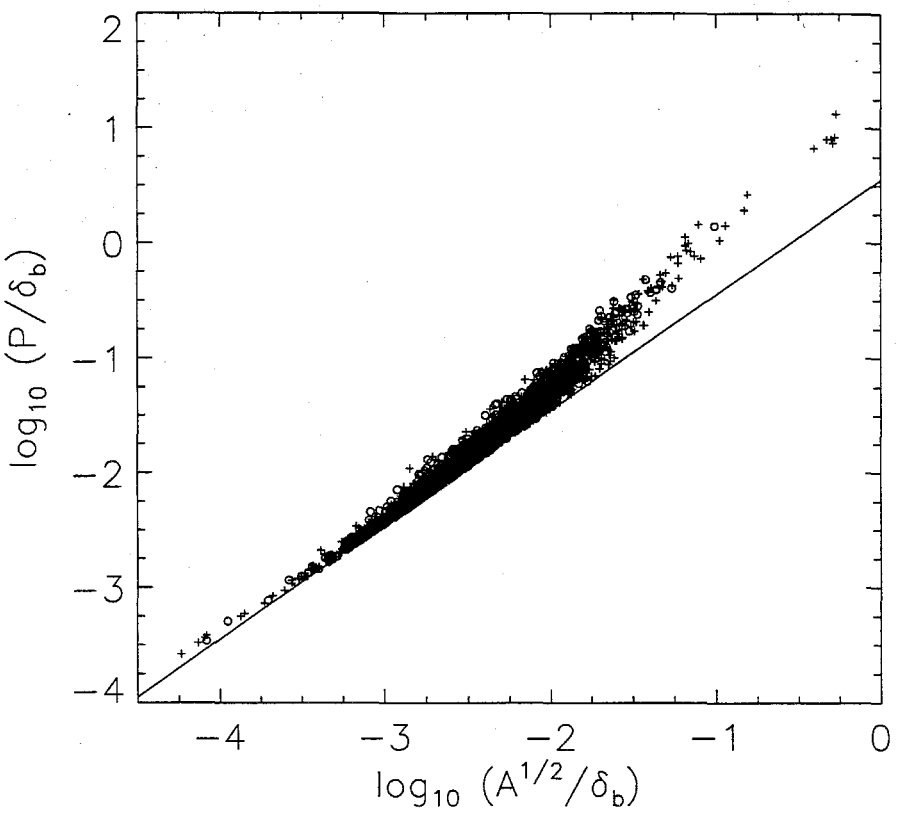

FIGURE 37 Scatter plot of perimeter, P, *vs.* size, $A^{1/2}$, of isoscalar island/lake structures at $Re \simeq 9.0 \times 10^3$ and $c = c_1$ (islands: crosses, lakes: circles).

Figure 37 shows that the islands and lakes exhibit a range of size values spanning over 3 decades. At a given size, a range of perimeter values can be found. At small sizes, the perimeter values approach the minimum possible value, while, at large sizes, the perimeter values become progressively larger. The area-perimeter behavior exhibited in figure 37 must be interpreted in light of the fact that the minimum perimeter value for any size will increase with size, in general, *cf.* equation (6.6) and related discussion. In particular, the area-perimeter behavior can be better assessed by normalizing the perimeter values by the perimeter of an equal-sized circle, *cf.* equation (6.6), as discussed below.

6.4 Size and shape complexity of islands and lakes

The size-dependent behavior of the perimeter is more evident in figure 38, which is a scatter plot of geometric-shape complexity, Ω_2, and size, $A^{1/2}$, for the isoscalar islands/lakes in figure 37. Shape-complexity as well as size values (and, therefore, perimeter and area values) are seen to be distributed. In other words, a given size can be associated with a range of shape complexity. Equivalently, different sizes are encountered possessing the same shape complexity. In particular, over most of the Ω_2-range, island/lake structures are found spanning a size- (area-) range of more than one (two) decade(s), for a given shape complexity.

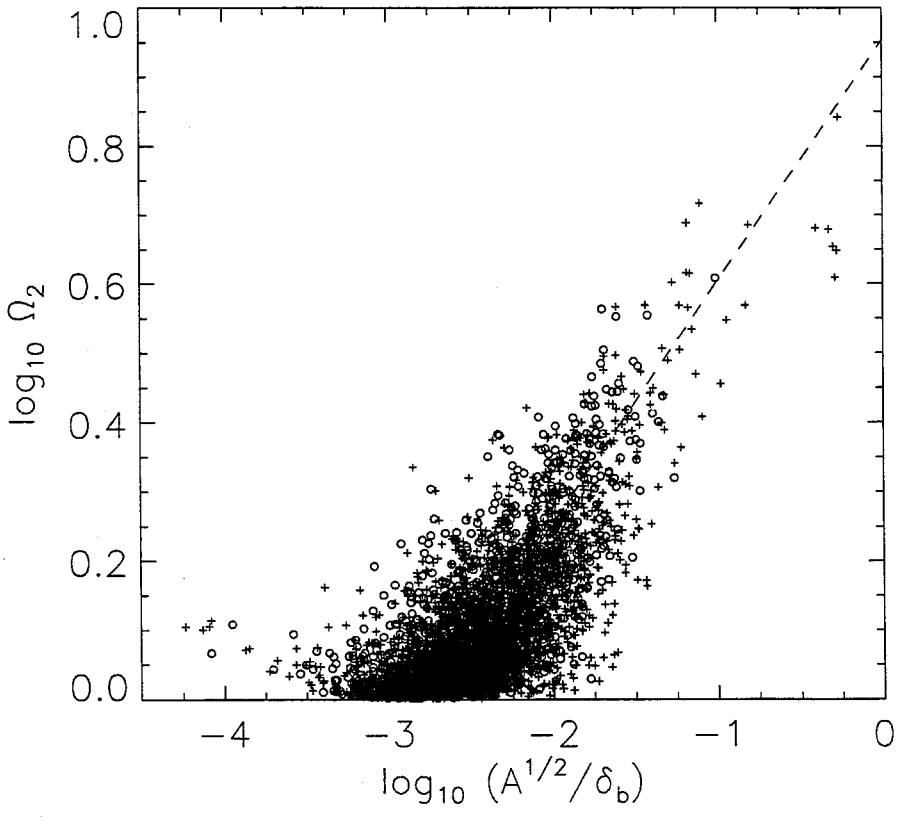

FIGURE 38 Scatter plot of geometric-shape complexity, Ω_2, *vs.* size, $A^{1/2}$, of isoscalar island/lake structures at $Re \simeq 9.0 \times 10^3$ (islands: crosses, lakes: circles).

This conclusion, of a (joint) size and shape-complexity distribution, is at variance with previously-proposed, PLF, perimeter-area relations (*e.g.*, Lovejoy 1982, Mandelbrot 1983), *i.e.*, the present data indicate that,

$$P \not\propto A^{D_2/2} \ , \qquad \text{or,} \qquad \frac{P}{\lambda_0} \neq \text{const.} \left(\frac{A}{\lambda_0^2} \right)^{D_2/2} \ , \tag{6.7}$$

where D_2 would be the PLF dimension of the (2-D) level set. A scaling length, λ_0, has been added here for dimensional reasons. A direct comparison with a PLF proposal is made in figure 38, where the dashed line indicates a power law for the shape complexity as a function of size. In other words, for the present data,

$$\Omega_2 \not\propto \left(\frac{A^{1/2}}{\delta_b} \right)^{D_2 - 1} \ , \tag{6.8}$$

for $D_2 = 1.35$, which is a value reported, for example, in Lovejoy 1982.

The data of figure 38 are not described by a power-law area-perimeter behavior, and, additionally, do not admit a one-to-one area-perimeter relation. The present data analysis indicates that, at least in the case of turbulent jets, isoscalar islands and lakes possess a *joint distribution of size and shape complexity*, $p_{A,\Omega}\left(A^{1/2}/\delta_b \, , \, \Omega_2\right)$, which may be expected in other turbulent-mixing flows, in particular, and in other complex phenomena, in general. The joint pdf is normalized such that,

$$\int_1^\infty \int_0^1 p_{A,\Omega} \left(\frac{A^{1/2}}{\delta_b} \, , \, \Omega_2 \right) \mathrm{d} \left(\frac{A^{1/2}}{\delta_b} \right) \mathrm{d}\Omega_2 \ = \ 1 \ . \tag{6.9}$$

The range of Ω_2-values is seen to increase with increasing size (*cf.* figure 38).

6.5 Size distribution

The ensemble-averaged number of isoscalar islands/lakes with size greater than a given value, $N_A(A^{1/2}/\delta_b)$, is shown in figure 39, derived from the same area-perimeter data as for figures 37 and 38. This statistic is known as a Korčak plot (Korčak 1938). A smooth variation of the (local) slope is evident, as a function of the (logarithm of) size. This is at variance with PLF, Korčak, number-size proposals (*e.g.*, Korcak 1938, Mandelbrot 1983).

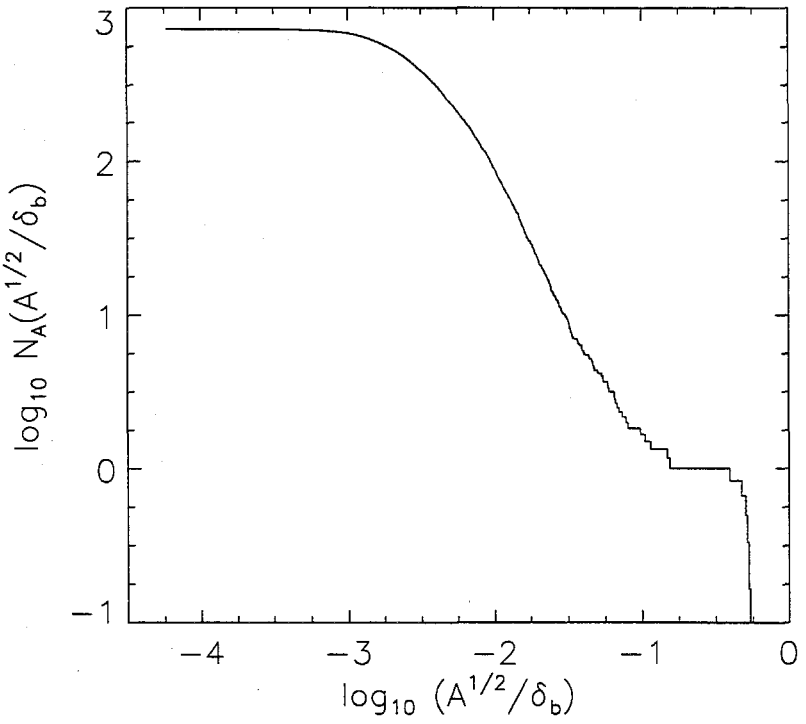

FIGURE 39 Cumulative (ensemble-averaged) count of size, $A^{1/2}$, of islands/lakes.

The Korčak (cumulative) distribution of size depicted in figure 39 can be converted to the corresponding pdf of size, $p_A(A^{1/2}/\delta_b)$, depicted in figure 40 for the data of figure 39. This pdf is given, in terms of the joint pdf of size and shape complexity, by,

$$p_A(A^{1/2}/\delta_b) \equiv \int_1^\infty p_{A,\Omega}\left(\frac{A^{1/2}}{\delta_b}, \Omega_2\right) \mathrm{d}\Omega_2 \ , \tag{6.10}$$

cf. equation (6.9), and,

$$p_A(A^{1/2}/\delta_b)\,\mathrm{d}(A^{1/2}/\delta_b) \ = \ -\,\mathrm{d}N_A(A^{1/2}/\delta_b) \ . \tag{6.11}$$

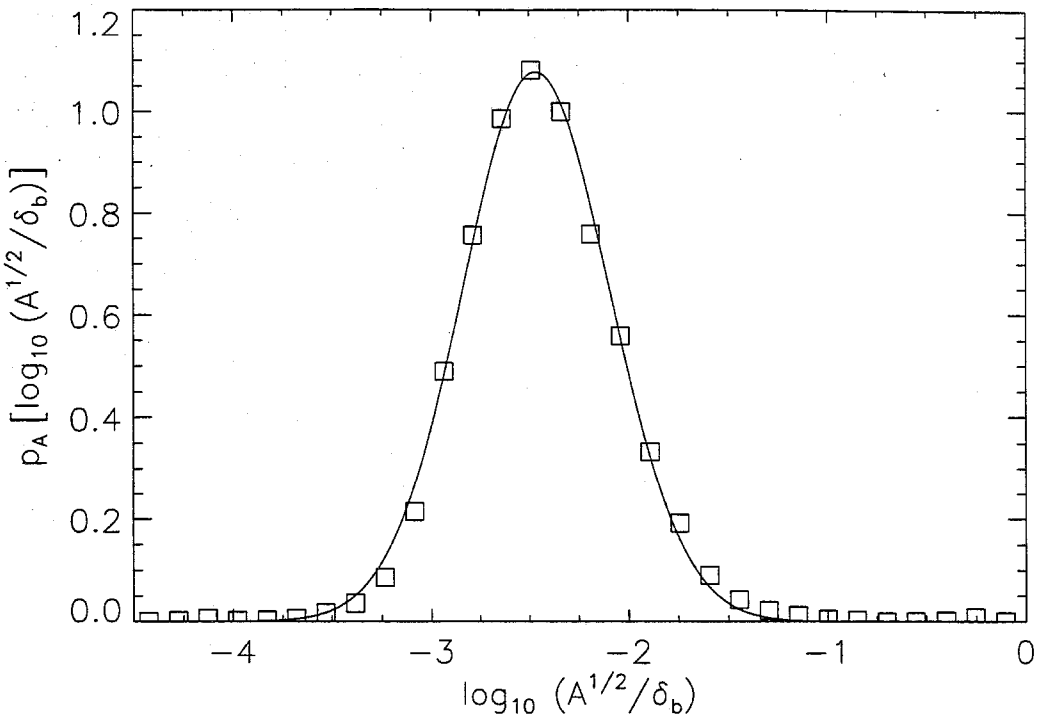

FIGURE 40 Probability density function of size, $A^{1/2}$, of isoscalar islands/lakes. Solid curve: Gaussian fit (in these coordinates).

A Gaussian fit (in these coordinates) of the data is included in figure 40. The quality of the fit indicates that a lognormal distribution provides a useful description of isoscalar island/lake sizes over the size range exhibited by the data, *i.e.*,

$$p_A(A^{1/2}/\delta_b) \simeq \frac{1}{\sigma\sqrt{2\pi}A^{1/2}/\delta_b}\,10^{-\frac{1}{2\sigma^2}\left[\log_{10}\left(\frac{A^{1/2}}{\delta_b}\right)-\mu\right]^2} \tag{6.12}$$

with an estimated mean of $\mu \simeq -2.5$ and a standard deviation of $\sigma \simeq 0.37$, in these coordinates. This finding is in accord with measurements of the (horizontal) size of clouds and radar-echo regions, for which a lognormal distribution was found in a variety of atmospheric conditions (*70*). Also consistent with these results are the findings of lognormal distributions of level-crossing (spacing) scales derived from 1-D scalar measurements in liquid-phase turbulent jets (Miller & Dimotakis 1991a) and in plumes in the atmospheric surface layer (Yee *et al.* 1995).

6.6 Distribution of shape complexity

The ensemble-averaged number of islands/lakes with geometric-shape complexity greater than Ω_2, $N_\Omega(\Omega_2)$, is plotted in figure 41. This cumulative count decreases continuously with increasing Ω_2, from the smallest values, $\Omega_2 = 1$, throughout the range of shape complexity. In other words, the cumulative count does not display plateaus at small or large values of Ω_2, in contrast to the behavior of the cumulative statistics for the size, *cf.* figure 39. The Ω_2 values range over almost one decade, *i.e.*, isoscalar islands/lakes were found with up to a factor of ten times the value of perimeter per unit (root) area enclosed, than for circles.

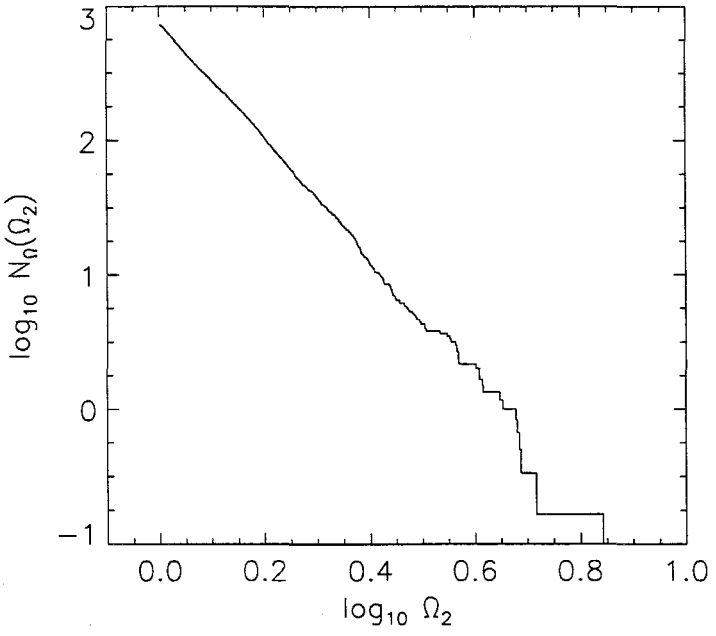

FIGURE 41 Cumulative (ensemble-averaged) count of geometric-shape complexity, Ω_2, of isoscalar islands/lakes.

The corresponding pdf of shape complexity, *i.e.*,

$$p_\Omega(\Omega_2)\,\mathrm{d}\Omega_2 \;=\; -\,\mathrm{d}N_\Omega(\Omega_2)\;, \tag{6.13}$$

or,

$$p_\Omega(\Omega_2) \;\equiv\; \int_0^1 p_{A,\Omega}\left(\frac{A^{1/2}}{\delta_\mathrm{b}}\,,\,\Omega_2\right)\mathrm{d}\left(\frac{A^{1/2}}{\delta_\mathrm{b}}\right)\;, \tag{6.14}$$

is shown in figure 42. An approximate power-law distribution of complexity is suggested from the data, as indicated by the fitted solid line in figure 42, *i.e.*,

$$p_\Omega(\Omega_2) \;\sim\; \Omega_2^{-\alpha}\;, \tag{6.15}$$

with $\alpha \simeq 5.3$ (*cf.* equation (6.13)).

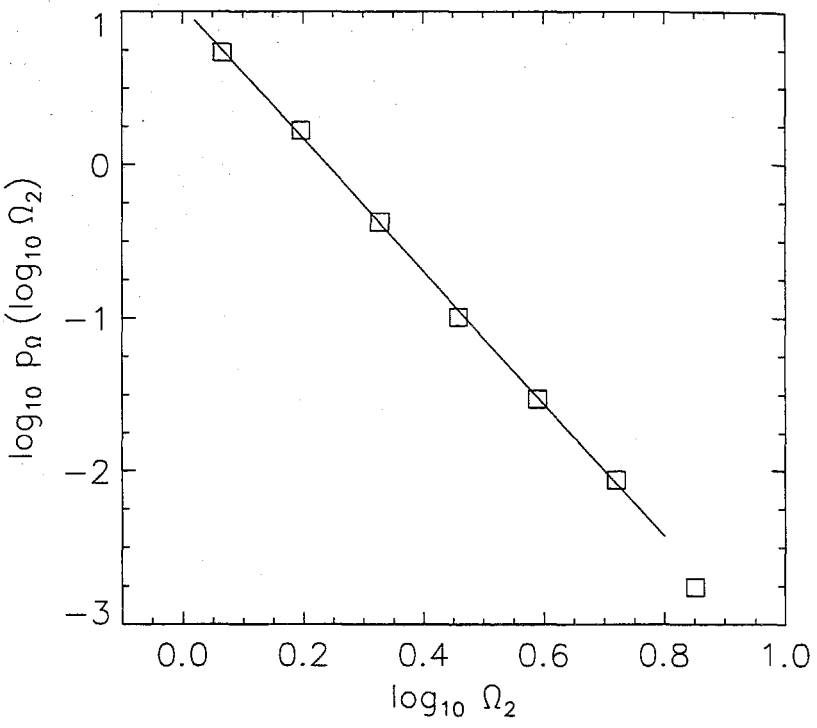

FIGURE 42 Probability density function of geometric-shape complexity, Ω_2, of isoscalar islands/lakes. Solid line: power-law fit (in these coordinates).

The pdf of shape complexity, therefore, decreases with increasing shape complexity, in an approximate power-law fashion. In particular, near-circular structures, which generally correspond to small sizes (*cf.* figure 38), are associated with the highest shape-complexity probability density. Note that in terms of the pdf of the logarithm of the shape complexity, *i.e.*, $\tilde{p}_\Omega(\log_{10}\Omega_2) \equiv \Omega_2\, p_\Omega(\Omega_2)$, relation (6.15) is equivalent to,

$$\tilde{p}_\Omega(\log_{10}\Omega_2) \;\sim\; \exp\left[-(\alpha-1)\log_{10}\Omega_2\right] \;, \tag{6.16}$$

which is a Poisson distribution for the logarithm of Ω_2 (as noted by Dimotakis, in discussions). In other words, a power-law distribution of shape complexity is equivalent to log-Poisson statistics.

6.7 Total perimeter, size, and shape complexity

Consider the total perimeter, $P_{\rm tot}$,

$$P_{\rm tot} \equiv \sum_{i=1}^{n_{\rm isl}} P_{\rm isl}^{(i)} + \sum_{i=1}^{n_{\rm lak}} P_{\rm lak}^{(i)} , \tag{6.17}$$

and the (net) enclosed area, $A_{\rm tot}$, of the isoscalar islands and lakes,

$$A_{\rm tot} \equiv \sum_{i=1}^{n_{\rm isl}} A_{\rm isl}^{(i)} - \sum_{i=1}^{n_{\rm lak}} A_{\rm lak}^{(i)} , \tag{6.18}$$

where $P_{\rm isl}^{(i)}$, $P_{\rm lak}^{(i)}$, $A_{\rm isl}^{(i)}$, and $A_{\rm lak}^{(i)}$ denote the perimeter/area values of the ith island/lake, respectively. Note, therefore, that the presence of lakes increases the total isoscalar arc-length while, at the same time, decreasing the net area enclosed by the level set.

A practically useful measure is the total shape complexity, $\langle \Omega_2 \rangle$. In analogy with equation (Eq. 6.6), this can be defined as,

$$\langle \Omega_2 \rangle \equiv \frac{P_{\rm tot}}{\left(4\pi A_{\rm tot}\right)^{1/2}} . \tag{6.19}$$

The total shape complexity can be expressed as a weighted sum of the shape complexities of the individual islands and lakes, *i.e.*,

$$\langle \Omega_2 \rangle = \frac{\sum_{i=1}^{n_{\rm isl}} \Omega_{2,{\rm isl}}^{(i)} \sqrt{A_{\rm isl}^{(i)}} + \sum_{i=1}^{n_{\rm lak}} \Omega_{2,{\rm lak}}^{(i)} \sqrt{A_{\rm lak}^{(i)}}}{\sqrt{\sum_{i=1}^{n_{\rm isl}} A_{\rm isl}^{(i)}} - \sqrt{\sum_{i=1}^{n_{\rm lak}} A_{\rm lak}^{(i)}}} , \tag{6.20}$$

where the individual shape complexities are denoted by $\Omega_{2,{\rm isl}}^{(i)} \equiv P_{\rm isl}^{(i)} / \left(4\pi A_{\rm isl}^{i}\right)^{1/2}$ and $\Omega_{2,{\rm lak}}^{(i)} \equiv P_{\rm lak}^{(i)} / \left(4\pi A_{\rm lak}^{i}\right)^{1/2}$.

This total-shape-complexity measure represents the ratio of the (total) isoscalar interfacial length, to the (square-root of the) total area of the scalar-field cross-section where jet fluid has not yet mixed down to the isoscalar threshold. In the context of non-premixed jet hydrocarbon combustion, for example, this $\langle \Omega_2 \rangle$ measure, evaluated at a threshold chosen to coincide with the stoichiometric fuel-to-air mixture fraction, would become the perimeter-to-(root-)area ratio of the burning, isoscalar interface.

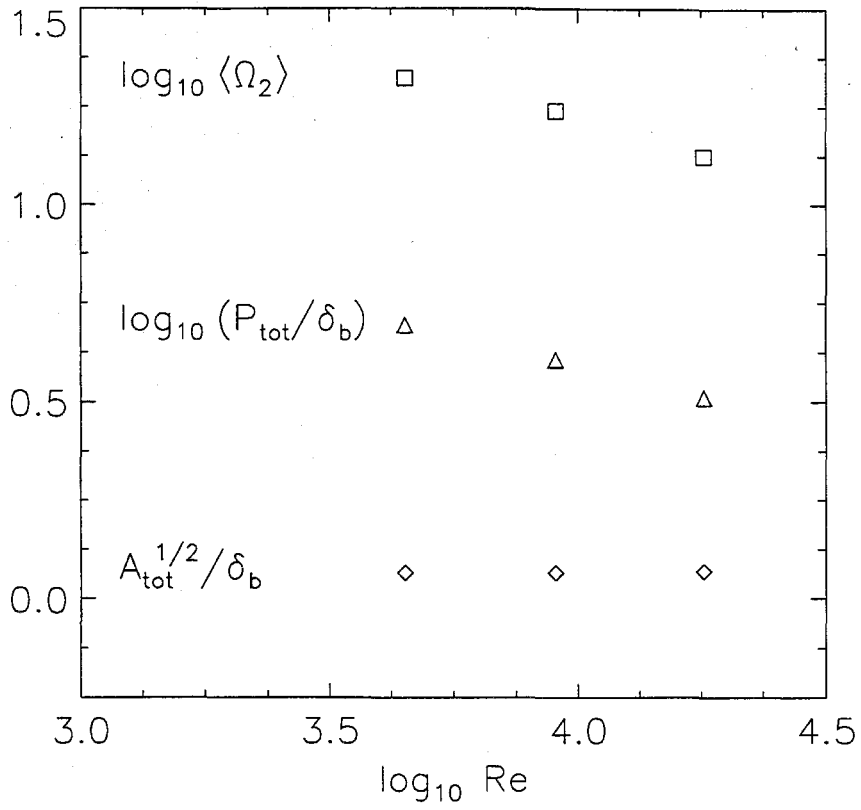

FIGURE 43 Reynolds-number dependence of total shape complexity, $\langle\Omega_2\rangle$, perimeter, $P_{\rm tot}$, and size, $A_{\rm tot}$, at a scalar threshold near the peak of the pre-mixing-transition scalar pdfs.

The ensemble-averaged total shape complexity, $\langle\Omega_2\rangle$, computed as a function of Reynolds number in the range $4.5\times10^3 \leq Re \leq 18\times10^3$, at the c_2 scalar threshold, corresponding to the peak of the pre-mixing-transition scalar pdf, is depicted in figure 43, as is the total perimeter, $P_{\rm tot}$, and total size $A_{\rm tot}$. The decrease, with increasing Reynolds number, of the total shape complexity is seen to be due to the decreasing total perimeter; the total size is only weakly dependent on Reynolds number, in this range. These observations are consistent with the behavior of scalar-field and isosurface measures observed in this Reynolds number range (*cf.* chapters 2 and 4), and indicate a mixing transition in the far field of turbulent jets.

The nature of the weighted sums in equation (6.20) shows that large lakes of high shape complexity can increase substantially the total shape complexity. Lakes

of high shape complexity and large size are indeed observed, across a wide range of sizes (*cf.* figure 38), contributing to the (relatively) high total shape complexity.

Conclusions

Turbulent mixing structure — The multiscale structure of mixing in turbulent flows, in general, and in turbulent jets, in particular, can be quantified in terms of scalar-field and scalar-isosurface measures (*e.g.*, Catrakis and Dimotakis 1996a). Different aspects of turbulent mixing can be investigated by these two complementary approaches. In particular, scalar-field statistics provide amplitude-distribution measures of the mixing structure (*e.g.*, the scalar pdf or power spectrum), while isosurface statistics (*e.g.*, the SDF dimension or volume-fill fraction) can be used to compute the distribution of scales generated by the turbulent mixing process. Analysis of both types of statistics shows that, at least in the case of liquid-phase turbulent jets in the Reynolds number range $4.5 \times 10^3 \leq Re \leq 18 \times 10^3$, turbulent mixing occurs over a range of scales whose distribution is dependent on both the flow Reynolds number and the scalar (mixed-fluid concentration) threshold.

Reynolds number effects; mixing transition — Analysis of both scalar-field and isosurface measures in the far-field of liquid-phase turbulent jets indicates a transition between different states of turbulent mixing, in the Reynolds number range $4.5 \times 10^3 \leq Re \leq 18 \times 10^3$ (Catrakis and Dimotakis 1996a). The Reynolds-number dependence of such measures as the scalar (jet-fluid concentration) pdf, (*cf.* figure 8), the area enclosed by the isosurfaces (*cf.* figure 12), and the spatial extent (bounding-box size) of the isosurfaces (*cf.* figure 14), is most manifest at lower scalar values, corresponding to the outer region of the jet. This region generally contains lower scalar-threshold isosurfaces and lower velocities, and can be expected to exhibit increased viscous effects and higher sensitivity to the Reynolds number. Conversely, SDF isosurface measures do not exhibit a discernible Reynolds number effect at low ($c = c_1$) scalar values. Additionally, a conspicuous Reynolds number dependence is found for SDF measures of the isosurface geometry, such as the SDF dimension and the pdf of largest-empty-box (LEB) scales, at the intermediate ($c = c_2$) scalar value. This threshold, near the peak of the pre-transition

scalar pdf's (*cf.* figure 8), corresponds to isosurfaces mostly to be encountered in the intermediate-radius (high-shear) regions of the jet (*cf.* b-series of figures 9–11). For this threshold, the coverage-length of the isoscalar contours *decreases* with increasing Reynolds number (*cf.* figure 29). The SDF dimension is also found to decrease with increasing Reynolds number (*cf.* figure 30), at the moderate-to-large scales, indicating an isosurface geometry that becomes less complex, in this scale range, as the Reynolds number increases. Consistent with these findings is the Reynolds-number dependence of the distribution of LEB scales. In particular, the data indicate that small-scale regions of the flow are more likely to be visited by the isosurfaces; a lower probability of finding a LEB region of that size, as the Reynolds number is increased (*cf.* figure 31). Finally, the expectation value of the LEB scale (as well as the most probable) is *increasing* with increasing Reynolds number (*cf.* figure 31); the distance from a point in the bounding box to the c_2 isosurface is increasing with increasing Reynolds number. These observations, taken collectively, indicate enhanced molecular *mixing*, that is responsible for (local) scalar-field homogenization, relative to *stirring*, that is responsible for isoscalar surface-area generation, with increasing Reynolds number.

Geometry of isosurfaces in turbulence and turbulent mixing — The coverage of isosurfaces of jet-fluid concentration is found to possess a scale-dependent-fractal (SDF) dimension that increases continuously with increasing scale. In particular, for level sets derived from 2-D, scalar-field images, the SDF dimension increases smoothly from near unity, at the smallest scales, to 2, at the largest scales, indicating that the geometric complexity of the isosurfaces increases monotonically with increasing scale. This behavior necessitates a scale-dependent generalization of (constant-dimension) fractal geometry. The framework of SDF geometry can be used to quantify the scale-dependence of various measures of the isosurfaces, *e.g.*, the volume-fill fraction. In addition, the interpretation of this SDF behavior in terms of the distribution of largest-empty-box (LEB) scales (chapter 5), as well as analysis of distributions of scales reported from velocity and concentration measurements in a variety of turbulent flows, suggest that the more-inclusive SDF framework can be used to quantify the multiscale geometry of turbulence and turbulent mixing, in general. The monotonic increase of the SDF dimension with increasing scale is probably a generic property of turbulent flows. One can argue that it would also

be encountered in other turbulent-mixing flows.

Scale distribution, SDF geometry, and models — The theoretical framework developed in chapter 4 shows that SDF coverage statistics of multiscale geometries are invertible and can be used to compute the distribution of scales: spacing scales, in 1-D, or largest-empty-box (LEB) scales in multidimensions (Catrakis & Dimotakis 1996b). For the case of power-law scaling over a finite range of scales, it is shown that power-law behavior is can be assessed (*cf.* figure 19) more accurately in terms of the pdf of scales, rather than fractal dimensions. Also, for the case of exponential or lognormal distributions of scales, both of which have been reported as good approximations of distributions of 1-D scales in level crossings of velocity and concentration measurements in various turbulent flows, the continuous variation of $D_d(\lambda)$ with scale (*cf.* figures 17 and 18) shows that this SDF behavior is intrinsic and, in particular, not a consequence of finite-size effects. A model of the distribution of scales is proposed, in terms of 2-D LEB scales, and shown to provide a good approximation to the distribution of scales in level sets derived from the 2-D image data in turbulent jets, at the small scales. Such scale distributions, at least at the small scales, may be expected for isosurfaces in turbulence and turbulent mixing in other flows.

Size and shape complexity — Isoscalar islands and lakes are found to exhibit a joint distribution of size and shape complexity, at least in the case of jet flows in the Reynolds number range investigated. Consistent with SDF geometric behavior, the size distribution is found to be approximately lognormal. Also, the data indicate a power-law distribution of shape complexity (log-Poisson statistics). The isoscalar islands and lakes exhibit a range of values of the shape complexity, Ω_2, that increase with increasing size; the interfacial length of the isoscalar structures, normalized by the enclosed (root) area, increases with area. For small sizes, Ω_2 tends to unity, indicating that the smallest isoscalar contours are relatively smooth and approach near-circular shapes. This can be appreciated, kinematically, by noting that the shape of a particular-sized flow structure is more sensitive to being distorted, at its own scale, by smaller structures, and to a lesser extent by larger-scale flow structures. Accordingly, larger-sized structures may be expected to be more complex in shape, as they subtend a larger fraction of the distribution

of scales.

Multiscale nature of turbulence — The experiments and analyses described in this thesis suggest that the geometry of scalar isosurfaces in turbulent jets, in particular, and in other turbulent flows, in general, can be quantified in terms of SDF measures and the distribution of scales (see, specifically, chapter 5). As the geometry of the isosurfaces is a result of the (space-time) dynamics of turbulent mixing in one of the canonical flows (jet), with transport and mixing occurring over a wide range of scales, one can expect that other multiscale, turbulence-generated structures, in a variety of other flows, will also exhibit a geometric behavior that is, at least qualitatively, SDF. While different turbulent flows may have quantitatively different SDF statistics as, for example, turbulent shear layers, boundary layers, wakes, *etc.*, the distribution of scales holds the promise of possessing universal features (lognormal statistics) at the small scales. In addition, the connection between SDF behavior and the scale distribution (chapter 4), in conjunction with additional evidence of SDF behavior in a variety of other multiscale natural phenomena, suggest that SDF geometry may be expected to be prevalent — and can be used to compute the distribution of scales — in multiscale natural phenomena, in general, and in turbulence, in particular.

APPENDIX A

Isosurface representation and coverage

Conventional methods for the representation and coverage of isosurfaces (level sets) derived from digital images are based on the identification of boundary pixels. In the analysis of the data described here, the scalar image $c(x, y)$-surfaces were represented using bilinear B-splines. Isoscalar contours (level-sets) were then computed from the bilinear B-spline representation. This removes several difficulties associated with pixel-based schemes.

The effects of pixel representations on the identification of isosurfaces will be discussed first. Figure A.1 depicts a scalar isosurface contour, for $c = c_1$, at $Re \simeq 9.0 \times 10^3$ (*cf.* figure 8) using conventional, boundary pixels, within the field-of-view of the image. The field-of-view is, by design, larger than the local ($z/d = 275$) transverse jet extent. All individual level sets of the measured isosurfaces are thus closed and fully contained within the field-of-view.

A selected portion of the isosurface of figure A.1, indicated by an arrow, is shown enlarged in figure A.2 using conventional boundary pixels. The boundary-outline-pixel representation for this isosurface is also shown in figure A.2, superimposed on the conventional-boundary-pixel representation. Boundary-outline pixels cover the outline of the boundary pixels and were devised and employed in the 2-D streak-image data analysis of Miller & Dimotakis (1991a). Figure A.3 shows a small island and a geometrically-identical lake represented using both conventional and boundary-outline pixels. It is seen that the conventional-boundary-pixel-representation counts for this island and lake are substantially different, even though the two isosurfaces are the same. There is, therefore, an inherent asymmetry in the representation of small lakes and islands using conventional boundary pixels. The boundary-outline-pixel representation removes this asymmetry.

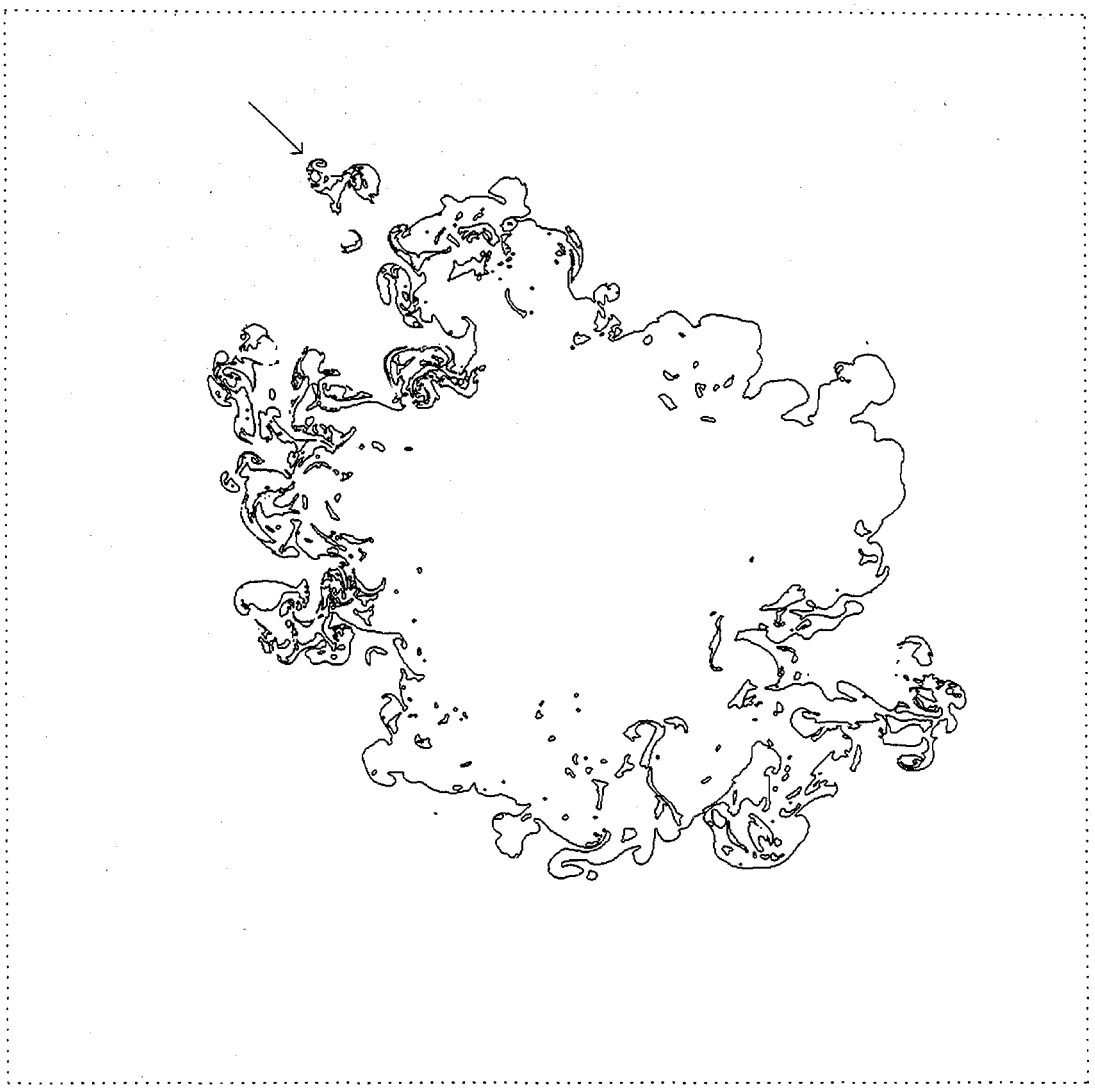

FIGURE A.1 Isoscalar surface at threshold $c = c_1$, for $Re = 9.0 \times 10^3$ (*cf.* figure 8), depicted using conventional boundary pixels. Also shown is the field-of-view (dotted line). Arrow indicates an isoscalar island, magnified and shown in figure A.2.

Figure A.4 compares the ensemble-averaged coverage counts of scalar isosurfaces for $c = c_1$ at $Re \simeq 9.0 \times 10^3$ (*cf.* figure 8) represented using both conventional and boundary-outline pixels. The coverage counts for figure A.4 were computed using a conventional coverage method in which the field-of-view of the image was successively subdivided (*e.g.*, Sreenivasan *et al.* 1989). Figure A.5 shows the corre-

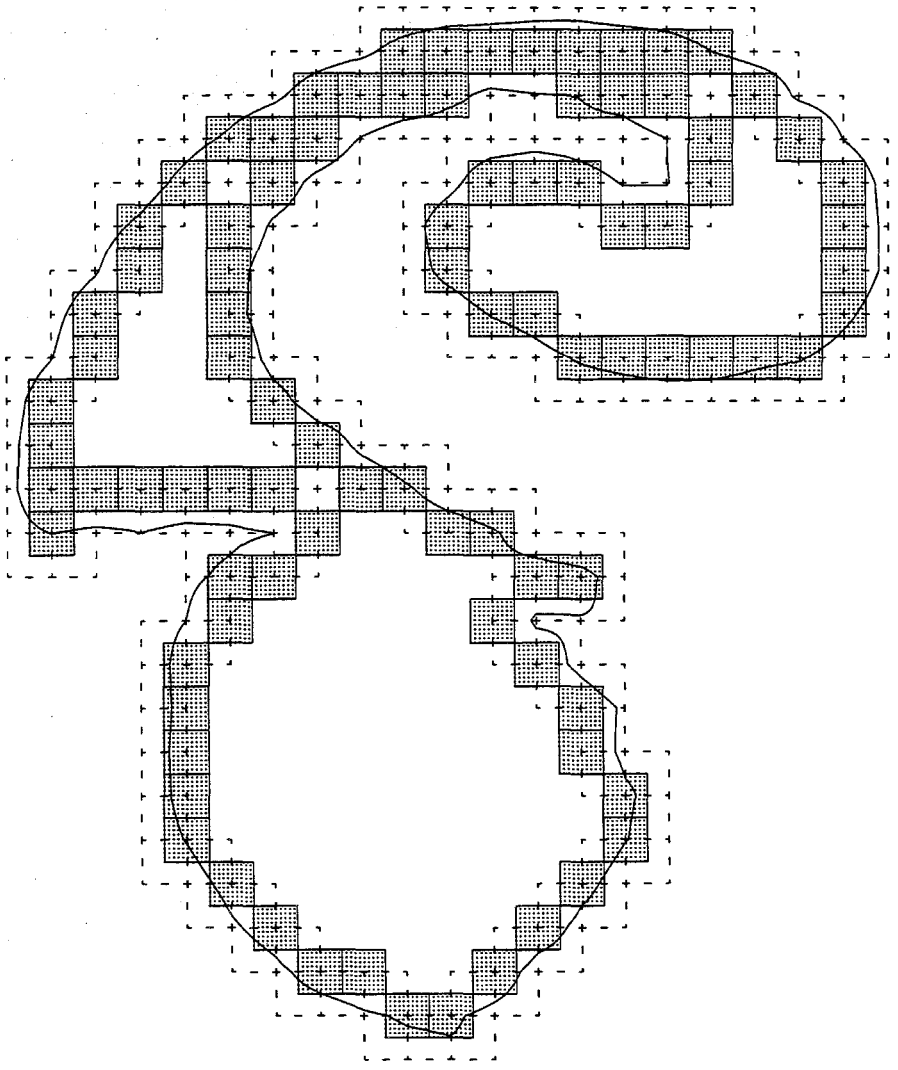

FIGURE A.2 Isoscalar island (indicated by arrow in figure A.1). Bilinear B-spline: solid line; boundary pixels: shaded squares; boundary-outline pixels: dashed squares.

sponding ensemble-averaged SDF dimension, $D_2(\lambda)$, computed from the coverage counts of figure A.4 using 2nd order finite differences. It is seen that the conventional boundary-pixel representation can lead to $D_2(\lambda)$ values at the smallest scales that are less than the topological dimension, d_t, *i.e.*, unity, in this case. This is a result

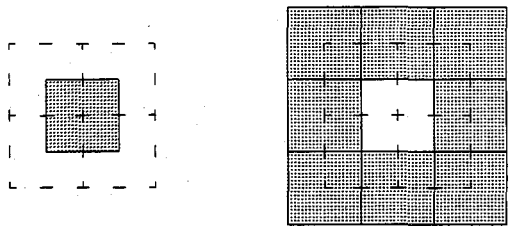

FIGURE A.3 Asymmetry in conventional boundary-pixel representations. The boundary of a small island (left) and of a geometrically-identical lake (right) is covered using conventional *vs.* boundary-outline pixels.

of the asymmetric representation of small lakes/islands with conventional boundary pixels, as noted above. The boundary-outline-pixel representation removes this problem as shown in figure A.5.

The coverage results of figure A.4, however, exhibit an inflection point, at large scales, for both the conventional and boundary-outline pixel representations. This is manifested as a *dip* in the value of $D_2(\lambda)$ at the large scales, as seen in the SDF dimension results in figure A.5. This is an artifact of the fact that the conventional box-counting methods employed to produce the data in figure A.5 subdivide the field-of-view of the image. Those methods do not account for the finite spatial extent of the data, and, as a result, such methods can mask the coverage behavior of the data at the outer scales, producing counts that substantially overestimate the coverage counts at those scales. For example, the ensemble-averaged coverage counts based on successive subdivision of a larger field-of-view (2048×2048 square-pixels) are also shown in figures A.4 and A.5. It is seen that a larger field-of-view, for the same data, can influence the large-scale estimate of the SDF dimension.

To address these issues, we have developed a modified box-counting method, the Bounding-Box Partition Method (BBPM), that removes several shortcomings of conventional box-counting methods. The modified method accounts for the finite spatial extent of each particular isosurface, and is, therefore, able to produce coverage counts over the whole range of scales, from the image-pixel resolution to the spatial extent. The first step of the method is to estimate the spatial extent of each particular isosurface. This is achieved by identifying the bounding box, or smallest circumscribing rectangle (*cf.* Tricot 1995), that covers the isosurface. Figure A.6 shows an example of a bounding box computed for the isosurface of figure A.1, as

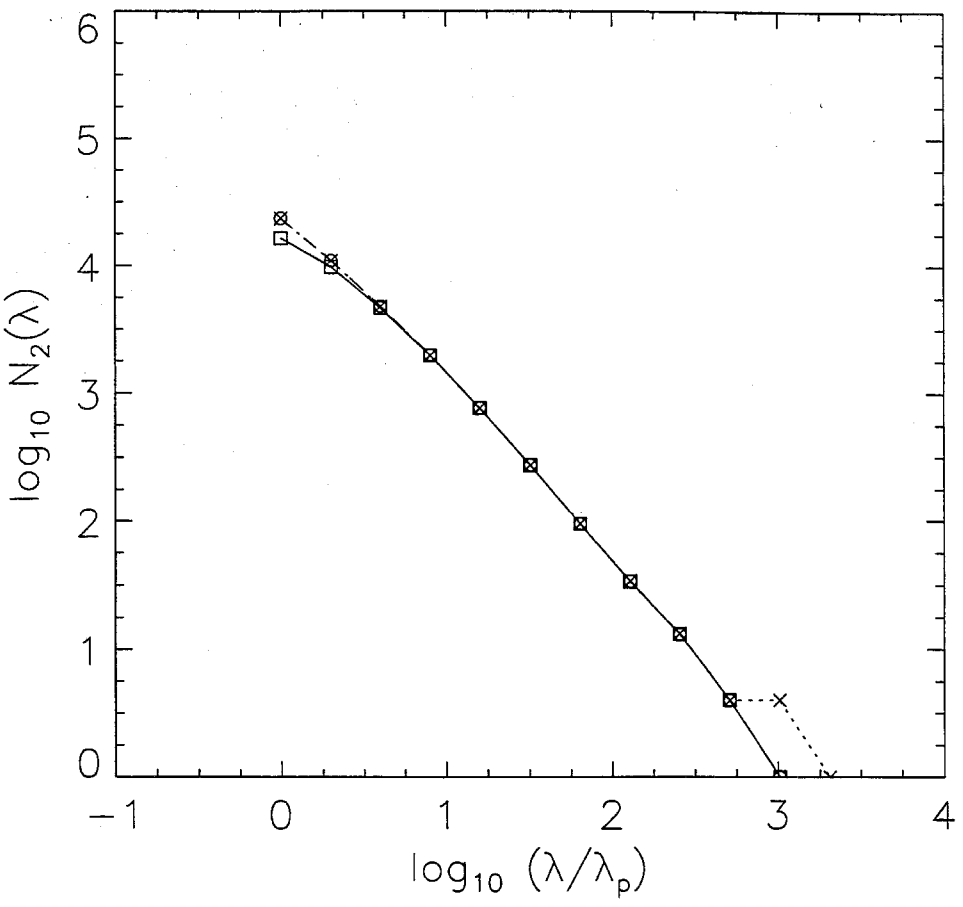

FIGURE A.4 Coverage, $N_2(\lambda)$, of scalar isosurfaces for $c = c_1$ at $Re = 9.0 \times 10^3$ (*cf.* figure 8), computed by successive subdivision of the field-of-view (*cf.* figure A.1). Conventional boundary pixels: solid line, squares; boundary-outline pixels: dashed line, circles; larger field-of-view: dotted line, crosses.

well as the extent of the image field-of-view. A coverage count of unity is assigned for the bounding box. The single scale that corresponds to this coverage count is assigned to the *geometric mean* of the lengths of the two sides, λ_x and λ_y, of the bounding box. This scale is also taken as an estimate of the spatial extent, δ_b, of the isosurface, *i.e.*,

$$\delta_b \equiv (\lambda_x \lambda_y)^{1/2} \quad , \tag{A.1}$$

and, *cf.* equation (3.7),

$$N_2(\delta_b) = 1 \ , \tag{A.2}$$

The largest coverage scale, $\lambda^{(0)}$, at this initial stage of the coverage process, is given, therefore, by $\lambda^{(0)} = \delta_b$. In the first iteration, the bounding box is subdivided into

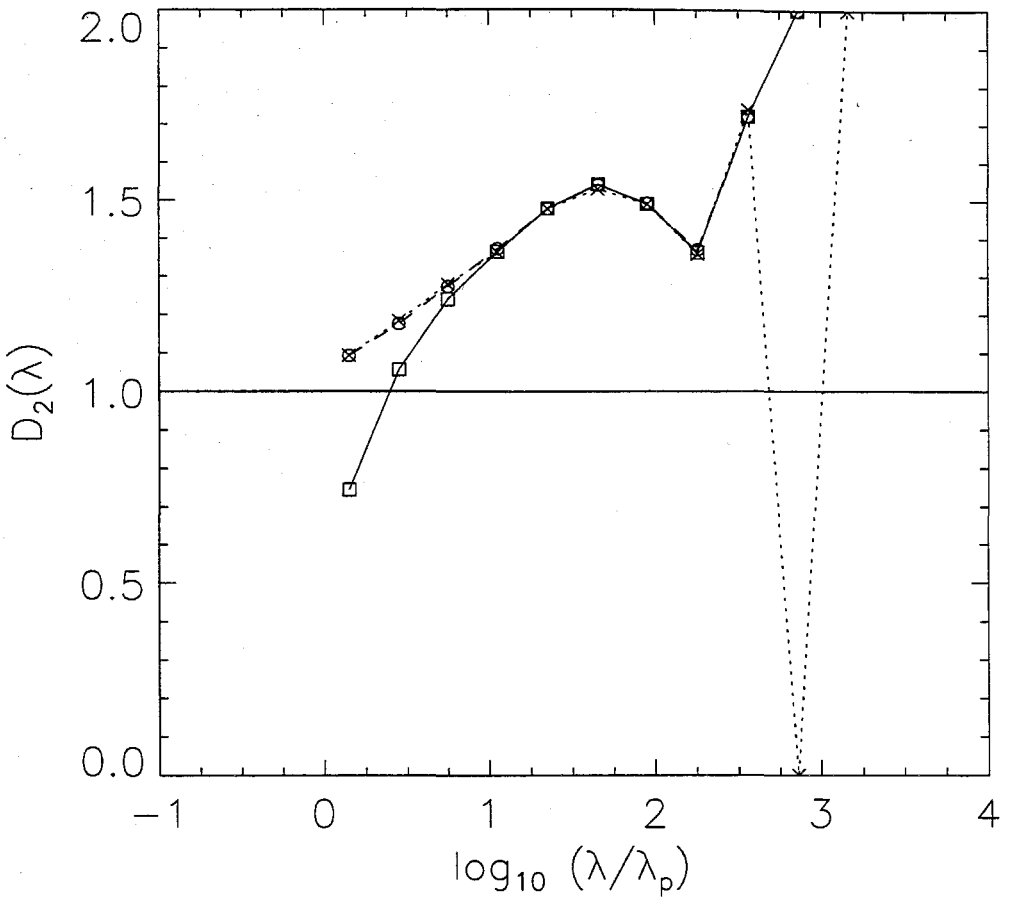

FIGURE A.5 Comparison of SDF dimension, $D_2(\lambda)$, computed for the coverage counts of figure A.4. Same legend as figure A.4. The topological dimension, $d_t = 1$, is also shown (solid line).

four equal rectangles, and the number of the smaller rectangles covering parts of the isosurface is counted. The associated coverage scale, $\lambda^{(1)}$, corresponding to this (first-iteration) count, is computed in a similar fashion, as the geometric mean of the sides of the smaller rectangles, so that $\lambda^{(1)} = \delta_b/2$. The process is repeated by further subdividing each rectangle, so that, at the k^{th} iteration, the coverage scale is given by, $\lambda^{(k)} = \delta_b/2^k$.

The bilinear B-spline representation method developed to represent the isosurfaces removes step-like pixelation difficulties that characterize pixel-based schemes. Bilinear B-splines conserve the (local) integral under the scalar surface, *i.e.*, they match the particular pixel output. Figure A.2 shows the bilinear B-spline representation (solid line) of an isosurface (*cf.* figure A.2). For every set of four neighbouring

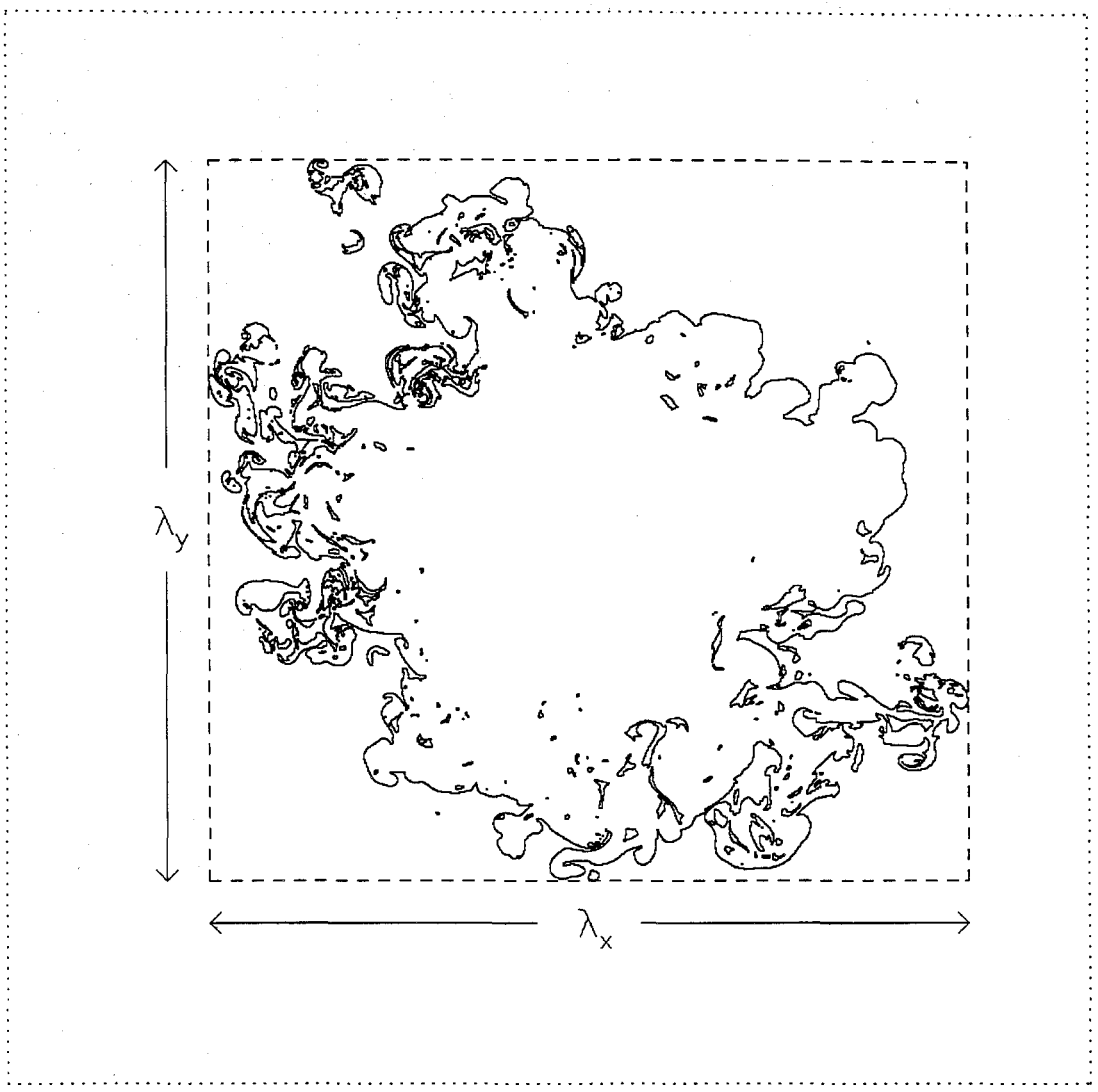

FIGURE A.6 Bounding box (dashed line) computed for the isosurface of figure A.1. Also shown is the field-of-view extent (dotted line). This isosurface is depicted using boundary-outline pixels.

image pixels, segments of the isosurfaces were computed using bilinear B-splines. Level sets of bilinear B-splines can, in general, give two branches within a four-pixel region, each of which belongs to a different isosurface. For this reason, a contour-following algorithm was written which marches along the boundary pixels belonging to the same isosurface. The resulting piece-wise-bilinear isoscalar contours are continuous and closed (*e.g.*, figure A.2).

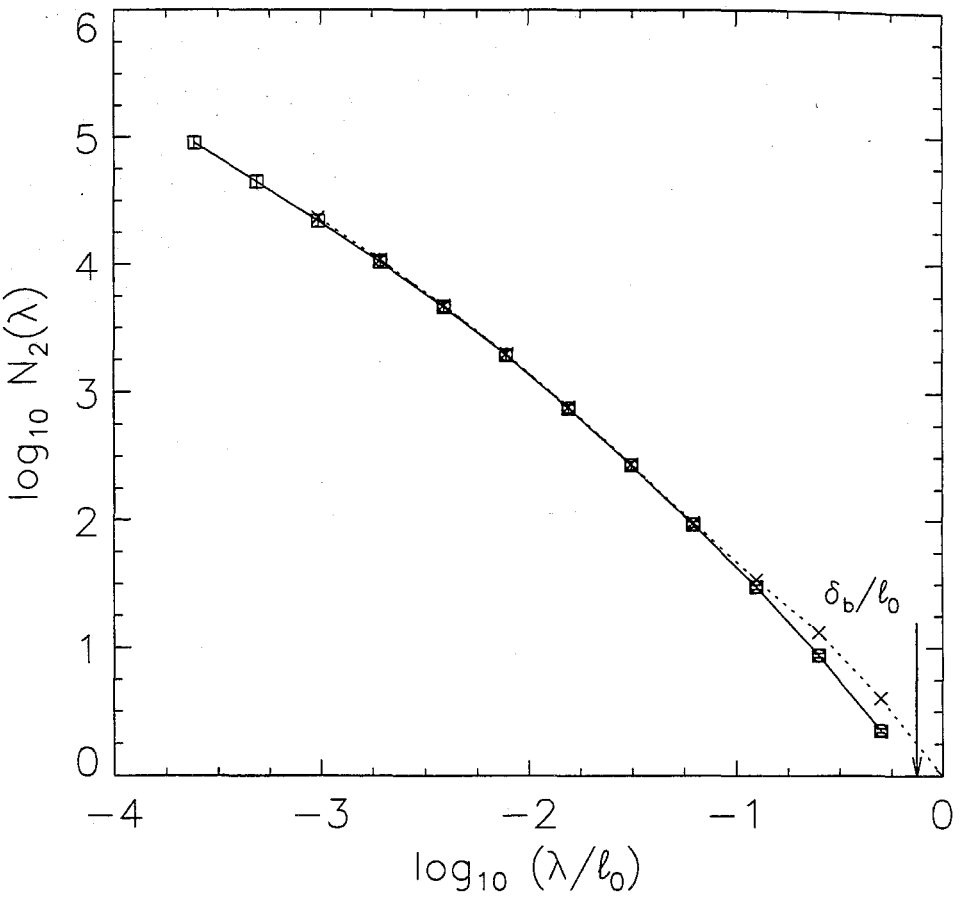

FIGURE A.7 Coverage, $N_2(\lambda)$, of scalar isosurfaces at $c = c_1$ and $Re = 9.0 \times 10^3$ (*cf.* figure 8), computed using the Bounding-Box Partition Method (BBPM). Bilinear B-splines: solid line, squares; boundary-outline pixels: dashed line, circles. Field-of-view-based coverage counts also shown (dotted line, crosses), *cf.* figure A.4. Error bars are for bilinear B-spline BBPM counts (error bars are smaller than data symbols).

The ensemble-averaged coverage computed using the BBPM applied to the bilinear B-spline isosurfaces is shown in figure A.7, for scalar isosurfaces at $c = c_1$ and $Re \simeq 9.0 \times 10^3$. For comparison purposes, figure A.7 also shows the coverage counts computed using the BBPM for isosurfaces represented using boundary-outline pixels, as well as the coverage counts computed using the conventional, field-of-view-based, box-counting method applied to boundary-outline pixels. Figure A.8 shows the ensemble-averaged SDF dimension corresponding to the coverage counts of figure A.7, computed using 2nd order finite differences; note that the ensemble-averaged SDF dimension was computed as the dimension corresponding

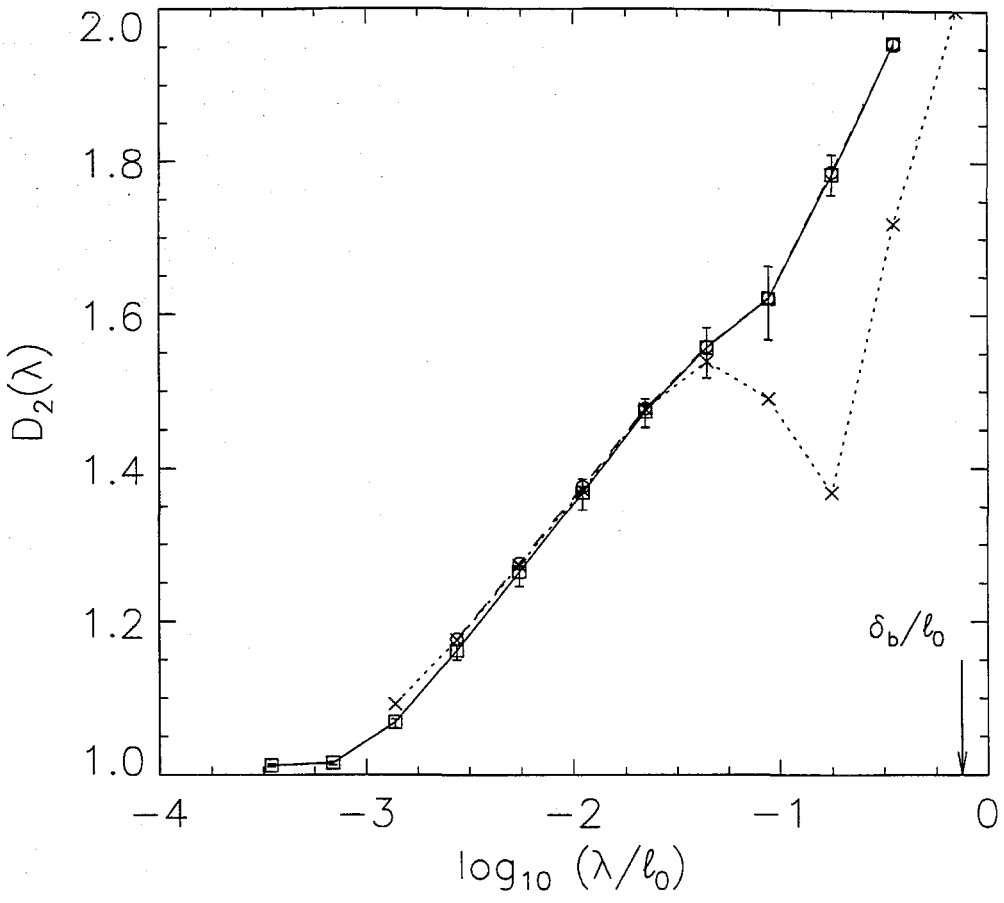

FIGURE A.8 Comparison of SDF dimension, $D_2(\lambda)$, computed for the coverage counts of figure A.7. Legend as in figure A.7. Error bars are for dimension computed from bilinear B-spline BBPM counts (*cf.* error bars for the corresponding counts in figure A.7).

to the ensemble-averaged counts (and, in particular, not as the ensemble-average of the individual dimensions). It is seen that the BBPM removes the (artificial) dip in the value of $D_2(\lambda)$ at large scales.

The uncertainty level in the counts is indicated by error bars in figure A.7. The error bars are of size equal to $\pm$ 1 standard deviation of the mean count (estimated from ensemble-averaging over six realizations) and were computed as,

$$\sigma_{\langle N \rangle} \equiv \sqrt{\frac{1}{n\,(n-1)} \sum_{i=1}^{n} (N_i - \langle N \rangle)^2} \ , \qquad \text{(A.3)}$$

where $n = 6$ is the number of images (at $Re \simeq 9.0 \times 10^3$) and $\langle N \rangle$ is the mean count. The percentage error in the (logarithm of the) coverage count is estimated to

be ±1%, over most of the scale range investigated. The error bars for the dimension were computed based on the dimension values of the individual realizations using an equation similar to (A.3) and are shown in figure A.8; as computed, these error bars correspond to a mean value of the dimension that is different from (slightly less than) the computed ensemble-averaged dimension (as also indicated by the slight asymmetry of the error bars with respect to the ensemble-average), *cf.* discussion on ensemble-averaging procedure above. The corresponding percentage error in the dimension varies with scale: from ±0.5% at small scales, to ±2% at large scales, to ±0.5% at the largest (computed) scale. The uncertainty levels in the dimension (at least in the lower decade of scales) do not affect, therefore, the conclusions reached regarding the SDF geometry and scale distribution of the isosurfaces.

The proposed BBPM yields coverage counts at large scales that follow the spatial extent of the isosurfaces. Additionally, the coverage counts of the proposed method agree at the small scales with the coverage counts obtained using the conventional method at those scales. Figures A.7 and A.8 also show that the bilinear B-spline representation yields coverage counts which agree, at the large scales, with the counts obtained using boundary-outline-pixel representations. At the small scales, boundary-outline-pixel representations lead to overestimates of the coverage necessary for the isosurfaces. Also, the smallest scale at which the conventional methods can produce coverage counts is limited by the pixel scale. The level sets derived from the bilinear B-spline representation, as seen in figure A.8, lead to coverage results that do not have these limitations. The computed SDF dimension approaches unity at the smallest scales, as expected.

APPENDIX B

Effect of noise on coverage

To investigate the effects of noise on the isosurface geometry and, in particular, coverage statistics, scalar isosurfaces were computed from the scalar-field image data of figure 4 ($Re \simeq 9.0 \times 10^3$) for a progression of decreasing threshold values, depicted in figures B.1a-f, from $c/c_{\rm ref} = 0.6$ to 0.1, in steps of 0.1. Note that figure B.1a reproduces the scalar isosurface depicted in figure 9a, for the $c/c_{\rm ref} = c/c_1 = 0.6$ threshold. Recall that this threshold value is outside the range of values corresponding to the near-singular region of the scalar pdf in the vicinity of the zero-value threshold, *cf.* figure 8.

The lowest threshold value is seen to result in qualitatively different isosurfaces (*cf.* figure B.1f). Clusters of points, or "dust", are evident alongside the larger isoscalar structures, at the lower thresholds. This is a direct consequence of noise. At such low values of the scalar threshold, isoscalar surfaces derived from scalar-field image data can be expected to be strongly influenced by noise, as a result of the (relatively) lower signal-to-noise ratio.

As noted earlier (Chapter 1), for the two-dimensional image data analyzed here, the highest-concentration regions are to be found generally in the center of the image, and the lowest-concentration regions in the outer part. Both the highest- and lowest-regions are associated with low signal-to-noise ratio, as compared to the intermediate-concentration, high-shear regions. Additionally, the isosurfaces corresponding to high concentration values have the least spatial extent. It is expected, therefore, that noise has the least effect on isosurface statistics computed for the intermediate concentration values (as compared to lower, or higher, values).

FIGURE B.1 Isoscalar surface at $Re \simeq 9.0 \times 10^3$, derived from the scalar-field image data depicted in figure 4. (a) Threshold level, $c/c_{\mathrm{ref}} = c/c_1 = 0.6$.

FIGURE B.1 (b) $c/c_{\text{ref}} = 0.5$.

FIGURE B.1 (c) $c/c_{\text{ref}} = 0.4$.

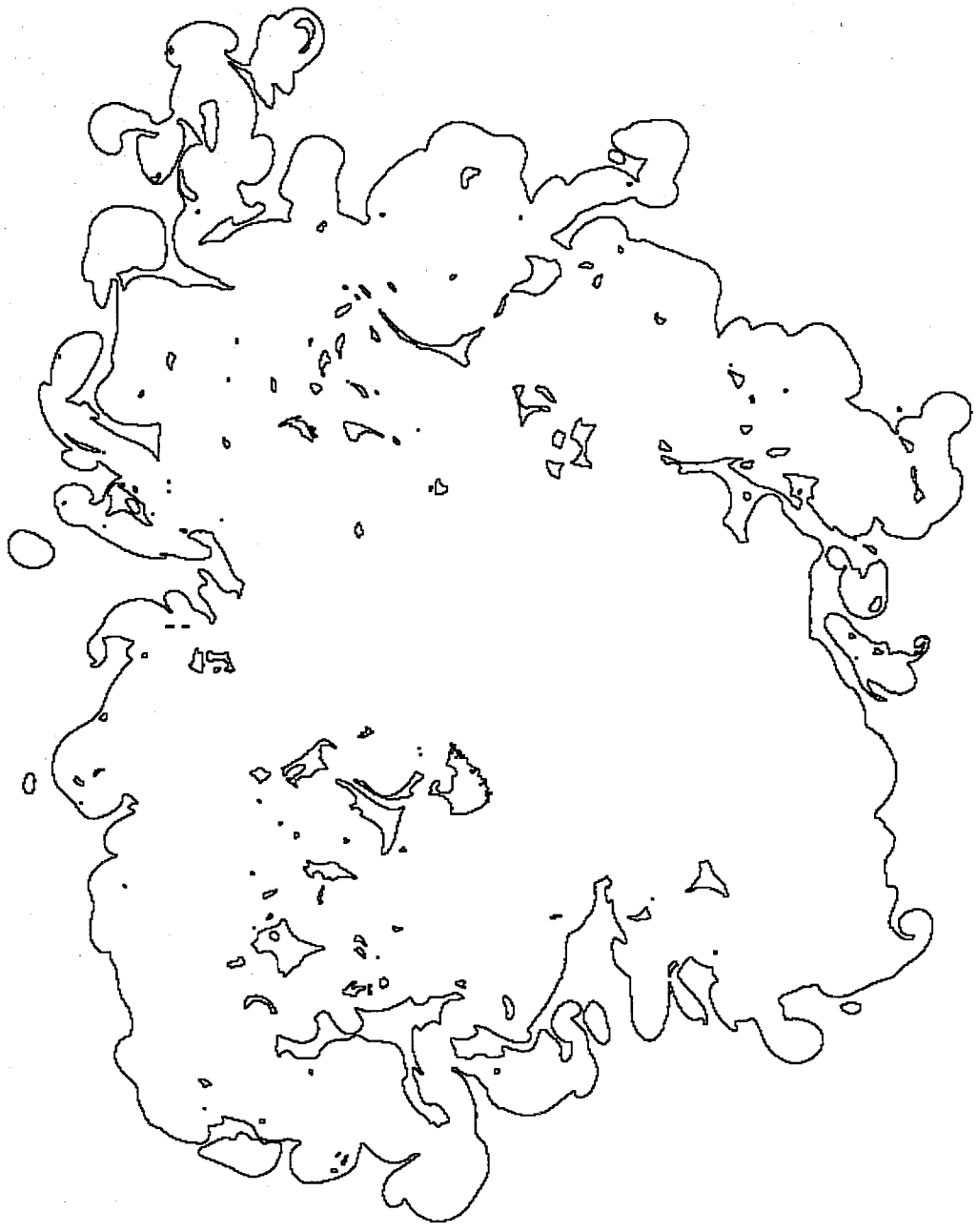

FIGURE B.1 (d) $c/c_{\text{ref}} = 0.3$.

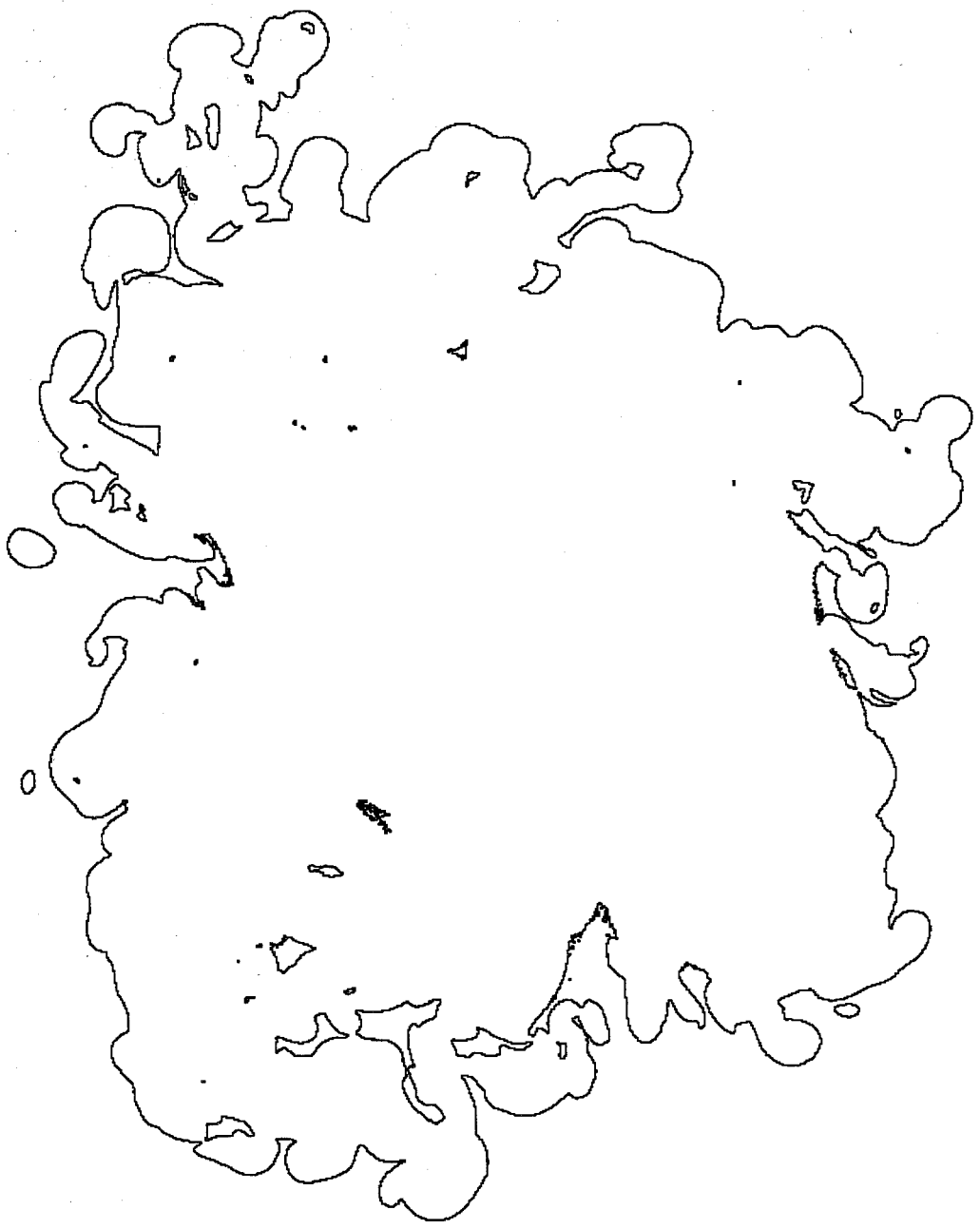

FIGURE B.1 (e) $c/c_{\mathrm{ref}} = 0.2$. Note noise manifested as "dust".

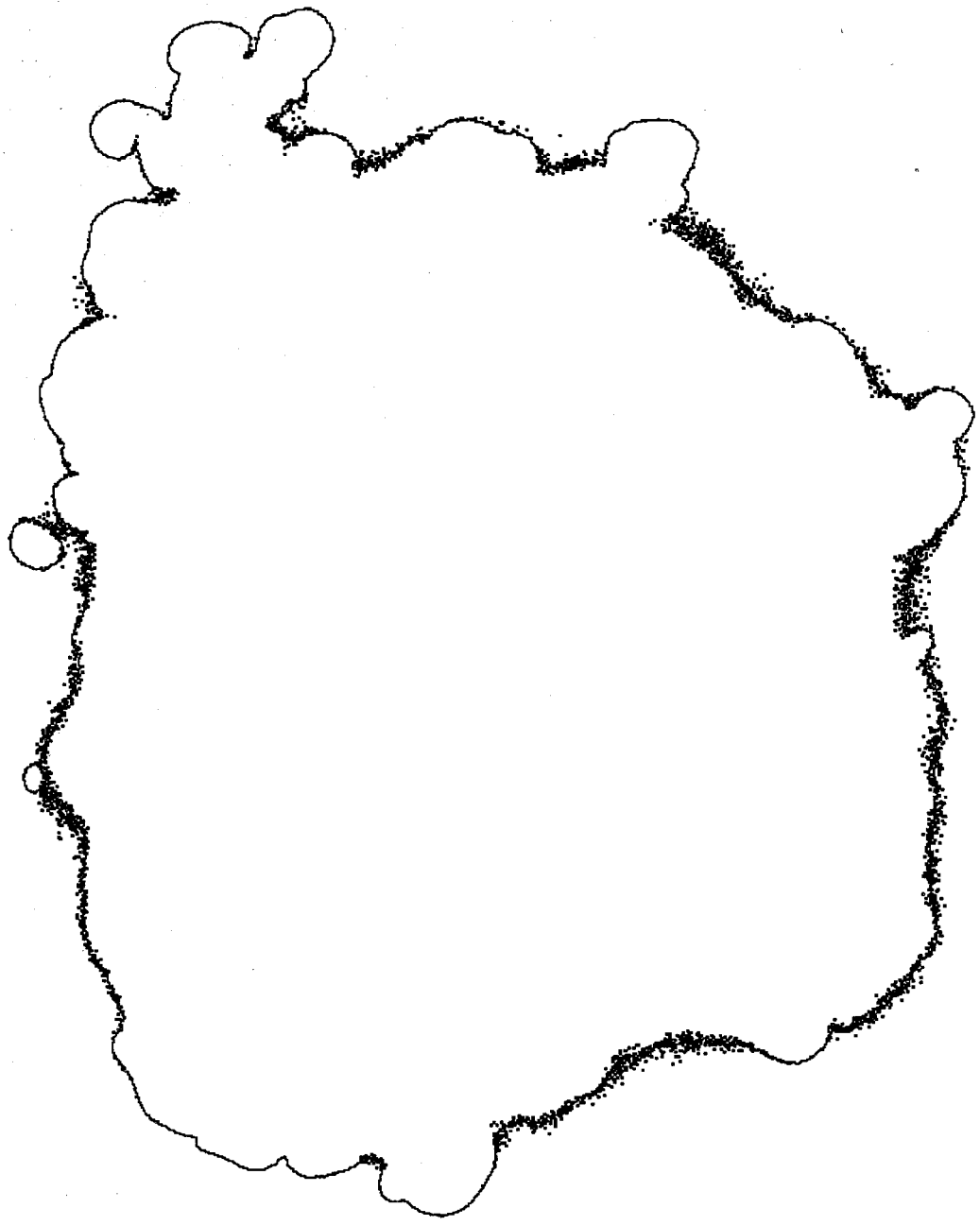

FIGURE B.1 (f) $c/c_{\text{ref}} = 0.1$. Note large regions of "dust" due to noise.

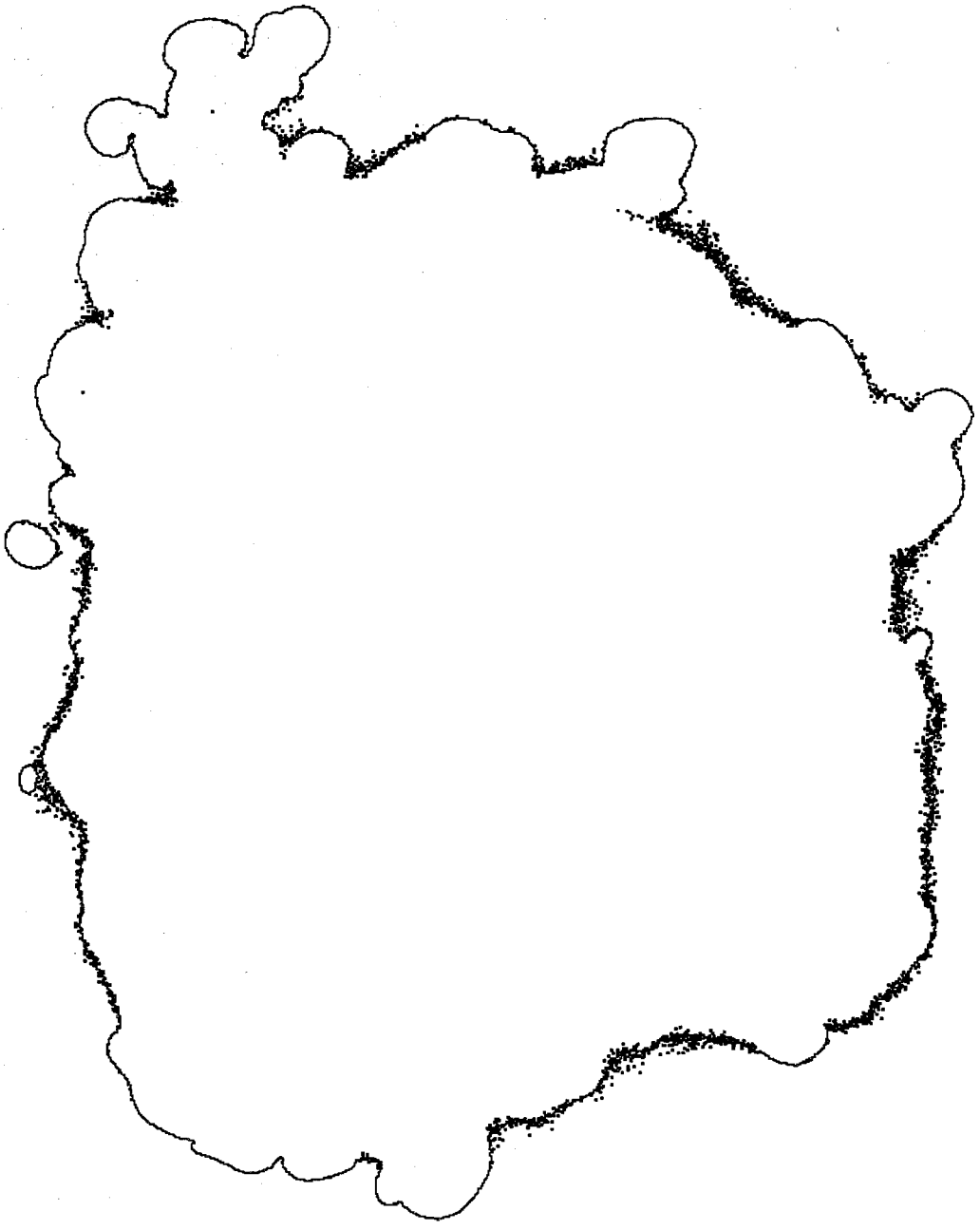

FIGURE B.1 (g) $c/c_{\text{ref}} = 0.104$. This particular threshold was found to give near-PLF behavior (due to the noise), *cf.* figure B.2.

The SDF dimension, $D_2(\lambda)$, computed from the coverage of the isosurfaces depicted in figures B.1a,b is shown in figure B.2. For the higher threshold, $c/c_{\text{ref}} = c/c_1 = 0.6$, the SDF dimension is seen to increase with increasing scale. Note that, while the behavior at $c/c_{\text{ref}} = 0.6$ depicted in figure B.2 result is for a single realization only, it is representative of the qualitative behavior of individual realizations, at this scalar threshold and Reynolds number. Recall, also, that the ensemble-averaged results show a well-defined, smooth SDF behavior at this threshold and Reynolds number, *cf.* figure 25.

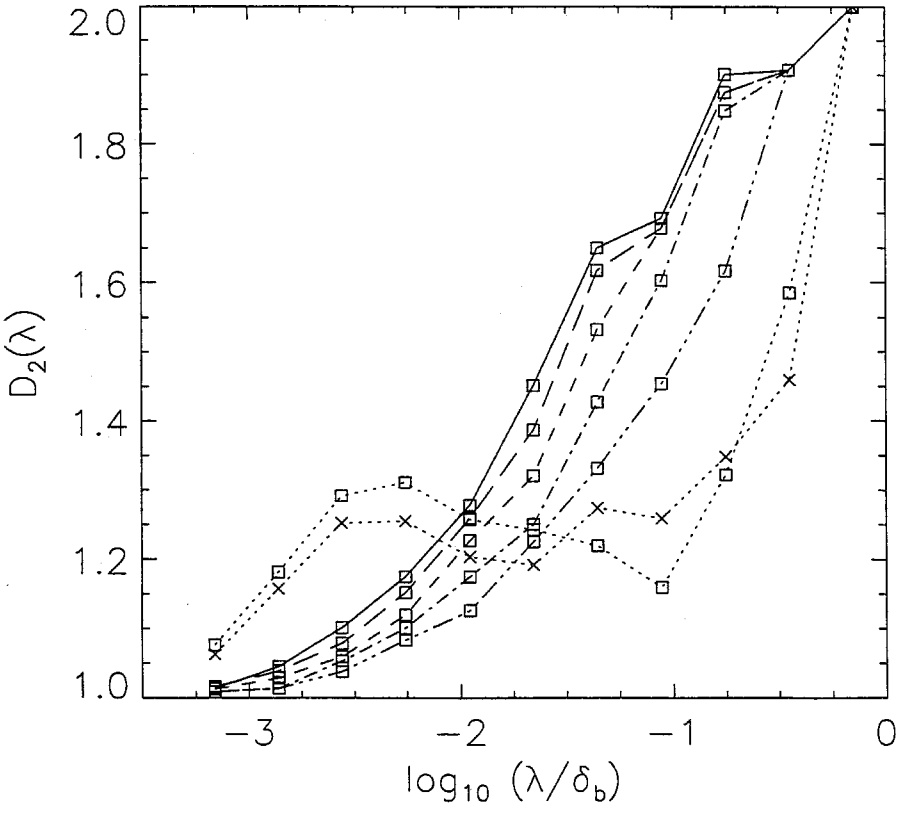

FIGURE B.2 Effect of noise on SDF dimension of the isoscalar surfaces depicted in figures B.1a-f, for a progression of decreasing threshold (c/c_{ref}) values (in square symbols): 0.6 (solid line); 0.5 (long-dash line); 0.4 (short-dash line); 0.3 (dot-dash line); 0.2 (triple-dot-dash line); 0.1 (dotted line, squares). Also shown (dotted line, crosses) are dimension values for $c/c_{\text{ref}} = 0.104$, a particular threshold for which a near-PLF behavior was found.

As the threshold is progressively decreased, a decrease of the SDF value at moderate-to-large scales is evident in figure B.2. At the lowest threshold in the progression ($c/c_{\rm ref} = 0.1$), a (sudden) increase of the SDF value at the smaller scales is evident. In particular, a threshold value can be found for which a region of a near-constant value of the fractal dimension ($D_2 \simeq 1.25 \pm 0.05$, in this case) is indicated at the smaller scales for a threshold of $c/c_{\rm ref} = 0.104$, *cf.* figure B.1g. This is a direct result of noise and, in particular, of the "dust" regions surrounding the isoscalar structures. This dust masks, in effect, the intrinsic geometric scaling of the (noise-free) isosurface, at this threshold.

The non-monotonic behavior of the SDF dimension in figure B.2, at the 2 lowest thresholds ($c/c_{\rm ref} = 0.1$ or 0.104) is due to the *clustering* of points, which can cause the SDF dimension to decrease locally (with increasing scale); *cf.* Appendix D. As noted earlier, the limiting values of the SDF dimension are, respectively, the topological dimension, $d_{\rm t}$, at the smallest scales, and the embedding dimension, d, at the largest scales (*cf.* equation (3.12) and related discussion). These are not necessarily the bounding values, however. The rate at which the SDF dimension decreases with decreasing scale, locally, can be augmented by clustering of structures and can result in the SDF dimension decreasing below $d_{\rm t}$. For example, the SDF dimension may approach zero in the case of point-like clustering of structures. In that case, for clusters that are spaced sufficiently far apart, the SDF dimension can approach zero at scales of the order of the mean spacing between clusters. Similarly, clustering of structures into regions of shapes other than points, *e.g.*, lines or planes, can result in a SDF dimension that locally approaches a value corresponding to the overall cluster topology.

We conclude that low values of the threshold, corresponding to low values of the signal-to-noise ratio, can lead to a qualitatively different geometry and, as a result, different SDF behavior as a result of noise. In particular, a (low) threshold was found ($c/c_{\rm ref} = 0.104$) at which a near-plateau of the fractal dimension ($D_2 \simeq 1.25 \pm 0.05$) was indicated (for a particular realization) which may be interpreted as PLF behavior in a range of scales, *cf.* Sreenivasan 1991. In this case, therefore, noise can lead to PLF behavior. Finally, different manifestations of noise may be expected to give rise to quantitatively different PLF (or SDF) behavior.

APPENDIX C

Area-perimeter computation

For the purpose of computing the perimeter, P, and area, A, of the isoscalar islands and lakes (*cf.* Chapter 6), level set contours were computed using a local biquadratic B-spline representation of the two-dimensional scalar field data. This ensures C^1-continuity of the computed contours (no cusps) and eliminates several pixelation difficulties associated with conventional methods for constructing contours from digital images.

In contrast to pixel representations, B-spline constructions of the isosurface do not impose a maximum, or minimum, value to the possible perimeter corresponding to a given area value, and do not overestimate the arc length of arbitrarily-oriented contours. Additionally, it was found that bilinear (*i.e.*, first-order) B-splines resulted in large overestimates of the perimeter-to-area ratio (or, the dimensionless Ω_2 complexity), for small islands/lakes (*i.e.*, for low values of the area). This effect is due to cusps introduced by the bilinear B-splines; the choice of biquadratic (second-order) B-splines eliminated this difficulty.

A contour-tracking algorithm was also developed that traces each individual island/lake contour, evaluated at subpixel resolution, based on the local biquadratic B-spline representation of the scalar-field, $c(x, y)$-surface. Examples of isoscalar islands computed in this fashion are shown in figures 44 and 45.

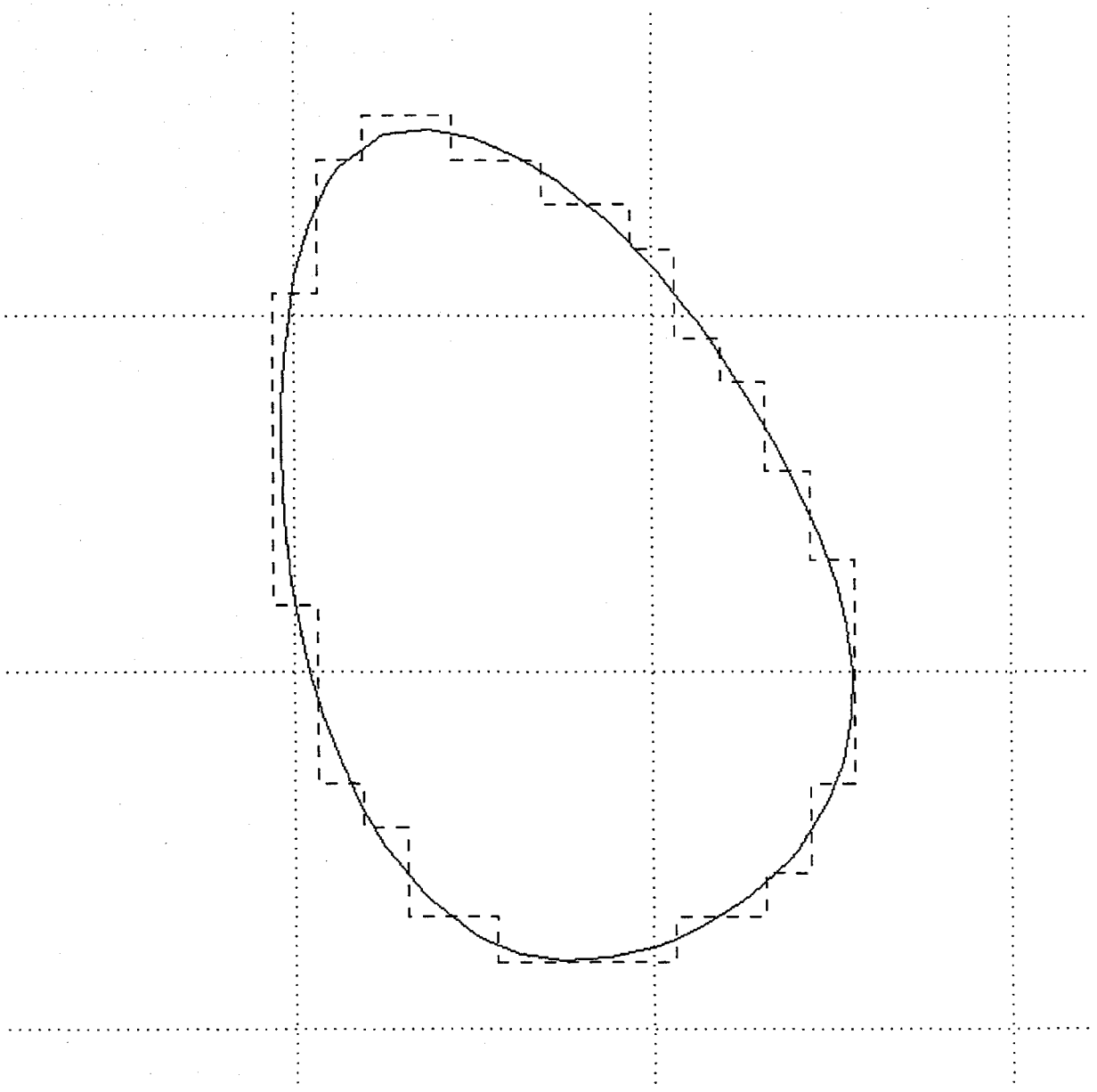

FIGURE 44 Example of an isoscalar island (solid line) derived from a biquadratic B-spline representation of the scalar field. Image pixels are shown as (large) dotted squares. Outer extent of boundary-outline subpixels, evaluated at $1/8^{\text{th}}$ of pixel resolution, is shown as a dashed line.

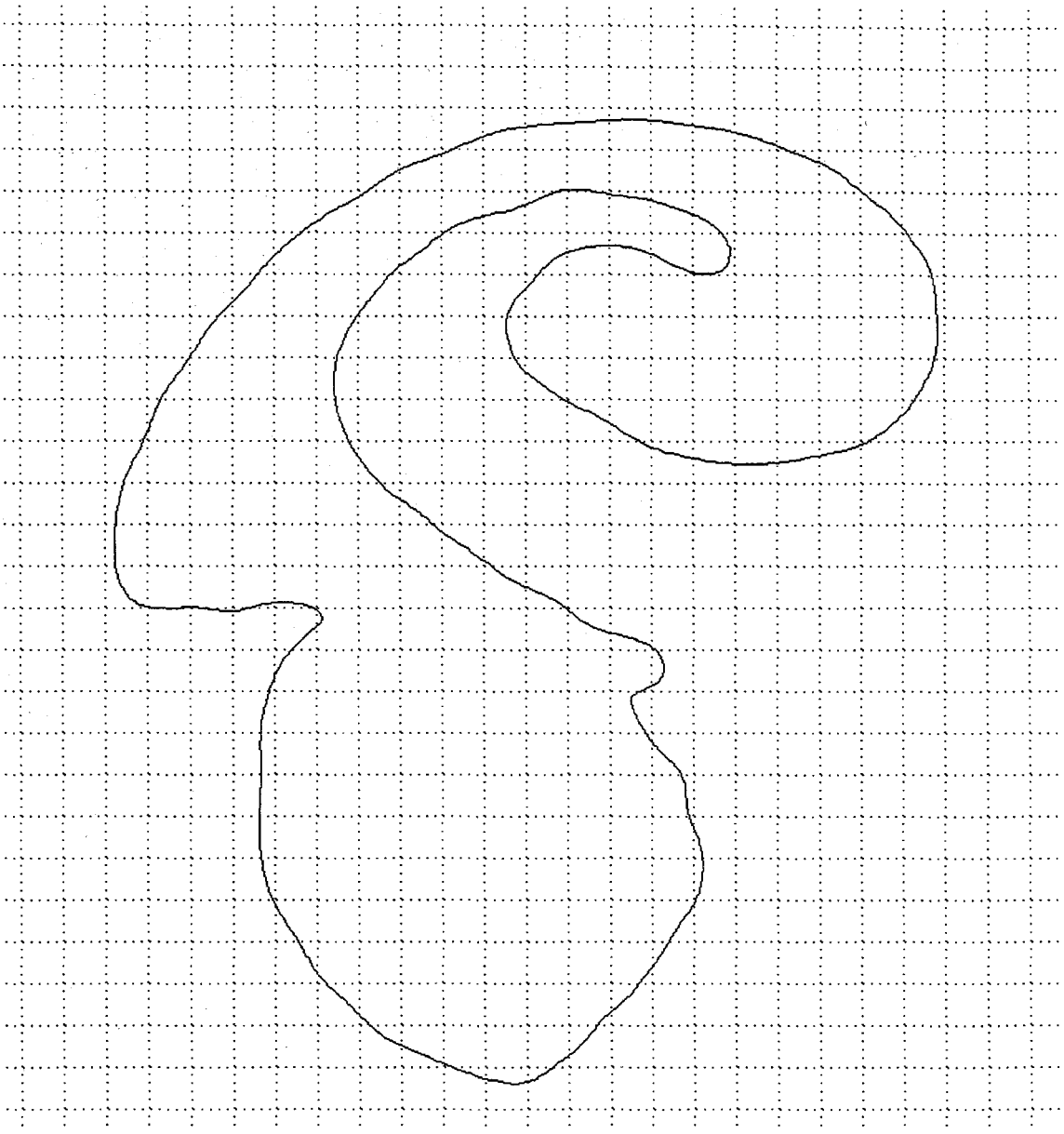

FIGURE 45 Isoscalar island derived from a biquadratic B-spline representation of the scalar-field image data depicted in figure 4, *cf.* figure A.2. Image pixels are shown as dotted squares.

Figure 44 depicts, in addition to the isoscalar island, the outer extent of boundary-outline subpixels that were computed in the contour-tracking process. A subpixel resolution of $1/8^{\text{th}}$ of the image-pixel resolution was chosen to compute these boundary-outline subpixels using local biquadratic B-splines. As long as this subpixel resolution is small compared to the smallest features sought, this scheme will track successfully the individual islands/lakes. From the outer extent of the boundary-outline subpixels, intersections with the contours were computed employing, again, biquadratic B-splines. The intersection points were joined with straight-line segments, as shown in figure 44.

It is seen that the biquadratic B-spline representation eliminates cusps, as opposed to bilinear B-splines (*cf.* figure A.2). While this is not an issue for the computation of coverage statistics, it is an important issue for the computation of area-perimeter statistics, as discussed above.

APPENDIX D

Scale-dependent-fractal (SDF) transform pairs

For reference, recall first the general 1-D SDF transform pair derived in chapter 4 for statistically homogeneous point sets, *cf.* equation (4.9),

$$D_1(\lambda) \;=\; 1 - \frac{\lambda \int_\lambda^\infty p_1(l)\,\mathrm{d}l}{l_\mathrm{m} - \int_\lambda^\infty (l-\lambda)\,p_1(l)\,\mathrm{d}l} \;=\; 1 - \frac{\lambda \int_\lambda^\infty p_1(l)\,\mathrm{d}l}{\int_0^\lambda \int_{\lambda'}^\infty p_1(l)\,\mathrm{d}l\,\mathrm{d}\lambda} \;, \tag{D.1}$$

and, conversely,

$$\begin{aligned} p_1(l) \;=\; & \frac{l_\mathrm{m}}{l^2} \left\{ D_1(l) \left[1 - D_1(l)\right] + l \frac{\mathrm{d}D_1(l)}{\mathrm{d}l} \right\} \\ & \times \exp\left\{ - \int_l^\infty \left[1 - D_1(l')\right] \frac{\mathrm{d}l'}{l'} \right\} \end{aligned} \;, \tag{D.2}$$

where $D_1(\lambda)$ is the 1-D SDF dimension and $p_1(l)$ is the pdf of spacing scales. The mean scale, l_m, is given by,

$$\begin{aligned} l_\mathrm{m} \;\equiv\; & \int_0^\infty l p_1(l) \mathrm{d}l \\ =\; & \lim_{l \to 0} \quad \left\{ l \, \exp\left[\int_l^\infty \left[1 - D_1(l')\right] \frac{\mathrm{d}l'}{l'} \right] \right\} \end{aligned} \;. \tag{D.3}$$

SDF transform pairs for several distributions of (spacing) scales (in 1-D) are listed in table S, below.

	$p_1(l)$	$D_1(\lambda)$
(S.1)	$\delta(l-l_{\rm m})$	$\begin{cases} 0, & \lambda < l_{\rm m} \\ 1, & l_{\rm m} < \lambda \end{cases}$
(S.2)	$\frac{\delta(l-l_1)}{2} + \frac{\delta(l-l_2)}{2}$	$\begin{cases} 0, & \lambda < l_1 \\ \frac{1}{1+\lambda/l_1}, & l_1 < \lambda < l_2 \\ 1, & l_2 < \lambda \end{cases}$
(S.3)	$\frac{a-1}{a^N-1}\sum_{k=0}^{N-1} a^k \delta\left(l - \frac{l_0}{b^k}\right)$	$\begin{cases} 0, & \lambda < \frac{l_0}{b^{N-1}} \\ \frac{\sum_{i=k+1}^{N-1}\left(\frac{a}{b}\right)^i}{\sum_{i=k+1}^{N-1}\left(\frac{a}{b}\right)^i + \frac{\lambda}{l_0}\sum_{i=0}^{k} a^i}, & \begin{cases} \frac{l_0}{b^{k+1}} < \lambda < \frac{l_0}{b^k} \\ k = 0, \ldots, N-1 \end{cases} \\ 1, & l_0 < \lambda \end{cases}$
(S.4)	$\frac{1}{l_{\rm m}} e^{-l/l_{\rm m}}$	$1 - \frac{\lambda/l_{\rm m}}{e^{\lambda/l_{\rm m}} - 1}$
(S.5)	$\frac{e^{-\frac{1}{2}\left[\frac{\ln\left(\frac{l}{l_{\rm m}}\right)}{\sigma} + \frac{\sigma}{2}\right]^2}}{\sqrt{2\pi}\sigma l}$	$1 - \left\{1 + \frac{l_{\rm m}}{\lambda}\left[\frac{1+\operatorname{erf}\left[\left(\ln(\lambda/l_{\rm m})/\sigma - \sigma/2\right)/\sqrt{2}\right]}{1-\operatorname{erf}\left[\left(\ln(\lambda/l_{\rm m})/\sigma + \sigma/2\right)/\sqrt{2}\right]}\right]\right\}^{-1}$
(S.6)	$\begin{cases} \frac{a}{l_1}, & l < l_1 \\ \frac{a l_1^{\nu-1}}{l^\nu}, & l_1 < l < l_2 \\ 0, & l_2 < l \end{cases}$ $1 < \nu < 2$	$\begin{cases} \frac{\lambda/l_1}{2\left(\nu - \alpha^{1-\nu}\right)/(\nu-1) - \lambda/l_1}, & \lambda < l_1 \\ \frac{\beta l_1/\lambda + (1-\nu)(l_2/\lambda)^{\nu-1}}{2 - \nu + \beta l_1/\lambda - (l_2/\lambda)^{\nu-1}}, & l_1 < \lambda < l_2 \\ 1, & l_2 < \lambda \end{cases}$ $\alpha \equiv l_2/l_1, \quad \beta \equiv \nu(\nu-1)\alpha^{\nu-1}/2$

S. Table of SDF transform pairs

	$p_1(l)$	$D_1(\lambda)$
(S.7)	$\begin{cases} a/l_1\,, & l < l_1 \\ a/l\,, & l_1 < l < l_2 \\ 0\,, & l_2 < l \end{cases}$	$\begin{cases} \dfrac{\lambda/2l_1}{1-\lambda/2l_1+\ln(l_2/l_1)}\,, & \lambda < l_1 \\ 1-\dfrac{\ln(l_2/\lambda)}{1-l_1/2\lambda+\ln(l_2/\lambda)}\,, & l_1 < \lambda < l_2 \\ 1\,, & l_2 < \lambda \end{cases}$
(S.8)	$\begin{cases} \frac{a}{l_1}\,, & l < l_1 \\ \frac{al_1}{l^2}\,, & l_1 < l < l_2 \\ 0\,, & l_2 < l \end{cases}$	$\begin{cases} \dfrac{1}{2\,(2-l_1/l_2)\,l_1/\lambda-1}\,, & \lambda < l_1 \\ 1-\dfrac{1-\lambda/l_2}{3/2-\lambda/l_2+\ln(\lambda/l_1)}\,, & l_1 < \lambda < l_2 \\ 1\,, & l_2 < \lambda \end{cases}$
(S.9)	$\begin{cases} 0\,, & l < l_1 \\ a/l^{\nu}\,, & l_1 < l < l_2 \\ 0\,, & l_2 < l \end{cases}$	$\begin{cases} 0\,, & \lambda < l_1 \\ 1-\dfrac{\lambda/l_1}{\dfrac{\lambda}{l_1}-\left(\dfrac{\nu-1}{2-\nu}\right)\left[\dfrac{\left(\frac{\lambda}{l_1}\right)^{2-\nu}-1}{1-\left(\frac{\lambda}{l_2}\right)^{1-\nu}}\right]}\,, & l_1 < \lambda < l_2 \\ 1\,, & l_2 < \lambda \end{cases}$
(S.10)	$\begin{cases} 0\,, & l < l_1 \\ a/l\,, & l_1 < l < l_2 \\ 0\,, & l_2 < l \end{cases}$	$\begin{cases} 0\,, & \lambda < l_1 \\ 1-\dfrac{\lambda\ln(l_2/\lambda)}{\lambda-l_1-\lambda\ln(\lambda/l_2)}\,, & l_1 < \lambda < l_2 \\ 1\,, & l_2 < \lambda \end{cases}$
(S.11)	$\begin{cases} 0\,, & l < l_1 \\ a/l^2\,, & l_1 < l < l_2 \\ 0\,, & l_2 < l \end{cases}$	$\begin{cases} 0\,, & \lambda < l_1 \\ 1-\dfrac{1-\lambda/l_2}{\ln(\lambda/l_1)+1-\lambda/l_2}\,, & l_1 < \lambda < l_2 \\ 1\,, & l_2 < \lambda \end{cases}$

S. Table of SDF transform pairs (continued)

For the cases of exponential (table entry S.4), lognormal (table entry S.5), or power-law (table entry S.6) distributions, plots of the SDF dimension, $D_1(\lambda)$, were given in section 4.3, *cf.* figures 17, 18, and 19, along with Monte-Carlo simulation results. Additional plots of the SDF dimension, for other scale distributions listed in the SDF transform pairs of Table S, are shown in figures 46–49.

For a single-scale pdf, *i.e.*, equally-spaced points (on a line), the SDF dimension exhibits a step-increase at the (characteristic) scale of the pdf, *cf.* table entry S.1). This is shown in figure 46. This behavior implies that the only change in the complexity of the set, as a function of scale, occurs at the (single) characteristic scale of the pdf, as may be argued *a priori*.

A two-scale pdf has a SDF dimension given in table entry S.2. This is plotted in figure 47. It is seen that the SDF dimension changes only in the range of scales bounded by the two characteristic scales. Additionally, the SDF dimension *decreases* with increasing scale, in that range. The behavior of the SDF dimension is, threfore, non-monotonic. This, perhaps surprising, behavior is confirmed by numerical results from 4 Monte-Carlo simulations with $L/l_{\mathrm{m}} = 3000$, plotted in figure 47 along with the theory. The discrepancy, at one of the smaller scales, between theory and simulation (*cf.* figure 47) is due to the discrete nature of the scales at which the box-counting was performed.

Table entry S.3 corresponds to stochastic (statistically-homogeneous) variants of Cantor-like sets (*i.e.*, discrete scale pdfs, as opposed to continuous scale pdfs such as entry S.6). This entry is a generalization of S.2 and has a scale pdf which is non-zero at scales generated by a power-law with a (single) characteristic scale l_0 and parameter b. The probability densities (delta functions) at these scales are also generated from (another) power-law, with parameter a. The parameters a and b (and the scale l_0) can be chosen to study several (stochastic) variations of the Cantor set. The theoretical prediction for the SDF dimension, in general, is also shown in entry S.3.

As an example of entry S.3, parameters were chosen ($a = 2$ and $b = 3$) to correspond to the (stochastic version of the) classic middle-third Cantor set. Four generations of this set result in a SDF dimension shown in figure 48. Multiple

regions of non-monotonicity are evident (*cf.* figure 47). Ten generations (with the same parameter values) are shown in figure 49 (*cf.* table entry S.3). The SDF dimension appears to develop a plateau (with superimposed oscillations), at a value near the (constant) PLF of $D_1 = \log 2/\log 3 \simeq 0.63$ for the (inhomogeneous Cantor) set (in the small-scale limit). This value is indicated in figure 49 as a dashed line.

Table entry S.7 is a special case of (the continuous, power-law scale pdf of) S.6, for a power-law exponent of $\nu = 1$. The resulting SDF dimension increases continuously with scale (at all scales smaller than the upper-cutoff scale l_2) as shown in figure 50. This is, therefore, another example of a case in which power-law behavior (of the scale distribution) is better assessed in terms of the SDF dimension. At the same time, the SDF dimension retains its practical use a quantitative measure of the volume-fill fraction (or complexity) of the set, as a function of scale.

Another special case of S.6, for a power-law exponent of $\nu = 2$, is listed as entry S.8 and is depicted in figure 51, A smoothly-increasing SDF dimension is evident (for scales below the upper-cutoff scale, l_2). This behavior is similar to that of entry S.7 (*cf.* figure 50), with higher values of the SDF dimension at a given scale.

Finally, entries S.9, 10, and 11 are given (for completeness) for scale distributions corresponding to entries S.6, 7, and 8, respectively, with zero probability density below the lower-cutoff scale, l_1. The behavior of the SDF dimension for these cases is similar to the behavior in figures 19, 50, and 51, respectively.

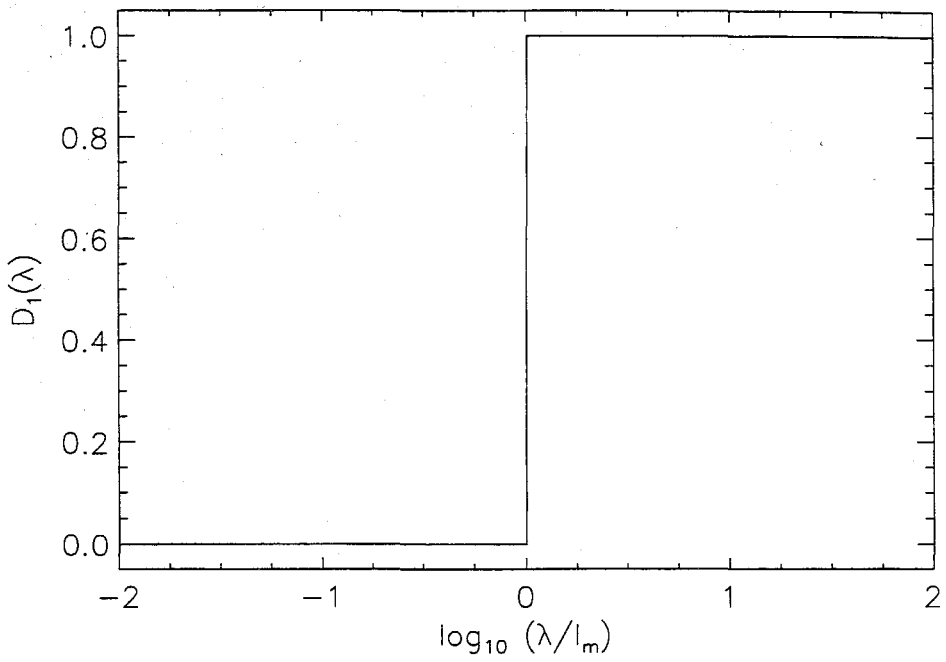

FIGURE 46 SDF dimension, $D_1(\lambda)$, for single-scale pdf, *cf.* table entry S.1.

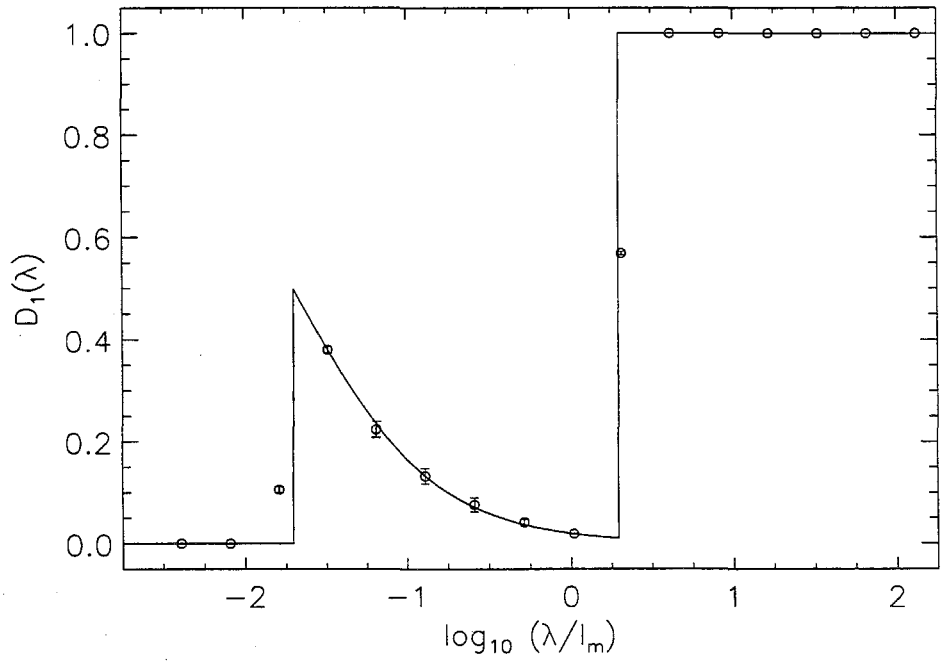

FIGURE 47 SDF dimension for two-scale pdf, *cf.* table entry S.2. Results from 4 Monte-Carlo simulations with $L/l_m = 3000$ are also shown (circles).

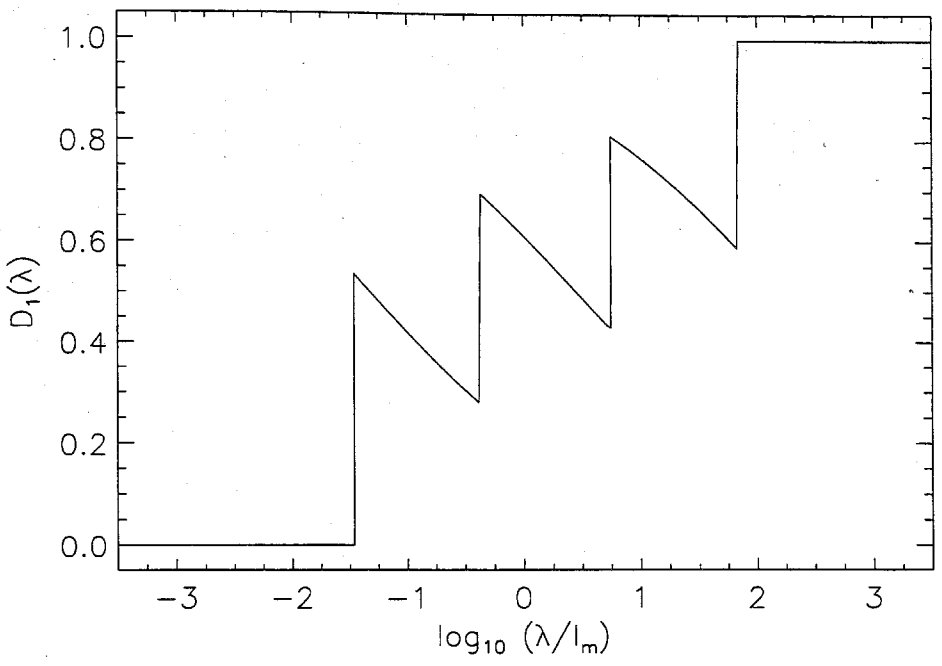

FIGURE 48 SDF dimension, $D_1(\lambda)$, for a discrete power-law pdf, over four generations, with $a = 2$ and $b = 3$, *cf.* table entry S.3.

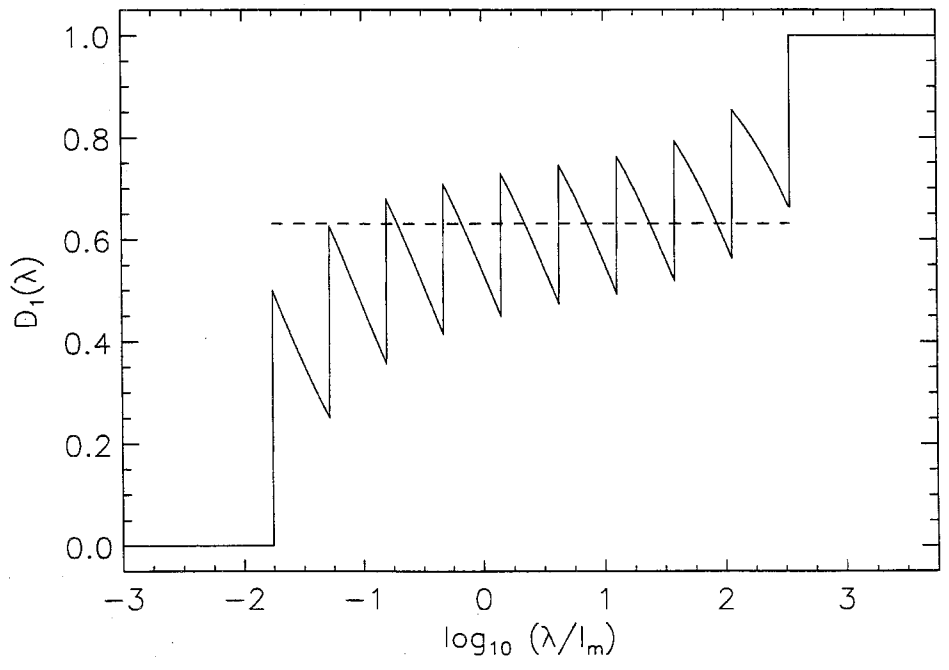

FIGURE 49 SDF dimension, $D_1(\lambda)$, for a discrete power-law pdf, over ten generations, with $a = 2$ and $b = 3$, *cf.* table entry S.3.

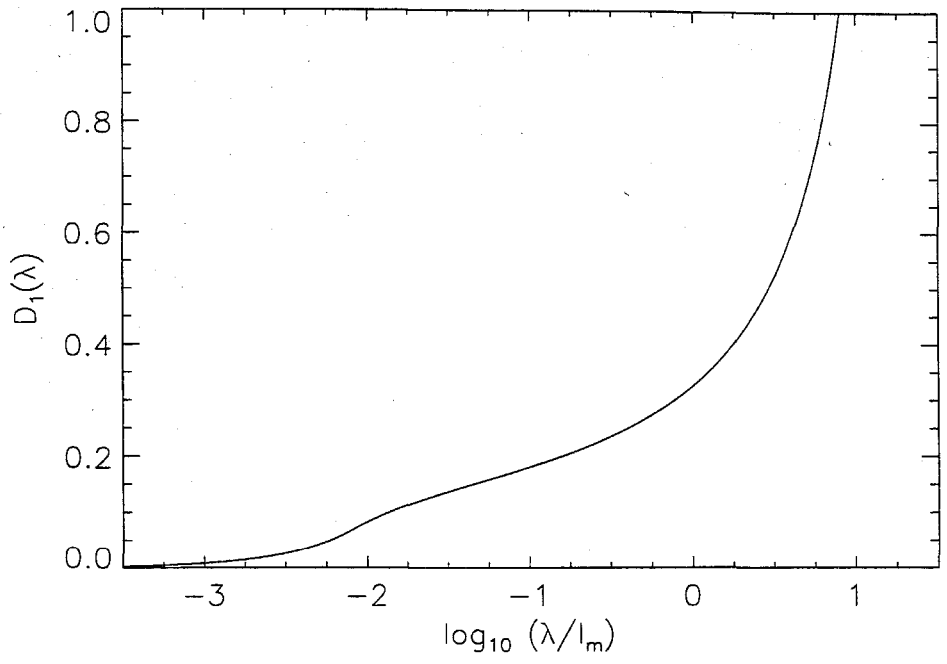

FIGURE 50 SDF dimension, $D_1(\lambda)$, for (continuous) power-law pdf of spacing scales with $\nu = 1$, *cf.* table entry S.7.

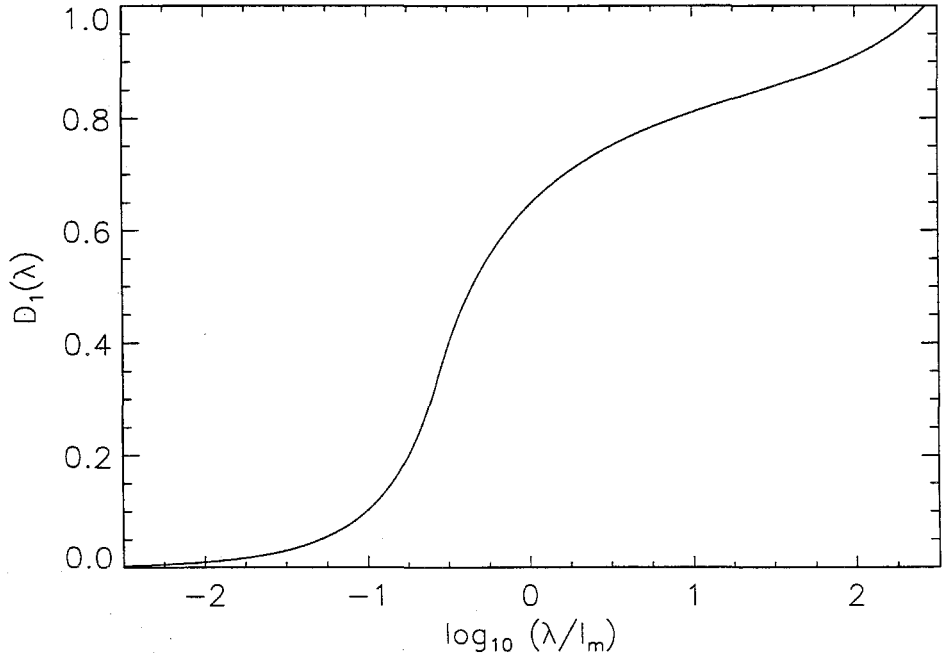

FIGURE 51 SDF dimension, $D_1(\lambda)$, for (continuous) power-law pdf of spacing scales with $\nu = 2$, *cf.* table entry S.8.

References

ASHURST, W. T. 1995 "A Simple Illustration of Turbulent Flame Ball Growth," *Combust. Sci. and Technol.* **104**, 19–32.

BILGER, R. W. 1980 "Turbulent Flows with Nonpremixed Reactants," *Turbulent Reacting Flows* (Eds. P. A. Libby, F. A. Williams, *Topics in Applied Physics* **44**, Springer-Verlag, New York), 65–113.

BORGAS, M. S. 1993 "The multifractal Lagrangian nature of turbulence," *Phil. Trans. Roy. Soc. Lond.* A **342**, 379–411.

BRANDT, P. N., GREIMEL, R., GUENTHER, E. & MATTIG, W. 1991 "Turbulence, Fractals, and the Solar Granulation," in *Applying Fractals in Astronomy* (Eds., A. Heck, J. M. Perdang, Springer, Berlin), 77–96.

CASTAGNOLI, C. & PROVENZALE, A. 1991 "From small-scale fractality to large-scale homogeneity: a family of cascading models for the distribution of galaxies," *Astro. and Astrophysics* **246**, 634–643.

CATRAKIS, H. J. & DIMOTAKIS, P. E. 1996a "Mixing in turbulent jets: scalar measures and isosurface geometry," *J. Fluid Mech.* **317**, 369–406.

CATRAKIS, H. J. & DIMOTAKIS, P. E. 1996b "Fractal Dimensions and Distributions of Scales in Turbulence," (in preparation).

CATRAKIS, H. J. & DIMOTAKIS, P. E. 1996c "Area-Perimeter Measures in Turbulent Jet Mixing: Size and Shape Complexity," (in preparation).

CHILÉS, J. P. 1988 "Fractal and Geostatistical Methods for Modeling of a Fracture Network," *Math. Geol.* **20**(6), 631–654.

CONSTANTIN, P. 1989 "Remarks on the Navier-Stokes equations," in *New Perspectives in Turbulence* (L. Sirovich, Ed., Springer-Verlag, NY, 1991), 229–261.

CONSTANTIN, P. 1990 "Navier-Stokes Equations and Area of Interfaces," *Comm. Math. Phys.* **129**, 241–266.

CONSTANTIN, P. 1994 "Geometric Statistics in Turbulence," *SIAM Rev.* **36**(1), 73–98.

CONSTANTIN, P. 1994 "Geometric and Analytic Studies in Turbulence," in *Trends and Perspectives in Applied Mathematics* (L. Sirovich, Ed., Springer-Verlag, NY), 21–54.

CONSTANTIN, P. & PROCACCIA, I. 1994 "The geometry of turbulent advection: sharp estimates for the dimensions of level sets," *Nonlinearity* **7**, 1045–1054.

CONSTANTIN, P., PROCACCIA, I. & SREENIVASAN, K. R. 1991 "Fractal Geometry of Isoscalar Surfaces in Turbulence: Theory and Experiment," *Phys. Rev. Lett.* **67**(13), 1739–1742.

DAHM, W. J. A. 1985 *Experiments on Entrainment, Mixing and Chemical Reactions in Turbulent Jets at Large Schmidt Numbers*, Ph.D. thesis, California Institute of Technology.

DENNY, M. W. 1988 *Biology and the Mechanics of the Wave-Swept Environment* (Princeton Univ. Press).

DIMOTAKIS, P. E. 1991 "Fractals, dimensional analysis and similarity, and turbulence," *Nonlinear Sci. Today* #2/91, pp. 1, 27–31.

DIMOTAKIS, P. E. 1993 "Some issues on turbulent mixing and turbulence," GALCIT Report FM93–1a.

DIMOTAKIS, P. E., MIAKE-LYE, R. C. & PAPANTONIOU, D. A. 1983 "Structure and Dynamics of Round Turbulent Jets," *Phys. Fluids* **26**, 3185–3192.

FALCONER, K. J. 1990 *Fractal Geometry: Mathematical Foundations and Applications* (Wiley, Chichester).

FLOHR, P. & OLIVARI, D. 1994 "Fractal and multifractal characteristics of a scalar dispersed in a turbulent jet," *Physica D* **76**, 278–290.

GLUCKMAN, B. J., WILLAIME, H. & GOLLUB, J. P. 1993 "Geometry of isothermal and isoconcentration surfaces in thermal turbulence," *Phys. Fluids* **5**(3), 647–661.

HAUSDORFF, F. 1919 "Dimension und äusseres Mass," *Math. Ann.* **79**, 157–179.

KAILASNATH, P. & SREENIVASAN, K. R. 1993 "Zero crossings of velocity fluctuations in turbulent boundary layers," *Phys. Fluids* A **5**(11), 2879–2885.

KERSTEIN, A. R. 1991 "Linear-eddy modeling of turbulent transport. Part V: Geometry of scalar interfaces," *Phys. Fluids* A **3**(5), Pt. 2, 1110–1114.

KOLMOGOROV, A. N. 1941 "The logarithmically normal law of distribution of dimensions of particles when broken into small parts," *Akad. Nauk SSSR* **31**(2), 99–101. Translated: V. Levin [1969] NASA TT F–12287.

KOLMOGOROV, A. N. & TIHOMIROV, V. M. 1959 "ϵ-entropy and ϵ-capacity of sets in functional spaces," *Am. Math. Soc. Translations* (1961, Section II), 277–364.

KOOCHESFAHANI, M. M. & DIMOTAKIS, P. E. 1986 "Mixing and chemical reactions in a turbulent liquid mixing layer," *J. Fluid Mech.* **170**, 83–112.

KORČAK, J. 1938 "Deux types fondamentaux de distribution statistique," *Bull. Inst. Inter. Stat.* **III**, 295–299.

KUZNETSOV, V. R. & SABEL'NIKOV, V. A. 1990 *Turbulence and Combustion* (Hemisphere, New York).

LANE–SERFF, G. F. 1993 "Investigation of the fractal structure of jets and plumes," *J. Fluid Mech.* **249**, 521–534.

LIEPMANN, H. W. 1949 "Die Anwendung eines Satzes über die Nullstellen Stochasticher Funktionen auf Turbulenzmessungen," *Helv. Phys. Acta* **22**, 119.

LONGUET-HIGGINS, M. S. 1958 "On the intervals between successive zeros of a random function," *Proc. Roy. Soc. London* **A246**, 99–118.

LOPEZ, R. E. 1977 "The lognormal distribution and cumulus cloud populations," *Mon. Wea. Rev.* **105**, 865–872.

LOVEJOY, S. 1982 "Area-Perimeter Relation for Rain and Cloud Areas," *Science*, **216**(4542), 185–187.

MANDELBROT, B. B. 1967 "How long is the coast of Britain? Statistical self-similarity and fractional dimension," *Science* **155**, 636–638.

MANDELBROT, B. B. 1975a "On the geometry of homogeneous turbulence, with stress on the fractal dimension of the iso-surfaces of scalars," *J. Fluid Mech.* **72**(2), 401–416.

MANDELBROT, B. B. 1975b *Les objets fractals: forme, hasard et dimension* (Flammarion, Paris).

MANDELBROT, B. B. 1977 *Fractals. Form, Chance, and Dimension* (W. H. Freeman & Co., San Fransisco).

MANDELBROT, B. B. 1982 *The Fractal Geometry of Nature* (W. H. Freeman & Co., New York).

MANDELBROT, B. B. 1989 "Fractal geometry: What is it and what does it do?," in *Fractals in the Natural Sciences* (M. Fleischmann, D. J. Tildesley, R. C. Ball, Eds., Princeton), 7.

MANTZARAS, J. 1992 "Geometrical Properties of Turbulent Premixed Flames: Comparison Between Computed and Measured Quantities," *Combust. Sci. and Technol.* **86**, 135–162.

MARK, D. M. & ARONSON, P. B. 1984 "Scale-Dependent Fractal Dimensions of Topographic Surfaces: An Empirical Investigation, with Applications in Geomorphology and Computer Mapping," *Math. Geol.* **16**(7), 671–683.

MCCOMB, W. D. 1991 *The physics of fluid turbulence* (Clarendon Press, Oxford).

MIKHAILOV, A. S. & LOSKUTOV, A. Y. 1991 *Foundations of Synergetics* **II**: *Complex Patterns* (Springer-Verlag, Berlin).

MILLER, P. L. 1991 *Mixing in High Schmidt Number Turbulent Jets*, Ph.D. thesis, California Institute of Technology.

MILLER, P. L. & DIMOTAKIS, P. E. 1991a "Stochastic geometric properties of scalar interfaces in turbulent jets," *Phys. Fluids A* **3**, 168–177.

MILLER, P. L. & DIMOTAKIS, P. E. 1991b "Reynolds number dependence of scalar fluctuations in a high Schmidt number turbulent jet," *Phys. Fluids A* **3**, 1156–1163.

NONNENMACHER, T. F., LOSA, G. A. & WEIBEL, E. R. 1994 *Fractals in Biology and Medicine* (Birkhäuser-Verlag, Basel, Switzerland).

PRASAD, R. R. & SREENIVASAN, K. R. 1990 "Quantitative three-dimensional imaging and the structure of passive scalar fields in fully turbulent flows," *J. Fluid Mech.* **216**, 1–34.

PROCACCIA, I., BRANDENBURG, A., JENSEN, M. H. & VINCENT, A. 1992 "The fractal dimension of isovorticity structures in 3-dimensional turbulence," *Europhys. Lett.* **19** (3), 183–187.

RICHARDSON, L. F. 1961 "The problem of contiguity: an appendix of statistics of deadly quarrels," *General Systems Yearbook* **6**, 139–187.

RIGAUT, J.-P. 1991 "Fractals, semi-fractals, and biometry," in *Fractals: Non-integral Dimensions and Applications* (G. Cherbit, Ed., Wiley, Chichester, UK), 151–187.

SREENIVASAN, K. R. 1991 "Fractals and Multifractals in Fluid Turbulence," *Ann. Rev. Fluid Mech.* **23**, 539–600.

SREENIVASAN, K. R. 1994 "Fractals in Fluid Mechanics," *Fractals* **2** (2), 253–263.

SREENIVASAN, K. R. & MENEVEAU, C. 1986 "The Fractal Facets of Turbulence," *J. Fluid Mech.* **173**, 357–386.

SREENIVASAN, K. R., PRABHU, A. & NARASIMHA, R. 1983 "Zero-crossings in turbulent signals," *J. Fluid Mech.* **137**, 251–272.

SREENIVASAN, K. R., PRASAD, R. R., MENEVEAU, C. & RAMSHANKAR, R. 1989 "The Fractal Geometry of Interfaces and the Multifractal Distribution of Dissipation in Fully Turbulent Flows," *Pure & Appl. Geoph.* **131**(1–2), 43–60.

SUZUKI, M. 1984 "Finite-Size Scaling for Transient Similarity and Fractals," *Prog. Theor. Phys.* **71**(6), 1397–1400.

TAKAYASU, H. 1982 "Differential Fractal Dimension of Random Walk and Its Applications to Physical Systems," *J. Phys. Soc. Japan* **51**(9), 3057–3064.

TAKAYASU, H. 1992 *Fractals in the Physical Sciences* (Wiley, Chichester, UK).

TAYLOR, G. I. 1921 "Diffusion by Continuous Movements," *Proc. London Math. Soc.* **20**, 196–212.

TRICOT, C. 1995 *Curves and Fractal Dimension* (Springer-Verlag, New York).

TRITTON, D. J. 1988 *Physical Fluid Dynamics* (Oxford Univ. Press).

VASSILICOS, J. C. 1990 "Fractal and moving interfaces in turbulent flows," University of Cambridge, Ph.D. thesis.

VASSILICOS, J. C. & HUNT, J. C. R. 1991 "Fractal dimensions and spectra of interfaces with application to turbulence," *Proc. R. Soc. Lond.* A **435**, 505–534.

VICSEK, T. 1992 *Fractal Growth Phenomena* (2nd Ed., World Scientific, Singapore).

VINCENT, A. & MENEGUZZI, M. 1991 "The spatial structure and statistical properties of homogeneous turbulence," *J. Fluid Mech.* **225**, 1–20.

WARE, B. R., CYR, D., GORTI, S. & LANNI, F. 1983 "Electrophoretic and Frictional Properties of Particles in Complex Media Measured by Laser Light Scattering and Fluorescence Photobleaching Recovery," *Measurement of Suspended Particles by Quasi-Elastic Light Scattering* (Wiley, NY), 255–289.

WELANDER, P. 1955 "Studies on the General Development of Motion in a Two-Dimensional, Ideal Fluid," *Tellus* **7**(2), 141–156.

WELLING, D., URANI, J., WELLING, L. & WAGNER, E. 1996 "Fractal analysis and imaging of the proximal nephron cell," *Cell Physiol.* **39**, 953–963.

YEE, E., CHAN, R., KOSTENIUK, P. R., CHANDLER, G. M., BILTOFT, C. A. & BOWERS, J. F. 1995 "Measurements of level-crossing statistics of concentration fluctuations in plumes dispersing in the atmospheric surface layer," *Bound. Layer Met.* **73**, 53–90.